/
Article / Book Information

( )	
Title(English)	Visualization of metabolic dynamics by mass spectrometry
( )	
Author(English)	Sugiura Yuki
( )	: ( ), : : 7992 , :2010 3 26 , : :
Citation(English)	Degree:Doctor (Engineering), Conferring organization: Tokyo Institute of Technology, Report number: 7992 , Conferred date:2010/3/26, Degree Type:Course doctor, Examiner:
( )	
Type(English)	Doctoral Thesis

Visualization of metabolic dynamics by mass spectrometry

Department of Bioscience and Biotechnology, Tokyo Institute of Technology

Yuki Sugiura

Acknowledgement

Abstract

In life science, localizations of transcripts are visualized with oligo probe *in situ* hybridization, and localizations of proteins are visualized with immunohistochemistry by antibodies. For metabolties, recently imaging mass spectrometry (IMS) technology has begun to practically be utilized.

Metabolites, in terms of metabolic intermediates, including lipids, amino acids, organic acids, and other small signaling molecules, are the end products of cellular regulatory processes. Their concentrations can be altered by physiological/pathological conditions, and they can regulate various biological phenomena depending on their concentrations. Thus, these metabolites can act as functional entities within cell and tissues. Recent progress in mass spectrometry (MS) based metabolomics established a methodology that was capable of satisfying the required criteria to simultaneously analyze wide range of metabolites, regarding quantitative performance, high throughput and high sensitivity. Such metabolite profiling has been utilized in clinical, pharmacological, and functional genomic studies. These analytical methods, however, could not provide direct information regarding the 2-dimensional distribution of metabolites within cells and tissues. The traditional metabolomics usually employ biofluids or tissue samples after they have been subjected to homogenization, extraction, and purification and have completely lost their spatial information. In addition, such MS-based metabolomics often could fail to detect components which can be lost during purification process or insoluble components in buffers. However, obtaining 2-dimensional information regarding metabolite expression is essential to understand metabolic entity of body, because of the heterogeneous metabolic process among different cell types *in vivo*.

Imaging mass spectrometry (IMS; also referred to as mass spectrometry imaging; MSI), a MS-based molecular imaging technique, provides distribution information regarding various biomolecules at the cell and tissue levels. In particular, matrix-assisted laser desorption/ionization (MALDI)-IMS coupled with advanced mass analyzer facilitates the analysis of the complete chemical information of metabolites in tissue sections. This technique visualizes a large number of metabolite molecular species simultaneously on a single tissue section. Following advantages particularly facilitate IMS as practical imaging tool for metabolites; First, IMS does not require any specific chemical labels or probes. Second, IMS is a "*non-targeted*" imaging method. Finally, the simultaneous imaging of many types of metabolite molecules is possible, and all these features are necessary for the assessment of metabolite localization. Due to these advantages, this emerging imaging technique is increasingly being used for the imaging of small organic molecules though it was initially developed as a tool for protein imaging.

In the first part of this thesis (chapter 1-4), I report my exploration of metabolite distribution in tissues with IMS; as an impressive finding, I discovered that metabolite species even with quite similar chemical structures shows distinct distribution patterns. For example, in the mouse cerebellum, I found docosahexaenoyl-phosphatidylcholine (DHA-PC) with palmitic acid (represented as PC(diacyl-16:0/22:6)) which is an abundant membrane phospholipid, was specifically expressed by granule cells, while DHA-PC with stealic acid (PC(diacyl-18:0/22:6)) distributed as complementary patterns although their structural difference is only two additional carbon chains; the latter PC was selectively expressed by purkinje cells (Figure 2-6, in chapter 2).

These observations raise a fundamental question; do the localized small metabolites play specific functional roles to each cell-type *in vivo*? If so, how can we analyze them? To achieve this, in the latter part of this thesis (chapter 5), I analyzed dynamic changes of metabolites on neural stimuli, in their amount and distribution pattern. Differential analysis between control and stimulated samples tells us about "*what*" kind of metabolic pathways are involved in the neural activity on the stimuli, and more importantly, such analysis tells us "*where*" the stimulated metabolism was occurred in the tissues.

Using IMS and other technique, I established experimental system to profile the metabolite dynamics i.e., the fluctuation in their expression with time, *in vivo*. In particular, for lipids, I uncovered the region specific dynamics of specific lipids on the stimulation by IMS, conjunction with laser capture micro dissection (LCM) technology. I visualized the dynamics of phospholipids induced by kainate administration, which is widely used as a model of limbic seizures, in mouse hippocampus by IMS. In addition, LCM conjunction with enzyme immune assay (EIA) completes the micro region profiling of lipid metabolites, especially of extremely small amount lipids; bioactive lipids such as prostaglansins (PGs) regulate various physiological events at very low concentration, and their dynamics were also comprehensively analyzed within each hippocampal cell type. The results indicate poly-unsaturated fatty acids (PUFAs), especially arachidonic-acid (AA) were specifically released in the granule cell layer of dentate-gyrus (DG) in the mouse hippocampus.

Analysis of molecular flux between time and space is only a way to directly assess metabolism itself, and therefore, presented approaches will reveal diverse metabolic process in *vivo* and further give insight to their functional roles in the biological phenomena, towards *in situ* metabolomics.

Chapter 1: Visualization of metabolite distribution with imaging mass spectrometry

1. Introduction

Classical matrix-assisted laser desorption/ionization (MALDI) mass spectrometry (MS) have been applied to the analyses of a wide range of molecules with varied physical and chemical characteristics. Now this continuous advancing technology has been utilized into molecular imaging technique. With the unique and powerful detection principle by MS, MALDI-imaging mass spectrometry (IMS) can be used for the visualization of the distribution of large number of biomolecules in the cells and tissues, ranging from small metabolite molecules[1, 2] to much larger proteins.[3, 4]

This emerging imaging technique was initially developed as a tool for protein imaging.[5-7] Most of the reports concerning MALDI-IMS thus far describe the detection and imaging of proteins or peptides, in fact. On the other hand, research directed toward the detection and imaging of small metabolites has recently been expanding. Figure 1-1 shows the result of a PubMed search (reviews were excluded) using "imaging mass spectrometry" as key words. Reports are subdivided into groups according to the substances analyzed in the study, and the number of reports in each group is indicated. Notably, the number of reports regarding the IMS of metabolite compounds has gradually increased, and occupies half of the works published in 2007.

2. Advantages of MALDI-IMS in metabolite imaging.

Localization of transcripts is visualized with oligonucleotide probe *in situ*

hybridization, and localization of proteins is visualized using immunohistochemistry based on antibodies. IMS (including both MALDI- and secondary ion mass spectrometry (SIMS)-based IMS) is an emerging technique for imaging the distribution of small metabolites, including lipids, amino acids, organic acids, and potentially applied to any other small organic molecules. The emergence of IMS as a tool for metabolite imaging has much impact because we do not have an established technique ranging diverse metabolites (Table 1-1).

Following advantages particularly facilitates IMS as an outstanding metabolite-imaging tool in tissues or cells: First, IMS does not require any labels or specific probes; second, IMS is a non-targeted imaging method, thus, we can localize unexpected metabolites; finally, the simultaneous imaging of many types of metabolite molecules is possible. Given the enormous molecular diversity of metabolite species, a large number of which are even still unknown, all these features are necessary for the assessment of metabolite localization. In addition, using tandem MS analysis, the detailed structure of metabolite molecules can be identified directly on the tissue sections; thus, it can be confirmed that the observed mass signals are derived from the molecules of interest, [1, 8] and potentially, novel metabolites could be identified. Tandem MS is also effective for discriminating isobaric ions.[1, 2]

3. Workflow of imaging mass spectrometry

The workflow of MALDI-IMS is shown in Figure 1-2. Basically, researchers take thin tissue slices mounted on conductive glass slides and apply a suitable MALDI matrix to the tissue section. Next, the slide is inserted into a mass spectrometer. A focused laser beam is directed at predetermined positions in the tissue slice and the

mass spectrometer records the spatial distribution of molecular species (typically with 10–200 μm scan pitch). Automated data collection takes 2–6 h, depending on the number of points assayed. Suitable image processing software can be used to import data from the mass spectrometer to allow visualization of ion distribution image and comparison with the histological image of the sample.

4. Strategy of IMS for small metabolites

Today, the application of IMS to researching small organic compounds (m/z < 1000) can be subdivided into two distinct areas: (1) measurement of endogenous metabolites, and (2) measurement of exogenous drugs. MALDI-IMS is partiurally effective for profiling [9-11] and visualizing distribution [1, 12-14] of endogenous lipids such as glycerophospholipids (GPLs); they can also be imaged with SIMS [15-18]. For example, when a mouse brain section coated with 2,5-dihydroxybenzoic acid (DHB) solution was immediately analyzed by MS, strong peaks that are mainly derived from phospholipids were observed between mass region of 400 < m/z < 900 [9, 19, 20]. This is because phospholipids are ionized efficiently due to the following reasons; first, large amounts—more than 60% in dry weight—of the brain tissue consists of lipids. Second, these compounds have an easily ionizable structure; phospholipids, in particular, phosphatidylcholines [PCs] contain a phosphate group and trimethylamine that are easily charged [21].

GPLs comprise a large molecular family in which phosphoric acid is bound via ester formation to a glycerolipid (Figure 1-3). They are subdivided into distinct classes (e.g., PCs, phosphatidylethanolamines [PEs], and phosphatidylinositols [PIs]) based on the structure of their polar head group linked to the phosphate, attached at the *sn*-3

position of the glycerol backbone. They are further subdivided into numerous molecular species on the basis of the composition of the fatty acids linked to the *sn*-1 and *sn*-2 positions of the glycerol backbone.

Using IMS, we can image not only these multiple classes, but also related molecular species simultaneously. In particular, capability of IMS to determine the distinct localization of each molecular species, in other words, elucidation of distinct fatty acid composition of biological membranes in different tissue locations, is an important advantage of IMS. Since several types of fatty acids, especially polyunsaturated fatty acids (PUFA), in the phospholipids are released and converted into bioactive lipids in response to extracellular stimuli, which mediate various important biological processes [22], thus distinct distribution information of PUFA-containing phospholipids are quite valuable [23]. In the successive chapter, I explored characteristic distribution of these PUFA-containing phospholipids, and further their dynamic accumulation during neural development.

Figures and Tables for Chapter 1.
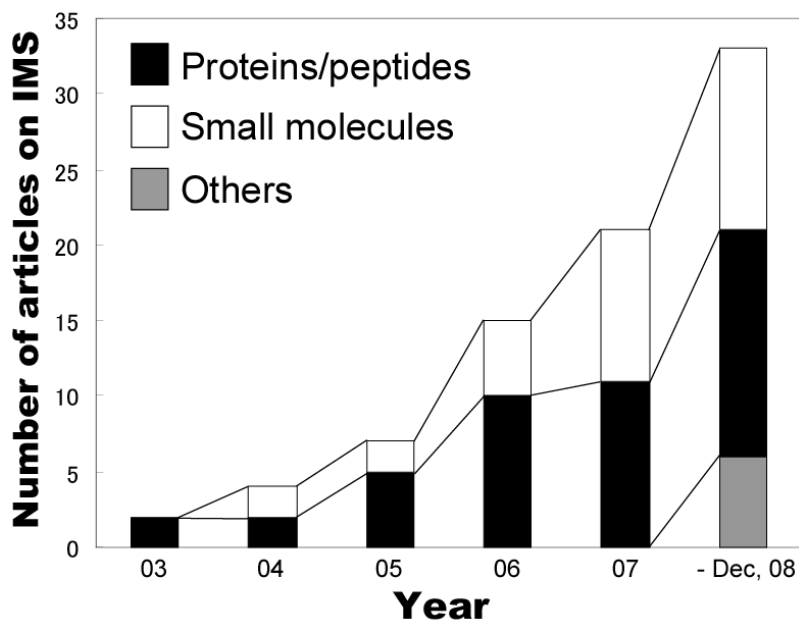
Figure 1-1: Result of the PubMed search using "imaging mass spectrometry" as keywords.
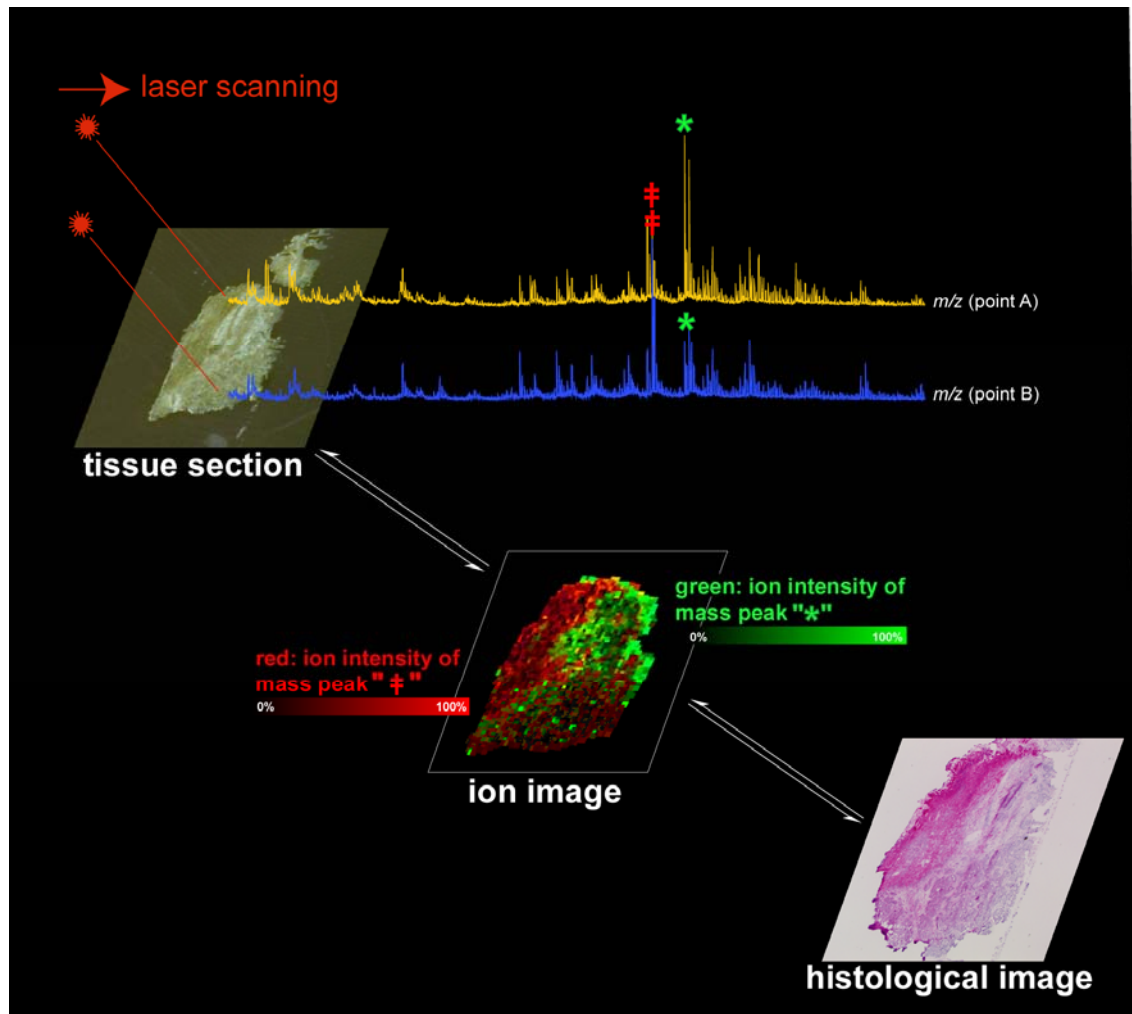
Figure 1-2: Schematic representation of MALDI-IMS procedures. Usually, tissue section mounted on an indium thin oxide (ITO) coated glass slide is covered with a specific MALDI matrix. Next, the ITO slide is inserted into a mass spectrometer. The MALDI laser scans through a set of preselected locations in the tissue (10–200 μm scan pitch) and the mass spectrometer records the spatial distribution of molecular species. Suitable image processing software can be used to import data from the mass spectrometer to allow visualization and comparison with the histological image of the sample. In this figure, green and red pixels represent the ion intensity of mass peaks labeled with " *" and " ‡ ", respectively.
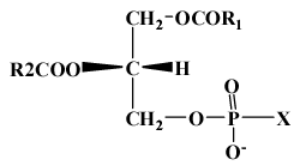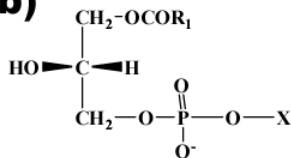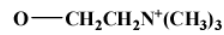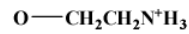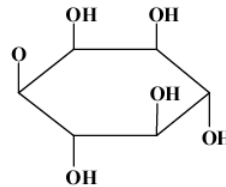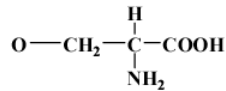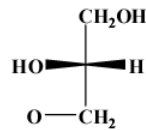
Figure 1-3: Structure of phospholipids.

Structures of the glycerol backbone of phospholipids (a) and lyso-phospholipids (b) are shown. They are subdivided into distinct classes (e.g., phosphatidylcholines, phosphatidylethanolamines, and phosphatidylinositols) based on the structure of the head group linked to the phosphate, attached at the sn-3 position of the glycerol backbone (c). They are further subdivided into numerous molecular species on the basis of the composition of fatty acids linked to the sn-1 and sn-2 positions of the glycerol backbone.

Table 1-1: Representative molecular imaging methods in tissues or cells.

	Representative methods	probe
DNA	FISH（fluorescence in situ hybridization）	oligo nucleotide probe
RNA	*in situ* hybridization	oligo nucleotide probe
protein	immunohistochemistry, green fluorescent protein-fused protein	antibody
metabolites (especially lipids)	imaging mass spectrometry	-

molecular diversity

Table 1-2: Imaging/detection of small metabolite molecules in tissues by MALDI and related ionization techniques.

Mapping of administered drug metabolism and its metabolite distribution by IMS is also attracting a lot of attention because of advantages over conventional imaging techniques, as will be discussed subsequently. In this area, so far, a number of studies regarding antipsychotics, cancer drugs, antianxiety drugs, and hypnotics have been reported

endogenous metabolites   **exogenous drugs**

glycerophospholipids;

PCs[1, 9, 19, 24, 25], PEs[20, 24, 25], PIs[20, 24, 25], PSs[20, 24, 25], PGs[20, 24] and caldiolipins [26]

complex lipid

glycosphingolipids

gangliosides[31, 32], sulfatides[20, 32, 33] and galactocyl-ceramide [34, 35]   **e.g.**   olanzapine (Antipsychotic)[2, 27],

Neutral lipids;   imatinib (Cancer drug)[27],

triacylglycerols [25], diacylglycerols [25] and cholesterol[24, 36]   vinblastine (Cancer drug)[28],

simple lipid   banoxantrone (Cancer drug)[29]

Fatty acids [37]   diazepam [30] and temazepam (Antianxiety drugs, Hypnotic)[30]

Other metabolites;

Amino acids[38], flavonoids[37, 38], oligosaccharides[37, 38], and heme[39 40]

Note: PC = phosphatidylcholine, PE = phosphatidylethanolamine , PI = phosphatidylinositol , PS = phosphatidylserine, PG = phosphatidyglycerol.

Chapter 2: Visualization of the cell-selective distribution of PUFA-containing phosphatidylcholines in mouse brain

1. Introduction

Much progress has recently been made in studies of brain lipids. Neural lipids play a role in synaptic vesicle fusion [41, 42], regulation of receptors and ion channels [43, 44], and formation of raft microdomains for neuronal cellular communications [23, 45, 46]. Among brain lipids, glycerophospholipids (GPLs) are the most abundant, comprising a large molecular family in which phosphoric acid in the ester form is bound to a glycerolipid. GPLs are subdivided into distinct classes (e.g., phosphatidylcholines [PCs] and phosphatidylinositols [PIs]) based on the structure of the polar head group. In brain membrane GPLs, much amount of PUFAs, such as arachidonic acid (AA) and docosahexaenoic acid (DHA), are stored at the sn-2 position in an asymmetrical manner [47]. Such PUFAs are mainly released from GPLs by the activity of phospholipase A_2 (PLA$_2$) [22], and are metabolized into various important bioactive lipids [23] involved in PUFA-mediated signaling pathways [48, 49]. The systemic analysis of diverse lipids, "lipidomics," plays a crucial role in understanding lipid signaling [50-52]. It is also crucial to determine the neuronal distributions of GPLs, especially PUFAs, to understand their possible roles in brain function. Until recently, however, lack of lipid visualization systems has made lipid distributions difficult to determine.

As above mentioned, IMS is a unique detection technique that discriminates structurally heterogeneous molecules by their masses [53, 54] and image them simultaneously. In admission, a recent breakthrough in statistical IMS [55-58] has enabled comprehensive imaging analysis of GPL molecular families.

This chapter presents an improved experimental procedure that further enables highly qualitative IMS. This technical improvement in IMS contributes towards *in situ* lipidomics, allowing profiling of large-scale changes in lipid composition or determining the topographical distribution of individual lipid species in neural cells. Using a presented procedure, I simultaneously differentiated and visualized the localizations of specific molecular species of GPLs in mouse brain sections. In particular, my novel observations on PUFA-PCs suggest the brain cell-selective production of specific PUFA-GPLs in specific brain regions.

2. Materials and Methods

Chemicals. Methanol, trifluoroacetic acid (TFA), potassium acetate, and lithium acetate were purchased from Wako Chemical (Tokyo, Japan). Calibration standard peptide and 2,5-dihydroxybenzoic acid (DHB) were purchased from Bruker Daltonics (Leipzig, Germany). Synthesized 17:0 lyso-PC was purchased from Avanti Polar Lipid (Alabaster, AL, USA).

Sacrifice of animals and tissue extraction. All experiments with mice were conducted according to the protocols approved by the Animal Care and Use Committee of the Mitsubishi Kagaku Institute of Life Sciences. The brains of male C57BL/6J Cr mice at the indicated ages (1 and 12 postnatal days, 7 and 96 postnatal weeks) were used. Mouse brains were extracted within a minute (typically in 40 seconds) after sacrifice. Post-mortem degradation of GPLs was observed within 15 minutes by IMS in a series of mouse brains extracted at different times (15, 30, 60, and 120 minutes, see also Supplemental Figure S1), presumably because of stimulation by PLAs under ischemic

conditions [59, 60]. The trimmed tissue blocks were immediately frozen in powdered dry ice, allowing tissues to be frozen without cracks, and stored at −80 °C until use.

Tissue section preparation. Tissues blocks were sectioned at −16 °C using a cryostat (CM 3050; Leica, Germany) to a thickness of 5 μm, as described in previous reports[61, 62]. Although brain blocks were held by an optimum cutting temperature (OCT) polymer, they were not embedded into it, because it was thought that any residual polymer on the tissue slices might degrade the mass spectra [62]. The frozen sections were thaw-mounted on indium-tin-oxide (ITO)-coated glass slides (Bruker Daltonics) and ITO-coated sheets (Tobi Co., Ltd., Kyoto, Japan). The slides were used for tandem time-of-flight (TOF/TOF) measurements and the sheets were used for quadrupole ion trap (QIT)-TOF measurements. Prepared sections were subjected to matrix application within 5 minutes.

Spray-coating of the matrix solution. A DHB solution (40 mg/mL DHB, 20 mM potassium acetate, 70% MetOH, 0.1% TFA) was used as the matrix solution for imaging of PCs. The matrix solution was sprayed over the tissue surface using a 0.2-mm nozzle caliber airbrush (Procon Boy FWA Platinum; Mr. Hobby, Tokyo, Japan). Matrices were applied simultaneously to the tissue sections that were to be compared to equalize analyte extraction and co-crystallization conditions. The distance between the nozzle tip and the tissue surface was held at 10 cm and the spraying period was fixed at 5 minutes. Approximately 100 μL of matrix solution were sprayed onto each brain section.

A properly handled spray-coating step created a uniform matrix crystal layer on the surface, and awareness of some technical points contributed to success. First, too small

a distance between the airbrush and the tissues (< 10 cm) often resulted in large droplets of matrix solution and inhomogeneous crystals (Supplemental Figure S2). Second, humidity is also important factor. Room humidity was held under 25% at room temperature (25 °C). High humidity tends to cause formation of needle-like crystals as shown in Figure S2C (> 80%, at room temperature).

Reduction of the generation of multiple molecular ions from a single PC molecular species by addition of an alkali-metal salt to the matrix solution. PCs undergo preferential cationization with alkalis to form metal-adduct molecules [9, 63, 64]. Because tissue sections are rich in sodium and potassium salts, such alkali-metal adduct phospholipids, rather than protonated molecules, are preferentially generated (Figure 2-1a). Molecular ionization with such multiple ion forms from a single species often perturbs IMS experiments for several reasons. First, the distribution image of GPLs might not reflect the actual distribution of GPLs but rather the heterogeneous distribution of salts. Second, since GPLs have many molecular species, a single peak might contain multiple types of ions. Indeed, for example, a protonated PC (diacyl-16:0/20:4) molecule is detected as having the same mass as a sodiated PC (diacyl-16:0/18:1) ion, at *m/z* 782 (Figure 2-1a). To overcome this problem, it is important to reduce the potential ion forms to a single alkali-metal adduct form. In this study, potassium salt was added to the matrix solution (20 mM potassium acetate). As a result, the molecular ion forms were limited to potassium adducts, and the spectra were simplified (Figure 2-1a, b). Consequently, the 2 types of PCs detected at *m/z* 782 described above could be separated at *m/z* 820 and *m/z* 798.

Tandem mass spectrometry. Molecular identification was performed with tandem mass spectrometry (MS^n) analysis using a QIT-TOF mass spectrometer (AXIMA-QIT; Shimadzu, Kyoto, Japan) to ensure molecular assignment only by mass. The MS^n analysis was performed directly on the mouse brain sections. Acquisition was performed in the mid-mass range mode (*m/z* 750 – 2000) at a stage voltage of 18 V in the negative-ion detection mode. Calibration was performed using an external calibration method. To perform accurate molecular identification of PC molecular species by using the QIT-TOF instrument, I performed MS^3 analysis following MS^2 analysis by using ions at $[M-59\ u]^+$, which correspond to the ions with neutral loss of trimethylamine groups. I assigned ions to PC molecules that showed neutral loss of phosphate acid groups (–124 u) during MS^3 analysis, because this loss indicates that the analyzed molecules contain trimethylamine and phosphate groups. Owing to the instrumental specificity of QIT devices, they cannot trap small ions (*m/z* < 200) in the "mid-range mode" and therefore cannot detect signals in the small *m/z* region during MS^n analysis.

IMS conditions. IMS was performed using a MALDI TOF/TOF-type instrument (Ultraflex 2 TOF/TOF; Bruker Daltonics) with modified laser focusing system. This instrument was equipped with a 355 nm Nd:YAG laser. The data were acquired in the positive reflectron mode under an accelerating potential of 20 kV using an external calibration method. Signals between *m/z* 400 and 1000 were collected. Raster scans on tissue surfaces were performed automatically using FlexControl and FlexImaging 2.0 software (Bruker Daltonics). The number of laser irradiations was 100 shots in each spot. Image reconstruction was performed using FlexImaging 2.0 software.

Spectrum normalization with TIC improves quantitation and visualization quality in IMS.

The addition of salt to the matrix solution effectively reduces the molecular ion forms of GPLs. However, salts interfere with the matrix-analyte crystallization process and thus lead to the development of heterogeneous crystals, which in turn results in spot-to-spot variance of signal intensities [65, 66]. This problem was solved using a spectrum-normalization procedure with TIC (Figure 2-2).

I performed spectrum normalization with TIC for each mass spectrum by using software that our research group developed. The obtained spectra were multiplied with arbitrary variables such that all spectra had equal TIC values (i.e., equal integral values of the measured m/z region [$400 < m/z < 900$]). Such TIC normalization is also available with the "Normalize Spectra" function of FlexImaging 2.0 software with filter function to exclude a number of noise spectra from the normalization process.

To evaluate the effect of the normalization procedure, I prepared a section of mouse brain homogenate that had a uniform distribution of biomolecules. Figure 2-2a shows the ion images for m/z 772.6 corresponding to PC (diacyl-16:0/16:0), with and without spectrum normalization. After the normalization procedure, the image was corrected such that the ion distribution was uniform throughout the section. The signal intensity was then plotted and found to have a Gaussian distribution. Spectrum normalization with TIC improved the results of the IMS of mouse brain sections. Figure 2-2b shows the ion images of a mouse brain section for PC (diacyl-16:0/16:0), with and without spectrum normalization. In the ion image without normalization, the ion distribution was heterogeneous, even between adjacent pixels. Furthermore, the signal intensity was found to decrease with time (arrowhead). In contrast, when the normalization procedure

was used, a clear ion-distribution pattern that correlated well with the anatomical features of the brain section was obtained.

LC/ESI-MS/MS. To identify the PC species, precursor ion scanning was performed using the 4000Q-TRAP instrument; these methods are effective for detecting PCs because characteristic fragment ions are generated by collision-induced dissociation (CID) [67] (for details regarding the experimental conditions, see materials & methods section of chapter 5).

Multivariate statistical analysis. An N-by-P data matrix was constructed from the intensity of N pixels and P peaks and then PCA was performed using MATLAB^{TM} software (Mathworks, Inc., Sherborn, MA, USA) (for details, see supplemental information).

3. Results

Determination of the composition of PC molecular species in the mouse brain.

First, IMS of sagittal mouse brain sections was performed using the positive ion detection mode, and approximately 150 mass peaks in the mass range of $700 < m/z < 900$ (Figure 2-3a) were detected. Among these, nine intense mass peaks were assigned using their masses to abundant PC molecular species and one sphingomyelin, all of which contain a trimethylamine head group. In addition, these assignments were verified with structural analysis of each peak using MS^n (Figure 2-3b). For this purpose, a QIT-TOF mass spectrometer was used. This instrument can identify molecules using a highly sensitive MS^n from mixture ions generated on the tissue surface [8]. Table 2

summarizes the results of MS and MS[n]. In each mass peak, the presence of a trimethylamine head group and phosphate was confirmed (neutral losses [NL] of 59 u and 124 u from precursor ions, corresponding to trimethylamine and cyclophosphate, respectively), and are used as diagnostic ions in product ion mass spectra [8, 68, 69] (Figure 2-3).

In addition, I determined the accurate abundance ratios for PC-molecular species in the mouse brain. For this purpose, LC/ESI-MS/MS was employed, which enabled quantitative analysis of GPLs and identification of the fatty acids linked at the *sn*-1 and *sn*-2 positions [70]. Table 2-1 summarizes the quantitative composition of PC molecular species in the total brain lysate.

Distinct distributions of phosphatidylcholine molecular species in the mouse brain

Next, the tissue distributions of the nine major PC molecular species in the entire brain sections were visualized. For this purpose, a TOF/TOF mass spectrometer was used that had high sensitivity in single-stage MS. Figure 2-4 shows the IMS results for the primary brain PCs. While the most abundant molecular PC species, PC (diacyl-16:0/18:1), was uniformly distributed across the entire gray matter region of each section, other PC molecular species showed rather heterogeneous distribution patterns. In particular, the PUFA-PCs, which are both AA-PCs and DHA-PCs, showed characteristic patterns. Three AA-containing species, PC (diacyl-16:0/20:4), PC (diacyl-18:0/20:4), and PC (diacyl-18:1/20:4), were abundant and commonly concentrated in the pyramidal and granular cell layer regions in the hippocampal formation (arrowheads). Two DHA-containing species, PC (diacyl-16:0/22:6) and PC (diacyl-18:1/22:6), were abundant and were commonly enriched in the granule cell layer

of the cerebellum, while PC (diacyl-18:0/22:6) showed a characteristic dotted distribution pattern near the same layer. Among PCs with mono-unsaturated fatty acids (MUFA), PC (diacyl-16:0/18:1) was enriched in the white matter or in the region containing the myelin sheath.

PUFA-containing PCs were highly detected in specific neural cell types

The characteristic localization of PUFA-containing PCs was then determined. To study their distribution in more detail, high-magnification IMS was performed at instrumental raster step size (raster size) of 15 μm. In the magnified images of the hippocampal formation, all 3 abundant AA-PCs were found in the regions corresponding to the hippocampal cell layers, i.e., the pyramidal and granule cell layers of the dentate gyrus (DG) (Figure 2-5). On the other hand, PC (diacyl-16:0/16:0) was enriched outside of the pyramidal and granule cell layers (Figure 2-5b). Also, an intensive dotted distribution pattern of PC (diacyl-18:0/22:6) was observed in the cerebellum (Figure 2-4). Using high-magnification IMS of the cerebellar cortex, PC (diacyl-18:0/22:6) was found to be enriched in the Purkinje cell layer (Figure 2-6). Optical observation of successive HE-stained brain sections also suggested that PC (diacyl-18:0/22:6) was selectively detected in Purkinje cells (Figure 2-6, arrowheads) and in molecular layers in which dendrites of Purkinje cells exist. In contrast, granule cells were impoverished in PC (diacyl-18:0/22:6). Interestingly, a complementary distribution of two other abundant DHA-PCs, PC (diacyl-16:0/22:6) and PC (diacyl-18:1/22:6), was observed in the granule cells of the cerebellum (Figure 2-6c, d).

Statistical analysis revealed temporal and spatial changes in PCs with age

Having demonstrated the cell-selective distribution of PUFA-PCs in the adult mouse brain, changes in the distribution and amount of PC molecular species at various ages were evaluated. Studies of humans and several other mammalian species have shown that some PUFAs, including AA and DHA, are selectively incorporated and accumulated in GPL bilayers during brain development [71-74], but information on the locations of these PUFAs in the brain has not been available. Knowledge of when and where the changes occur would provide insight into the possible functions of PUFAs at specific brain locations. PC molecular species were comprehensively analyzed and their PUFA-PC distribution patterns and amounts in a developmental series of brain sections were obtained post-natally at 3 days, 12 days, 7 weeks, and 96 weeks.

To extract important information from such large IMS data sets (40000 data points for the 4 developing brain sections), Principle Component Analysis (PCA), an unsupervised multivariate data analysis technique [57, 58, 75], was used. PCA is useful for obtaining an overview of entire data sets (i.e., general trends in fluctuations in GPLs' expression with development) before proceeding to a more detailed data analysis (i.e., visualization of individual GPLs). For a detailed description of the procedure and results of PCA, see also chapter 4. Table 2-3 summarizes the results and interpretation of the PCA. To locate the brain regions or developmental time points with spectral fluctuations, the principal components were score by color at each data point (Figure 2-7, top line of each panel). It was assumed that components 2, 3, and 4 contained important information because of their heterogeneous distributions of component scores among sections. Eventually, it was determined that they represented three significant trends in PC expression changes.

Characteristic SFA/MUFA-PC expression patterns during brain development

As the first trend, component 2 represents the reduction of PCs with C14-16 fatty acids (myristic and palmitoyl acid) and the accumulation of myelin-constituting PCs with development. The inset of Figure 2-7a shows that the component 2 scores for spectra in the infant brains (P1 and P12; P, postnatal day) were higher than those in the adult brains (7 and 96 weeks old). As Table 3 suggests, PCs with C14-16 fatty acids, namely PC (diacyl-14:0/16:0) and PC (diacyl-16:0/16:1), along with a myelin-constituting PC, namely PC (diacyl-18:0/18:1), were suggested to be associated with the statistical difference in the component score. As expected, the visualization of each molecular species showed drastic reductions in PC (diacyl-14:0/16:0) and PC (diacyl-16:0/16:1), especially in the cerebral cortex, and their levels in the adult brains were quite low (arrowheads). On the other hand, PC (diacyl-18:0/18:1) accumulated in the white matter with myelin formation, especially in the callous corpus and in the medulla and white matter of the cerebellum (arrows).

Characteristic PUFA-PC distribution patterns during brain development

Second, component 3 represents the accumulation of AA-PCs during the formation of the hippocampus, cerebral cortex, corpus striatum, and granule cell layer of the cerebellum. As with the component 2 analysis, the focus was on the increase in component 3 score with development in the above-mentioned regions (Figure 2-7b inset). In this principal component, AA-PCs, namely PC (diacyl-16:0/20:4) and PC (diacyl-18:0/20:4), largely contributed to the statistical changes (Table 2-3). Visualization confirmed that the expression levels of the AA-PCs were certainly increased, especially in the hippocampal cell layers and corpus striatum. As

27

the arrowheads indicate, a faint localization observed at P1 had progressed in P12 and was clearly identified in the adult brains.

Finally, component 4 represents the accumulation of DHA-PCs in the cell layers of the cerebellum. Component 4 scores clearly trended higher in the cerebellar cortex, especially in the molecular and granule cell layers. In this case, DHA-PCs, namely, PC (diacyl-16:0/22:6) and PC (diacyl-18:0/22:6), were expected to be associated with the statistical difference in the component score (Table 2-3). In particular, PC (diacyl-18:0/22:6), which was contained in the soma and dendrites of Purkinje cells, progressively became enriched and formed a dotted distribution pattern in the cerebellum, while at P1, it was distributed at the surface of the cerebellar cortex (arrows) where immature Purkinje cells can be found. Also, PC (diacyl-18:0/22:6) progressively accumulated in the granule cell layer of the cerebellum (arrowheads). In addition to PCA, other multivariate analyses were performed, namely ICA (Supplemental Figure S6 and Table 2-4). Although PCA extracted the information most efficiently, ICA also identified other trends in expression changes summarized in Table 2-4. As a consequence, both multivariate analyses characterized the accumulation of PUFA-PCs in specific regions from total expression changes.

4. Discussion

IMS is an effective tool for lipid imaging

In this report, a practical method using IMS was introduced for visualize GPL distribution in the mouse brains, and the capability of IMS was demonstrated as a potential standard technology for lipid imaging. Applying the technique, the distribution

patterns of GPL molecular species in various regions of the mouse brain were comprehensively determined, and an atlas of distribution map was generated.

As mentioned in previous chapter, IMS is effective for detecting [9-11] and visualizing GPLs [1, 12-14]. A large amount of GPLs in the brain (more than 50% dry weight) and an easily charged structure (e.g., phosphate ester) yields high-ionization efficiency. In particular, in the positive-ion detection mode, molecular species of choline-containing lipids (e.g., PC, lyso-PC, and sphingomyelin) are highly ionized due to their trimethylamine head group[21]. Despite the promising capability of IMS for GPL imaging, improvement in its quantitative ability and reproducibility are necessary due to the nature of MALDI-direct MS. For example, excess endogenous salts and their tissue localizations perturb the ion images of specific molecules. The present study demonstrated that adding an alkali-metal salt to the matrix solution is an effective way minimize molecular ion adducts (Figure 2-1). Also, complex analyte-extraction and crystallization processes on the tissue surface generate spot-to-spot variances in analyte ionization efficiency. In addition, an IMS experiment with a large number of data points takes a long time (< 8 hours), and therefore, the sublimation of matrix crystals occurs (especially in a high vacuum chamber). This results in a decrease in signal intensity as shown in Figure 2-2c. The study results demonstrated that spectrum normalization using TIC is effective in correcting heterogeneous ionization efficiency (Figure 2-2). In a protein study, Norris et al. previously reported that spectrum processing, including a normalization process, is effective in improving IMS-data [76]. The present results demonstrated that, in lipid study, the normalization process eliminated spot-to-spot variances in signal intensity on the brain homogenate section (Figure 2-2a), and improved both qualitative and the semi-quantitative ability (Figure 2-2b) even among

different sections. For the absolute quantification of micro-region GPLs, further studies such as those using microdissection technology and LC/ES-MS/MS are required.

Visualization of GPL distributions revealed characteristic localizations of PUFA-PCs

A properly performed IMS experiment can generate ion distribution maps that are informative for exploring GPLs in a tissue section. By employing this technique, a number of PC molecular species were visualized simultaneously in a mouse brain section, and the distribution patterns of the species were found to be quite heterogeneous (Figure 2-4). The most impressive finding is that some PUFA-PCs were selectively obtained by specific cells (Figures. 2-3 and 2-4).

Among the classes of GPLs, PCs are the most abundant structural component of neural and glial cell membranes, and the fatty acid constituents of PCs (i.e., molecular species) influence the membrane's physical properties, including fluidity and curvature [16, 23, 77, 78].

Thus the cell-type heterogeneity of the fatty-acid constituent in part reflects the cells' heterogeneous membrane properties. Figure 2-6 shows that PC (diacyl-18:0/22:6) was contained in Purkinje cells in the cerebellum. Both ion and optical images indicate that this DHA-containing PC molecular species was highly contained not only in the soma but also in the dendrites of Purkinje cells. Because of its high degree of unsaturation, DHA-GPLs increase membrane fluidity and even regulate the functions of membrane-associated proteins [79-81]. Purkinje cells are the largest neurons in the brain, with intricately elaborate dendritic arbors. Thus, higher membrane fluidity may be required for effective transport of membrane-associated proteins via the plasma

30

membrane. Thus, the high-level expression of DHA-PC may contribute to the transportation of membrane proteins in the cells.

Also, it is well known that GPLs, including PCs, serve as reservoirs of PUFAs, which are released and converted into bioactive lipids in response to extracellular stimuli, and which mediate various important biological processes [22]. Thus, the cell-type specificity of PUFA storage constituents is worth describing. Figure 2-5 shows that arachidonic acid (AA)-containing PCs are enriched in the cell layers of pyramidal neurons of CA1 and of granule neurons of DG. The prominent detection of AA-PCs in such cells suggests the storage of large amounts of AA. Judging from their localization pattern, they are presumably enriched in the nuclear membranes of the cells. In fact, AA is known to be selectively incorporated and enriched in the PCs of the nuclear membrane [82]. From nuclear PCs, AA is released into the cytoplasm by PLA_2 activity in response to extracellular stimuli, facilitating the initiation of the AA cascade [22]. Thus, a high concentration of AA-PCs in the hippocampal cell layer indicates the necessity of producing large amounts of eicosanoids for neural activity in the hippocampal formation.

Visualization of spatio-temporal-changes of GPL composition by IMS

Neural cell membranes are dynamic entities whose lipid constituents are continuously adjusted [74]. The fatty acid composition of tissues is known to change throughout development, and the changes differ among the classes of GPLs [71-74]. The novelty of the present study is that, by visualizing these changes, functional insight was obtained into these biochemical processes. For example, a previously reported developmental increase in oleic acid (18:1) was revealed by IMS to result from the accumulation of PC

31

(diacyl-18:0/18:1) in the myelin-containing region during maturation (Figure 2-7a). Furthermore, even alterations in microdomains could be identified, which are difficult to separate using conventional biochemical approaches. Although previous studies have shown that increases in the levels of AA and DHA are relatively small in the total brain lysate, the present study found that enrichment occurred in a quite region-specific manner. AA and DHA were observed to accumulate primarily in the cell layers of the hippocampal formation and cerebellum, respectively (Figure 2-7b), presumably in the nuclear membrane, during functional maturation. Such dynamic changes in GPL composition may be attributed to the temporal and heterogeneous expression of the lysophospholipid acyltransferase family, which have been recently characterized [83]. Further study focused on fluctuations in expression of these enzymes with time and location coupled with the presented distribution map is needed to understand how GPL diversity is established with development.

This chaoter focused on PCs because of the space limitations, however, analyses of other GPLs and glycosphingolipids, including phosphatidylethanolamine (PE), phosphatidylinositol (PI), phosphatidylserine (PS), and sulfatides (STs), are also available, as shown in Supplemental Figures S4 and S5. As a result of the technical improvement described in this chapter, an atlas could be provided of these GPLs over time and space. For PCs, distribution maps were generated that cover multiple molecular species at various ages and brain regions. This data set indicates the necessity of region-specific studies in brain lipidomics, and provides important information for performing such analyses.

Figures and Tables for Chapter 2.
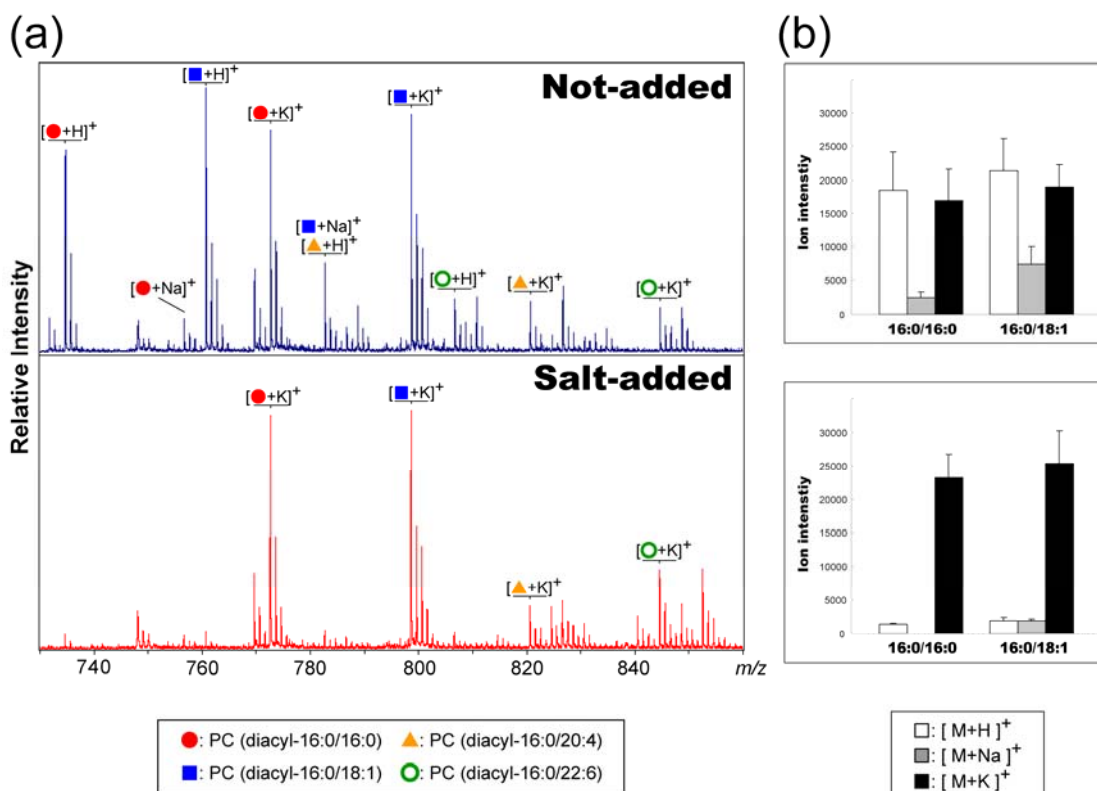
Figure 2-1: Generation of multiple molecular ions from a single PC molecular species was reduced by adding an alkali-metal salt to the matrix solution.

a, Spectra obtained from sections of mouse brain-homogenate using matrix solution with/without potassium acetate. The use of the salt-added matrix solution allowed multiple molecular ion-forms of PCs to be reduced to a single potassiated molecular ion form. *b,* Ion intensities of two PC species, PC (diacyl-16:0/16:0) and PC (diacyl-16:0/18:1), in three molecular ion forms, protonated, sodiated, and potassiated molecules
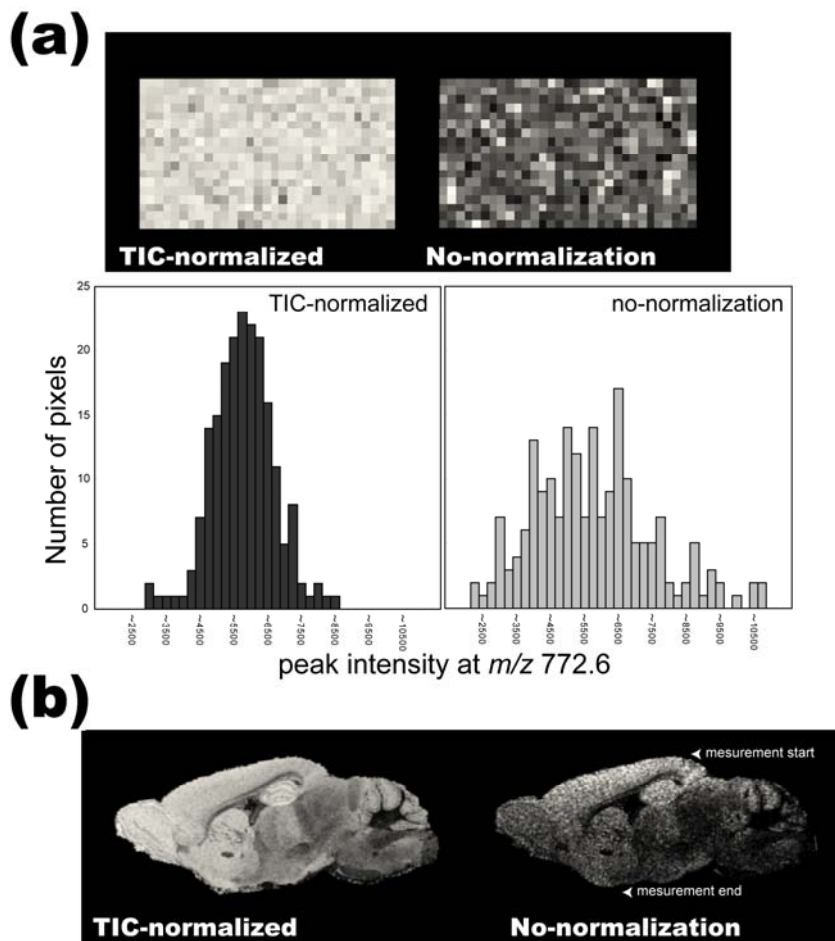
Figure 2-2: Spectrum normalization using TIC improves both the quantitative ability and visualization quality of IMS.

a, IMS results for PC (diacyl-16:0/16:0) on a section of mouse brain homogenate, processed with/without TIC-normalization (upper panel), and plot of ion-intensity distribution for PC (diacyl-16:0/16:0) obtained from a brain-homogenate section, with/without TIC-normalization (lower panel). *b*, Ion images of PC (diacyl-16:0/16:0) on an adult mouse brain section, in which spectra were processed with/without TIC normalization.

(a)

PC(diacyl-16:0/18:1)

PC(diacyl-16:0/16:0)

PC(diacyl-18:1/20:4)

PC(diacyl-16:0/22:6)

PC(diacyl-18:0/22:6)

SM(18:0)

PC(diacyl-16:0/20:4)
PC(diacyl-18:0/18:1)

PC(diacyl-18:0/20:4)

PC(diacyl-18:1/22:6)

Relative Intensity

700   750   800   850   *m/z*

(b)

m/z 744.4 → PC(diacyl-30:0)

m/z 770.4 → PC(diacyl-32:1)

m/z 772.4 → PC(diacyl-32:0)

m/z 796.4 → PC(diacyl-34:2)

m/z 798.4 → PC(diacyl-34:1)

m/z 820.5 → PC(diacyl-36:4)

m/z 826.5 → PC(diacyl-36:1)

m/z 844.5 → PC(diacyl-38:6)

m/z 846.5 → PC(diacyl-38:5)

m/z 848.5 → PC(diacyl-38:4)

m/z 870.6 → PC(diacyl-40:7)

m/z 872.6 → PC(diacyl-40:6)

Figure 2-3: Primary PC molecular species simultaneously detected in mouse brain sections by IMS.

a, An averaged mass spectrum obtained from an entire mouse brain section. In the spectrum, intense mass peaks corresponding to 9 abundant PCs were assigned according to mass. *b*, Results of MS^n structural analysis of ions corresponding to the PCs. Both MS^2 and MS^3 product ion spectra show that the mass peaks are derived from the PCs. Neutral losses (NL) of 59 u and 124 u from precursor ions, corresponding to trimethylamine and cyclophosphate, respectively, were used as diagnostic ions. Also refer to Table 2-2.
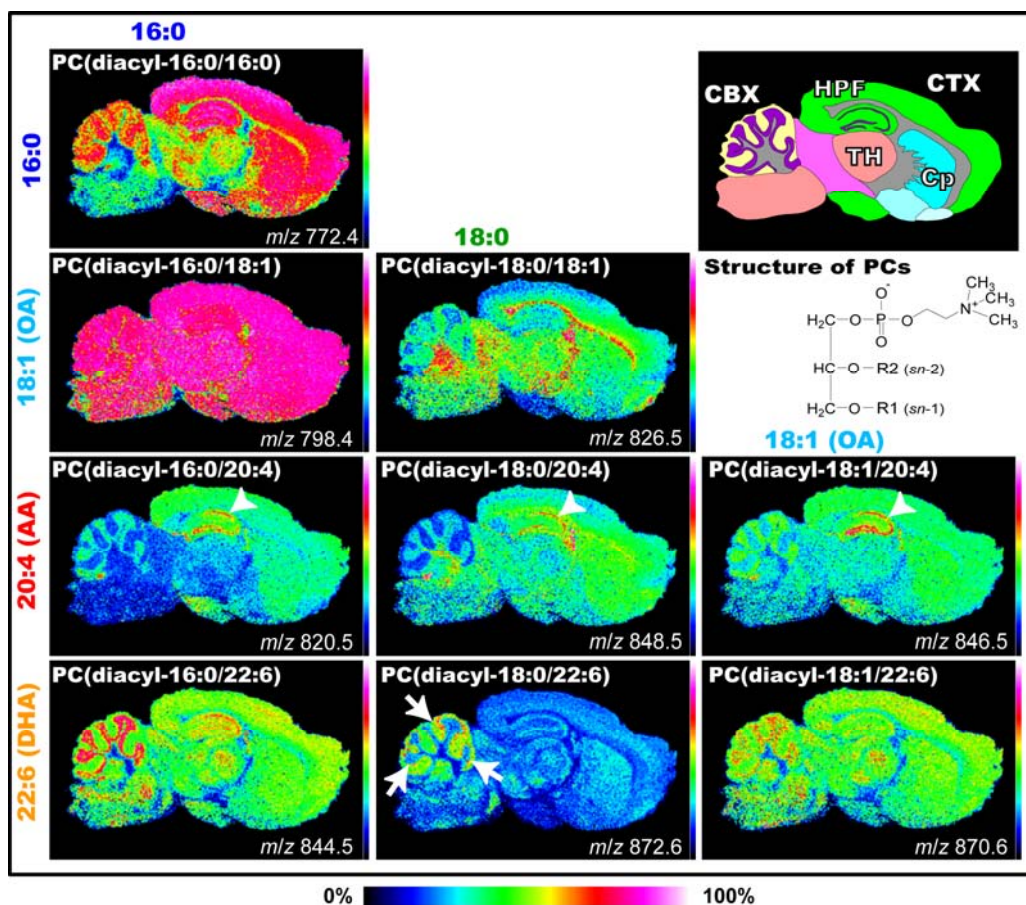
Figure 2-4: Differential distribution of PC molecular species in sagittal mouse brain sections.

MALDI-IMS spectra of a brain section simultaneously identified the heterogeneous distributions of several PCs. Schema of the mouse brain sagittal section and ion images of PCs obtained by IMS are shown. Ion images of PCs are arranged according to their fatty acid (FA) composition. PCs with identical FA compositions at the sn-1 position are arranged lengthwise, while those with identical FA compositions at the sn-2 position are arranged sideways. The structures of PCs are also presented. Among the PCs, AA-PCs showed characteristic localization in the hippocampal cell layers (arrowheads). Among DHA-containing species, two abundant species, PC (diacyl-16:0/22:6) and PC (diacyl-18:1/22:6), were commonly enriched in the granule layer of the cerebellum, while PC (diacyl-18:0/22:6) showed a characteristic dotted distribution pattern near the cell layer (arrows). CBX, cerebellar cortex; CP, corpus striatum; CTX, cerebral cortex; HPF, hippocampal formation; TH, thalamus.

37

(a) HE-stained
CA1
DG

(b) PC(diacyl-16:0/16:0)

(c) PC(diacyl-16:0/20:4)

(d) merged
100%
34%
0%

(e) PC(diacyl-18:0/20:4)

(f) merged
100%
23%
0%

(g) PC(diacyl-18:1/20:4)

(h) merged
100%
19%
0%
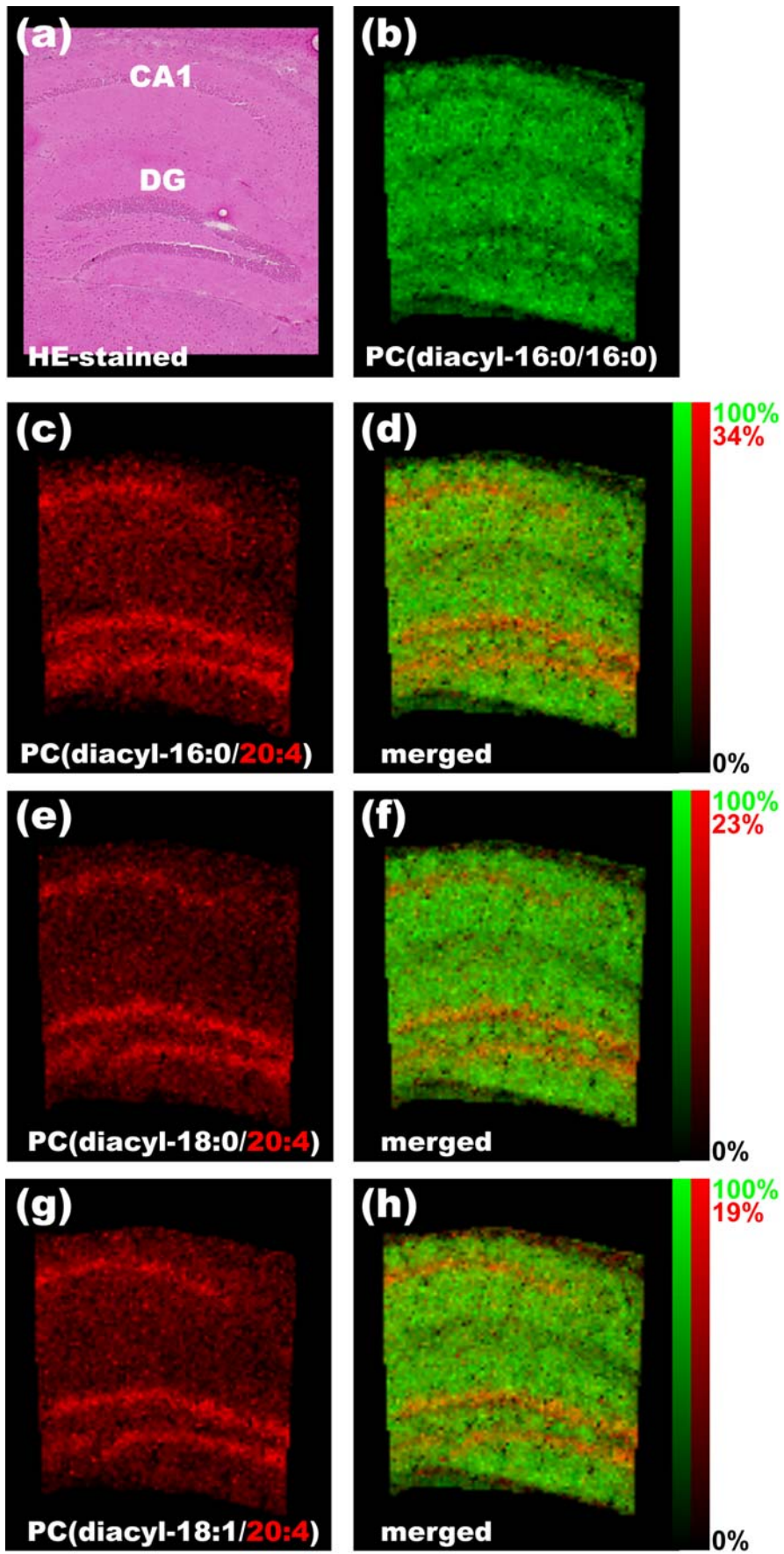
Figure 2-5: AA-containing PCs are localized in the cell layers in the hippocampal formation.

High-magnification IMS at a raster size of 15 μm (*c, e, g*), and successive section stained with HE (*a*) revealed that AA-containing PCs were enriched in the cell layer regions of the hippocampal formation, which are the pyramidal cell layer of CA1 and the granule cell layer of DG, while PC (16:0/16:0) was widely distributed in the dendritic region of the hippocampal formation (*b*). *d, f, h*, Merged images. The relative abundance of the 2 ions is indicated in the color scale bar.
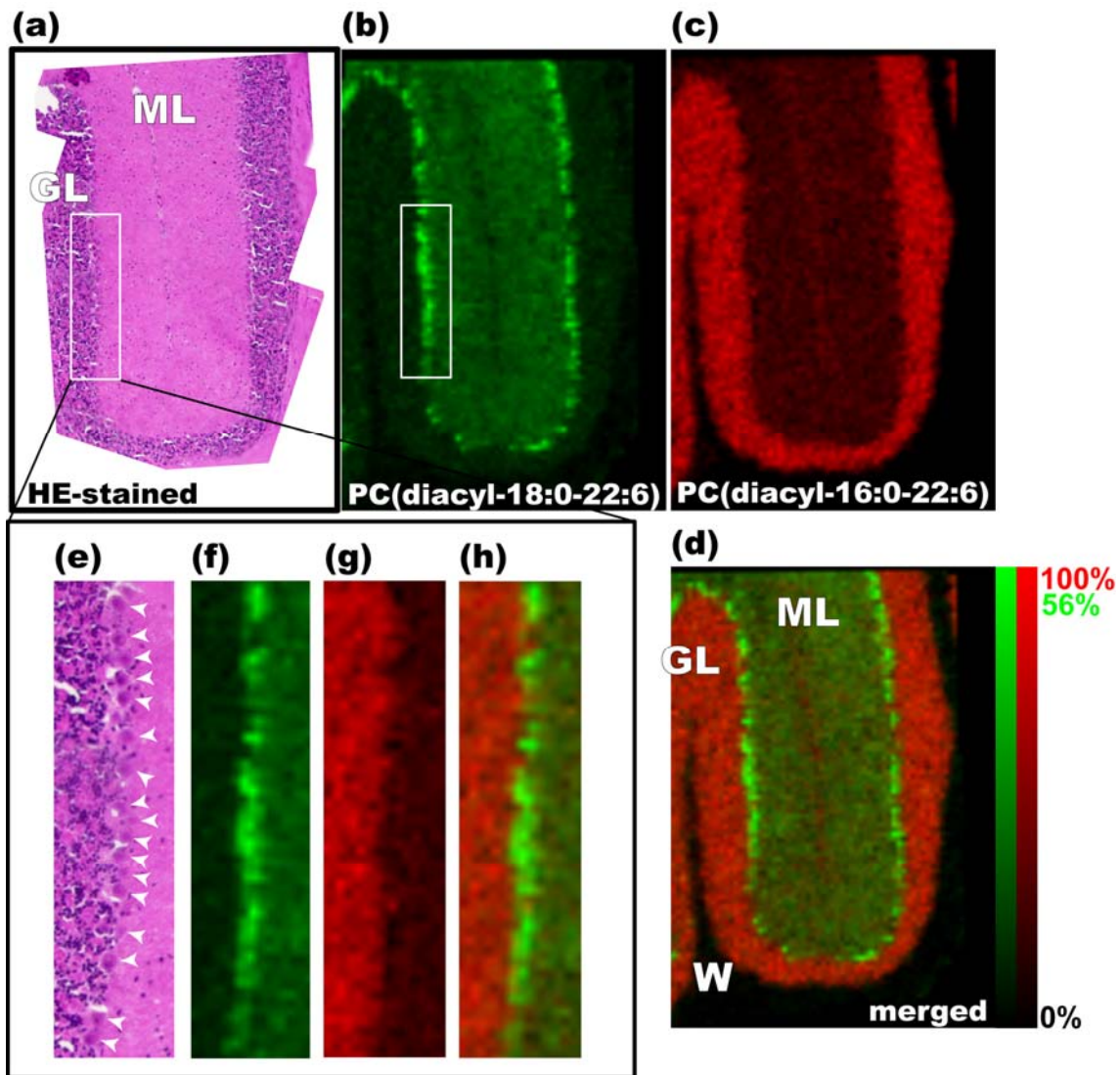
Figure 2-6: Purkinje cells selectively contained a DHA-containing PC.

High-magnification IMS at a raster size of 15 µm revealed the Purkinje cell-selective distribution of PC (diacyl-18:0/22:6) in the cerebellum. Both optical observation of HE-stained successive brain sections (*a, e*) and ion images of DHA-PCs (*b, f*) clearly suggest that the PC was enriched in the Purkinje cell layer (arrowheads). Interestingly, a complementary distribution of another abundant DHA-PC, PC (diacyl-16:0/22:6), was enriched in the granule layer of the cerebellum (*c, g*). *d*, Merged image. ML, molecular layer; GL, granule layer; W, white matter. The relative abundance of the 2 ions is indicated in the color scale bar.

(a) Principle component 2

p-1 day p-12 days p-7 weeks p-96 weeks

component score

Principle component 2

MS intensity

m/z 744.4
PC(diacyl-14:0/16:0)

m/z 770.4
PC(diacyl-16:0/16:1)

m/z 826.5
PC(diacyl-18:0/18:1)

(b) Principle component 3

component score

Principle component 3

MS intensity

m/z 820.5
PC(diacyl-16:0/20:4)

m/z 848.5
PC(diacyl-18:0/20:4)

(c) Principle component 4

p-1 day p-12 days p-7 weeks p-96 weeks

component score

Principle component 4

MS intensity

m/z 872.6
PC(diacyl-18:0/22:6)

m/z 844.5
PC(diacyl-16:0/22:6)

P3 P12 7 weeks 2 years

MS-intensity
0% 100%

Component score
Low High

41

Figure 2-7: IMS-PCA analysis of the developmental mouse brains revealed dynamic changes in PC expression.

IMS was performed on a developmental series of four mouse brain sections, obtained post-natally on days 3 and 12 and in weeks 7 and 96, and then PCA was performed to extract general trends in PC expression fluctuation during development. Three trends emerged. *a*, PC2 represents a reduction in PCs with short-chain fatty acids and an accumulation of myelin-constituted PCs with development. *b*, PC3 represents an accumulation of AA-PCs in the hippocampal formation, cerebral cortex, corpus striatum, and granule cell layer of the cerebellum. *c*, PC4 represents an accumulation of DHA-PCs in the cell layers of the cerebellum. In each panel, the upper row illustrates the principal component score for each pixel, and the lower rows show the results of individual visualizations of PCs that have large loading factors for each principal component. The brain sections were HE-stained and optical images of the sections are shown.

Table 2-1: Molecular species of PCs from mouse whole brain lysate identified by UPLC/ESI-MS/MS (n = 3)

molecular species	Relative abundance	S.D.
16:0/18:1	100	
16:0/16:0	58.5	4.4
18:0/18:1	48.2	2.5
16:0/22:6	35.1	3.2
16:0/20:4	29.3	3.8
18:0/22:6	19.8	1.8
18:0/20:4	14.7	0.8
18:1/20:4	10.2	1.5
18:1/22:6	8.5	0.7

Table 2-2: Results of MS and MS^n with the intense mass peaks obtained directly from the mouse brain sections

observed mass	observed ions in MS^2	observed ions in MS^3	assigned molecular species
772.4	713.1	588.9	[PC(diacyl-16:0/16:0)+K]$^+$
798.4	739.3	615.1	[PC(diacyl-16:0/18:1)+K]$^+$
820.5	761.3, 637.0	637.0	[PC(diacyl-16:0/20:4)+K]$^+$
826.5	767.3	643.0, 605.0	[PC(diacyl-18:0/18:1)+K]$^+$
844.5	785.3	661.0, 623.0	[PC(diacyl-16:0/22:6)+K]$^+$
846.5	787.4	663.2	[PC(diacyl-18:1/20:4)+K]$^+$
848.5	789.4	665.2	[PC(diacyl-18:0/20:4)+K]$^+$
870.6	811.5, 687.3	687.3	[PC(diacyl-18:1/22:6)+K]$^+$
872.6	813.4	689.1	[PC(diacyl-18:0/22:6)+K]$^+$

Table 2-3: Results and interpretation of PCA of the developing mouse brain

	Primary contributing PCs			Interpretation of the component
Component 2	PC(diacyl-14:0/16:0)	PC(diacyl-16:0/16:1)	PC(diacyl-18:0/18:1)	Reduction in PCs with short-chain fatty acids and accumulation of myelin-constituted PCs
Component 3	PC(diacyl-16:0/20:4)	PC(diacyl-18:0/20:4)	PC(diacyl-16:0/18:1)	Accumulation of two abundant AA-PCs in the hippocampus, cerebral cortex, corpus striatum, and granule cell layer of the cerebellum
Component 4	PC(diacyl-18:0/22:6)	PC(diacyl-16:0/22:6)	PC(diacyl-18:1/22:6)	Accumulation of DHA-PCs in the cerebellum

Table 2-4:Results and interpretation of ICA of the developing mouse brain

	Primary contributing PCs			Interpretation of the component
Component 1	PC(diacyl-16:0/18:1)	PC(diacyl-16:0/16:0)	PC(diacyl-16:0/18:0)	Accumulation of PCs with SFA and MUFA
Component 2	PC(diacyl-18:0/18:1)	PC(diacyl-14:0/16:0)	PC(diacyl-16:0/16:1)	Reduction in PCs with short-chain fatty acids and accumulation of myelin-constituted PCs
Component 3	PC(diacyl-16:0/20:4)	PC(diacyl-18:0/20:4)	PC(diacyl-32:1)	Accumulation of two abundant AA-PCs in the hippocampus, cerebral cortex, corpus striatum, and granule cell layer of the cerebellum

Chapter 3: Visualization of Age-dependent Accumulation of C20-Ganglioside Molecular Species in the Mouse Hippocampus

1. Introduction

Gangliosides are glycosphingolipids consisting of mono- to poly-sialylated oligosaccharide chains of variable lengths attached to a ceramide unit. They are inserted in the outer layer of the plasma membrane with the hydrophobic ceramide moiety acting as an anchor, while their oligosaccharide moiety is exposed to the external medium [84]. Gangliosides are particularly abundant in the central nervous system (CNS) and are thought to play roles in memory formation [85], neuritogenesis [86], synaptic transmission [87], and other neural functions. In addition, they are particularly involved in brain development and maturation [88, 89].

Gangliosides comprise a large family (Figure 3-1); their constituent oligosaccharides differ in the glycosidic linkage position, sugar configuration, and the contents of neutral sugars and sialic acid. Based on the number of sialic-acid contained, they subdivided into GM (i.e. mono-sialilated), GD (di-sialilated), GT (tri-sialilated) and GQ(quadra-sialilated) groups. The oligosaccharide unit is important because gangliosides interact with proteins that participate in signal transduction through membrane microdomains. For example, the ganglioside GM3 has been found to be closely associated with signaling proteins, such as c-Src, Rho, FAK, and Ras, in cultured cells [86, 90, 91], and GD3 is associated with the Src-family kinase Lyn and the neural cell adhesion molecule TAG-1 in rat brain [92, 93].

The ceramide moiety of gangliosides also varies with respect to the type of long-chain base (LCB) (sphingosine base) and fatty acid moiety. Such structural heterogeneity results in part from the different chain lengths, especially of the LCB (See

also Figure 3-1b). While some complex mammalian sphingolipids such as C18-sphingosine, i.e., C18-LCB species, are distributed in all tissues, C20-sphingosine (C20-LCB species) is present in significant amounts only in the gangliosides of the nervous system [94-97], and its content increases throughout life [98-100]. This structural heterogeneity of ceramides allows flexibility for performing different cellular functions, for example, cAMP-mediated signal transduction[101]. Thus, it has been suggested that C18- and C20-gangliosides are differentially regulated and might play different roles in neuronal function *in vivo* [94].

At present, few methods exist for the holistic study of the distribution of these ganglioside molecular species in biological specimens. Antibodies to some oligosaccharide moieties are available for visualizing the molecular species with different constituent oligosaccharides [102], but immunological methods cannot detect the differences in the ceramide structure, which is hidden in the lipid bilayer.

In this respect, IMS of biological tissues by using MALDI is a useful method. It can distinguish between different ganglioside molecular species by determining the differences in the mass-to-charge ratios (*m/z*) simultaneously[1, 7, 65, 103, 104]. Furthermore, use of tandem mass spectrometry (MS^n) to examine tissue surfaces enables identification of the visualized molecules and further provides detailed information on their structures[1, 39, 105, 106].

In this chapter, I used IMS to perform molecular imaging of ganglioside molecular species in mouse hippocampal formation. I clarified the distributions of different ganglioside molecular species, especially of those that contain different LCB moieties, namely C18- and C20-sphingosine. I have demonstrated, for the first time, that the distribution of ganglioside molecular species *in vivo* is brain-region selective. I

speculate that this selectivity is associated with the different functions of the gangliosides expressed in different brain regions.

2. Materials and Methods

Chemicals. Methanol, trifluoroacetic acid (TFA) and methyl iodide were purchased from Wako Chemical (Tokyo, Japan). Calibration standard peptide and 2,5-dihydroxybenzoic acid (DHB) were purchased from Bruker Daltonics (Leipzig, Germany).

Section Preparation. I used the brains of male C57BL/6Cr mice and at the indicated time point (0, 3, and 14 postnatal days, 8 postnatal weeks, and 33 postnatal months), they were sacrificed. The extirpated tissue blocks were immediately frozen in powdered dry ice and stored at –80°C until use. The frozen sections were sliced at –16°C with a cryostat (Leica CM 3050) at a thickness of 5 μm according to the previous reports [62, 107]. To fix each tissue block, an optimum cutting temperature (OCT) polymer was used. When the sections were sliced, the cutting block was not embedded in OCT since any residual polymer on the tissue slices might have degrade mass spectra[62]. Frozen sections were thaw-mounted on indium-tin-oxide (ITO)-coated glass slides (Bruker Daltonics) and ITO-coated sheets (Tobi Co., Ltd., Kyoto, Japan). ITO-coated glass slide was used for the measurement using TOF/TOF instrument and ITO-coated sheet was used for quadrupole ion trap (QIT)-TOF instrument. For matrix, I used a DHB solution (50 mg/mL; 70% methanol, 0.1% TFA) because this matrix minimizes the loss of sialic acid and carbon dioxide from gangliosides[108]. The matrix solution was uniformly sprayed over the tissue surface using a 0.2 mm nozzle caliber air-brush (Procon Boy FWA

Platinum; Mr. Hobby, Tokyo, Japan). In this study, the distance between the brush's nozzle tip and the tissue surface was kept at 15 cm and the spraying period was fixed at 3 minutes. All experiments with mice were conducted using protocols approved by the Animal Care and Use Committee of the Mitsubishi Kagaku Institute of Life Sciences.

Tandem Mass Spectrometry. For the MS^n analysis, I used a QIT-TOF mass spectrometer (AXIMA-QIT; Shimadzu, Kyoto, Japan). The MS^n analysis was performed directly on the hippocampus area of the mouse brain sections. Acquisition was performed in the "mid-mass range" mode (*m/z* 750 − 2000) at a stage voltage of −18 V in the negative-ion detection mode. In the MS^n analysis, the conditions for data acquisition (i.e., laser power, collision energy, and the number of laser irradiations) were changed in order to obtain product ion mass spectra with peaks that have high intensity and a high signal-to-noise ratio. The calibration was performed using an external calibration method.

Protocols of IMS. IMS were performed using a MALDI time-of-flight (TOF)/TOF-type instrument (Ultraflex 2 TOF/TOF; Bruker Daltonics). The data were acquired in the negative-reflectron mode under an accelerating potential of 20 kV by using an external calibration method. In this analysis, signals between *m/z* 800 to 2500 were collected. The raster scan on the tissue surface was performed automatically by FlexControl and Fleximaging 2.0 software (Bruker Daltonics). The number of laser irradiations was 100 shots in each spot. Image reconstruction was performed using FlexImaging 2.0 software.

Data processing. In the IMS results, the variation in the ionization efficiency, which is caused by the heterogeneous distribution of matrix crystals and their sublimation during measurement, was eliminated for each data point by equalizing the total ion current of each mass spectra, using the "Normalize Spectra" function of FlexImaging 2.0 software. In addition, in IMS of developing hippocampus formation (Figure 3-5), for each time point, intensity scale of C20-GD1 is normalized in order that the brightest pixels of C20-GD1 have 60% of the maximal C18-GD1 intensity value using the "Edit Mass Filter Parametrs" function of FlexImaging 2.0 software.

For calculation C20-ganglioside percentage (Figure 3-5), I used the most intense ion peak derived from GM1 and GD1, namely $[GM1-H]^-$ and $[GD1+K-2H]^-$, and intensities of these peaks in the summed spectra from each hippocampal region (at least 1300 spectra were summed for one region) were used for the calculation. For spectrum summation, Flex Analysis 3.0 software was used (Bruker Daltonics).

Analysis of Methyl-esterification of gangliosides. Tissues of the interested regions were dissected using an injection needle (Terumo 22G needle; Terumo Corporation, Tokyo, Japan) under stereo-microscopic observation and immediately immersed in 20 μl of methanol. After vortexing, the solution was centrifuged and the supernatants were added to 6 μl of methyl iodide. The reaction was performed for 3 h at room temperature. Gangliosides in the reaction mixture were eluted from a PepClean C18 spin column (Thermo Fisher Scientific, Kanagawa, Japan), according to the procedure described by S. Handa and K. Nakamura [109]. Mass spectrometry was performed with TOF/TOF instrument using DHB as matrix (5 mg/mL; 50% methanol, 0.1% TFA), on the steel target plate (MTP 384 target plate ground steel; Bruker Daltonics).

3. Results

Detection of gangliosides directly from mouse hippocampal formation

The negative-mode MALDI-MS spectra obtained directly from the mouse hippocampal formation are shown in Figure 3-2A. Negatively charged glycerophospholipids, such as phosphatidyl inositol, phosphatidyl ethanolamine, and phosphatidyl serine, and sphingolipids such as sulfatides (STs) were detected in the mass range of $800 < m/z < 950$. Mass peaks corresponding to GM1, GD1, and GT1 gangliosides were detected in the mass range of $1500 < m/z < 2300$. As shown in Table 3-1, I detected ions corresponding to GM1, GD1, and GT1, which contain either C18- or C20-sphingosine.

Structural analysis by MS^n allows us to analyze more detailed structure of detected ions. To confirm that the differences of 28-u which corresponds to a $(CH_2)_2$ unit, observed between the C18 and C20 species, can be certainly attributed to the LCB chain lengths, I performed a structural analysis of ions corresponding to GM1 gangliosides by MS^n (Figure 3-2B). MS^n can provide detailed structural information of the ions of interest. The MS^2 results for both m/z 1544 and 1572 showed a ceramide peak and peaks corresponding to oligosaccharides containing a sialic acid (Figure 3-2B (a)). The peaks in the MS^2 spectra for oligosaccharides of m/z 1544 and 1572 were exactly the same; thus, these gangliosides have the same oligosaccharide moiety. I therefore performed MS^3 of the ceramide peak to determine the detailed structure of the ceramide. In the MS^3 spectra obtained, the common peak was observed at m/z 283.0, which corresponded to $(C_{17}H_{35}COOH)^-$, a fatty acid (Figure 3-2B (b)). Thus, I determined that the mass difference was derived from the difference in the chain lengths of the LCB, namely C18- and C20-sphingosine.

IMS of gangliosides in the mouse hippocampal formation.

MALDI-IMS visualizes the spatial abundance of numerous ions simultaneously in the same tissue section, thus enabling holistic imaging of ganglioside molecular species. Figure 3-3 shows the imaging results obtained for the mouse sagittal brain section at low instrumental step size (50 μm raster). For imaging the myelinated region of the brain section, I visualized the ions at *m/z* 878.6 and 906.6, which correspond to STs with different sphingosine bases, namely ST(22:0 OH) and ST(24:0 OH), respectively (Figure 3-3 b-c). STs demonstrate the same distribution pattern regardless of the type of ceramide moiety; however, interestingly, the distributions of C18- and C20-ganglioside molecular species are considerably different. In particular, IMS revealed a characteristic concentration of ions corresponding to C20 species of both GM1 and GD1 in a part of the hippocampal formation (Figure 3-3A, arrowheads). On the other hand, ions corresponding to C18-GD-1 were distributed uniformly in the gray matter region of the frontal brain, and those corresponding to C18-GM1 were strongly distributed in the white matter region in addition to the gray matter region (Figure 3-3A).

To understand the characteristic localization of the C20-species in the hippocampal formation in greater detail, I performed IMS of the hippocampal formation at high instrumental step size (15 μm raster) (Figure 3-3B). Ions corresponding to the C20-species of both GM1 and GD1 were found to be localized in the outer two-thirds of the dentate gyrus (DG) molecular layer (ML) and the stratum lacunosum moleculare (SLM) of both CA1 and CA3. They were, however, much less observed in the inner layer of molecular layer of DG and the layers outside of SLM in the CAs. In contrast, ions corresponding to C18-GD1 were detected in the whole region of the hippocampal formation, but the signals were weak in the DG-ML and the SLM. Ions corresponding

to C18-GM1 were also detected in region rich in the myelinated axon. I also performed IMS of a horizontal brain section (Supplemental Figure S6) (40 μm raster) and observed clear accumulation of C-20 gangliosides in the entorhinal cortex (EC) and the regions including projections from the EC both to the DG-ML and to the SLM of the hippocampus.

Validation of IMS results by MS of methyl-esterified gangliosides.

MALDI-MS of sialic acid-containing oligosaccharides should be performed with caution because of the preferential loss of sialic acid during mass spectrometry[108, 110]. To evaluate the degree of sialic acid loss in the experimental system used, I performed mass spectrometry of authentic samples of GM1, GD1, and GT1 in the presence of sodium and potassium at physiological concentrations, at same laser power and detector sensitivity used in the IMS experiments (Supplemental Figure S7). I found that GD1 and GT1 preferentially formed sodium/potassium adduct ions under presence of salts, and that reduced the sialic-acid dissociation though GD1 produced certain amount of ions at *m/z* 1544 and 1572, which lost one sialic-acid. On the other hand, the presence of salts efficiently suppressed the loss of sialic acid from GT1. In authentic GM1 samples, there was almost no sialic-acid dissociation.

Thus, to confirm the IMS results, I extracted gangliosides from the regions of interest, i.e., the stratum radiatum (SR) (region A) and ML/SLM region (region B) in the mouse hippocampal formation (Figure 3-4). Then I derivatized them to the methyl-esterified gangliosides. While underivatized GD1 and GT1 exhibited significant loss of sialic acid due to dissociation by in-source or post-source decay[108, 110, 111], such dissociation was suppressed by methyl esterification[112], enabling the detection of their fully sialylated

molecules as dominant peaks. The results of MALDI-MS analysis of methyl-esterified GM1 and GD1 showed that the C20 molecular species was present in approximately 21% of the total GM1 gangliosides in region A and 32% of those in region B. Further, 21% and 34% of the GD1 gangliosides in region A and B, respectively, contained the C20 molecular species. Taken together, these results confirmed the accumulation of the C20 species in both GD1 and GM1 gangliosides in the ML and SLM.

Changes in the distribution of ganglioside molecular species during development.

To date, several articles have reported development- and aging-related increase in the C20-ganglioside content [98-100], and I think that it is important to know both when and where C20-gangliosides accumulate. In order to identify and characterize gangliosides in developing and aged hippocampal formations, I performed IMS of the mouse hippocampal formation at 0, 3, and 14 postnatal days, 8 postnatal weeks, and 33 postnatal months. Figure 3-5 shows the IMS results for ions at m/z 1858 and 1902 and demonstrates that the area with high C20-GD1 content increased with neurodevelopment. On postnatal days 0 and 3, significant signals (S/N > 1.0) derived from C20-GD1 were detected from only a few data points in the entire hippocampal formation. On postnatal day 14, C20-GD1 signals were concentrated in the narrow area of the DG-ML and began to be observed over the medial edge of the region, which corresponds to the terminal area of the projections from the lateral entorhinal area (Figure 5A, arrow heads) [113]. At 8 postnatal months, the signals were observed from a wide area (ML/SLM), which corresponds to the terminal area of the projections both from the lateral and medial entorhinal area [113]. Furthermore, in aged hippocampal formations, the accumulation was clearly increased. Figure 3-5B shows the percentage

of GD1 gangliosides containing the C20-species in the different regions. It demonstrates the development- and aging-related increase in C20-GD1 content in the ML and SLM, but no obvious increase in other regions in the hippocampal formation. In contrast, the C18-GD1 content decreased in the ML/SLM with aging (Figure 3-5A, arrows).

4. Discussion

As a next step of the previous study which characterized the distinct composition of ganglioside molecular species between axons/dendrites and soma of neuron *in vitro* [114], in the present study, I demonstrated that gangliosides with differences in their ceramide moieties showed distinct distribution patterns in the mouse brain, especially in the hippocampal formation *in vivo*.

In the direct analysis of gangliosides using MALDI-MS, the mass spectra showed distinct mass peaks for ganglioside molecular species with different oligosaccharide/ceramide moieties (Figure 3-2), which enabled the visualization of the distribution of individual molecular species by IMS (Figure 3-3). The characteristic of gangliosides specific to the CNS is the structure of their LCB, i.e., the presence of 18 or 20 carbons; further, C20-gangliosides are found only in the CNS [95-97]. Antibodies to the oligosaccharide moieties of gangliosides are used to visualize the distribution of gangliosides with different oligosaccharide moieties; however, antibodies cannot distinguish between the C18 and C20 molecular species. To date, no other method has achieved differential visualization of such molecular species.

MALDI-MS should be performed with caution when used for the detection of oligosaccharide moieties of gangliosides because previous MS studies of gangliosides have demonstrated that sialic acid residues tend to be lost [108, 110, 111]. Thus, it is necessary

to evaluate the degree of sialic acid dissociation in the experimental system described here. I performed MS of authentic samples of GM1, GD1, and GT1 gangliosides, which account for 80% of the total brain gangliosides[89]. From the results, I deduced that the ion signals at m/z 1544 and 1572 correspond to ions originating from both GM1 and GD1, but not GT1. In contrast, the ions at m/z 1874 and 1902 contain almost no GT1-derived signals and originated predominantly from only GD1(Supplemental Figure S7).

Based on these results, I analyzed the distribution patterns of the C20 species. The IMS results revealed that both C20-GM1 and C20-GD1 are selectively localized in the outer two-thirds of the DG-ML, among all brain regions (Figure 3B). The ion signal at m/z 1572 (C20-GM1/GD1) showed more concentrated pattern than that at m/z 1902(C20-GD1); this indicates that GM1 has a higher C20 content than GD1 in these regions. Moreover, this trend was confirmed by MS of methyl-esterified gangliosides after extraction from the tissue section (Figure 3-4)

Because most of the afferent nerves from the EC terminate in the SLM/ML in DG, C20-GM1 and GD1 are suggested to be most concentrated in the axon and the axon terminals of the neurons from the EC[113]. Furthermore, in the horizontal sections, C20-GM1/GD1 were localized in the lateral and medial parts of the EC area and the region including the projections (a medial and lateral perforant path) to the DG and the area in which they terminated[115]. These results suggest that EC neurons selectively express the C20 species. I deduce that for other gangliosides, in particular precursor-gangliosides to biosyntheses GM1 and GD1, namely GM2, GD2, GM3, and GD3, the C20-species of them are also localized in these regions. Although I could not detect a sufficient number of ions of these gangliosides, presumably because they are

present in considerably smaller amounts than GM1 and GD1[89], this is an interesting topic for further study.

Moreover, observation of the concentration of C20 species throughout development suggests that the appearance of extensive C20-GM1/GD1 distribution in the DG-SMm corresponds to the period of rapid synapse formation, dendritic outgrowth, and glial proliferation in this region. Taken together, this C20-GM1/GD1 distribution and concentration may reflect the functional maturation of the EC-hippocampus neural pathway, which possibly progresses first from the LEA and then from the MEA area (Figure 3-5). Indeed, it is known that EC lesions induce changes in the ganglioside content in the hippocampus DG-ML[116].   Moreover, it is known that animals with EC lesions show behavioral deficits, and ganglioside administration accelerates the recovery of the impaired functions[115, 117, 118]. The present findings suggest that such ganglioside treatments have effects that are possibly dependent on the type of molecular species they contain. Furthermore, the IMS results suggest that aging-related increase in the C20-GM1/GD1 content, which has also been proven by the biochemical data obtained in studies using HPLC[94, 99, 100, 119], selectively occurred in the DG-ML/SLM region in the hippocampal formation. Since C20-sphingosine is more effective in reducing membrane fluidity than the C18 species, this age-dependent accumulation of C20-GM1 can lead to altered properties of the cell membrane. Considering the age-dependent accumulation and the selective distribution of the C20 species in the EC and its projections, where selective degradation of neurons is observed in early stages of Alzheimer diseases[120], this accumulation may increase the risk for the age-dependent neurological diseases such as Alzheimer disease.

Finally, in this study, I successfully characterized the location of age-dependent

C20-GD1 accumulation (Figure 3-5) besides that previous studies have established this phenomenon with highly quantitative methods in brain lysate[121]. However, one should bear mind that IMS is developing method especially for quantitative analysis because of nature of MALDI, in which ionization efficiency of analyte is easily affected by number of factors such as crystallization condition of matrix and extraction efficiency of analyte from tissues [122]. I consider that established-quantitative methods such as HPLC are effective to complement its quantitative aspect of MALDI-IMS.

Figures and Tables for Chapter 3.

a.

b.

C18-species

C20-species
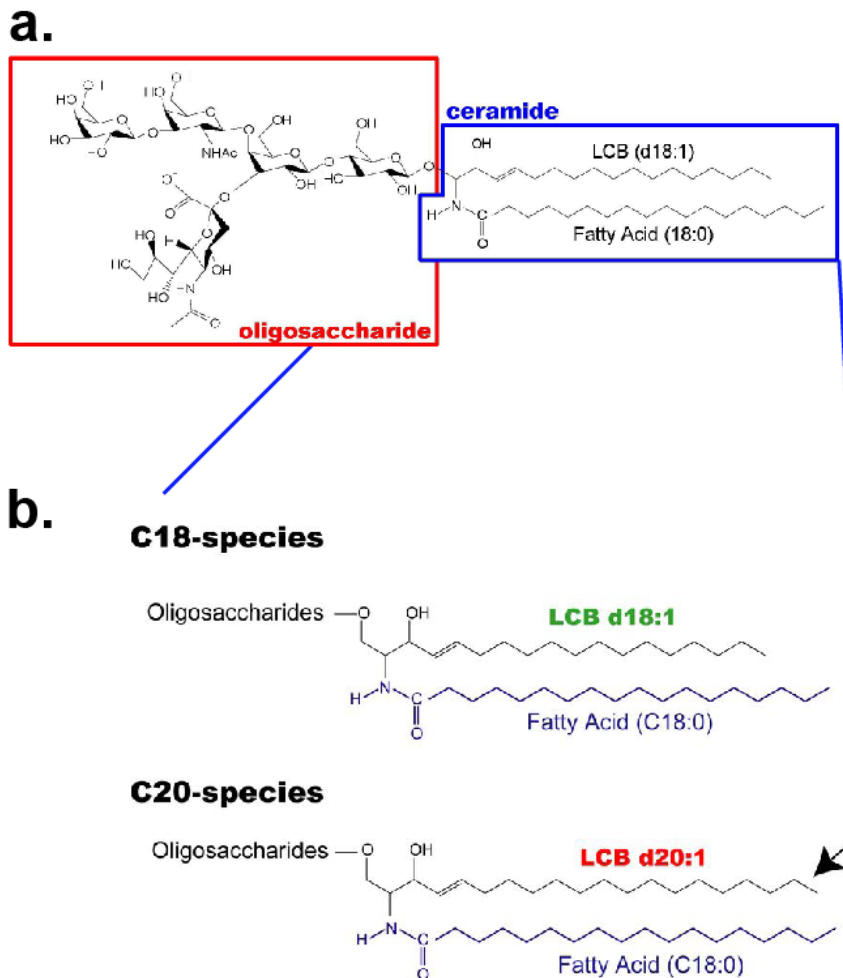
**Figure 3-1: Structure of GM1a.**

Gangliosides comprise a large family; their oligosaccharides structures differ in the glycosidic linkage position, sugar configuration, and the contents of neutral sugars and sialic- acid content. The ceramide moiety of gangliosides, it also has some variation varies with respect to the type of long -chain base (LCB) (sphingosine- base) and fatty acid moiety (a). Structures of ganglioside molecular species containing C18- and C20-long chain base (LCB) are shown in (b).
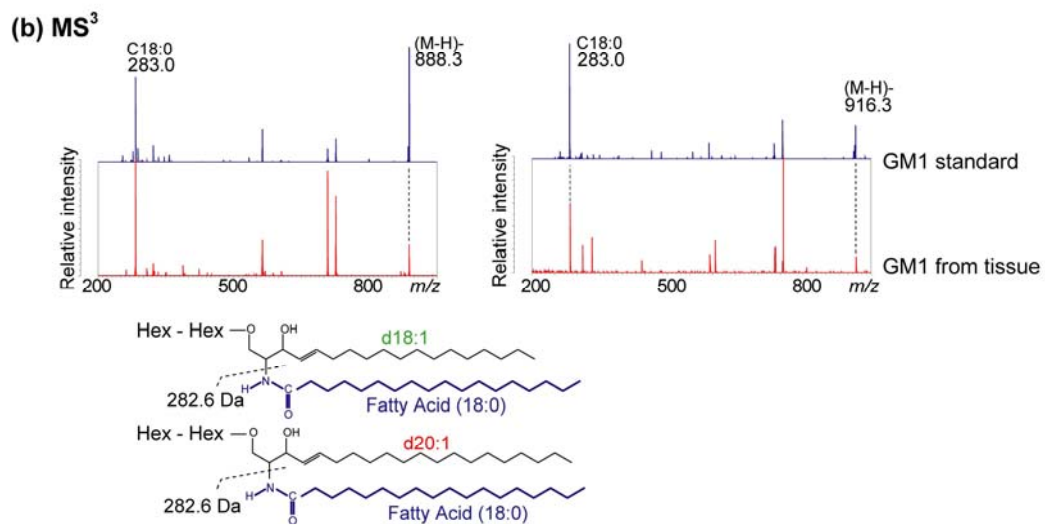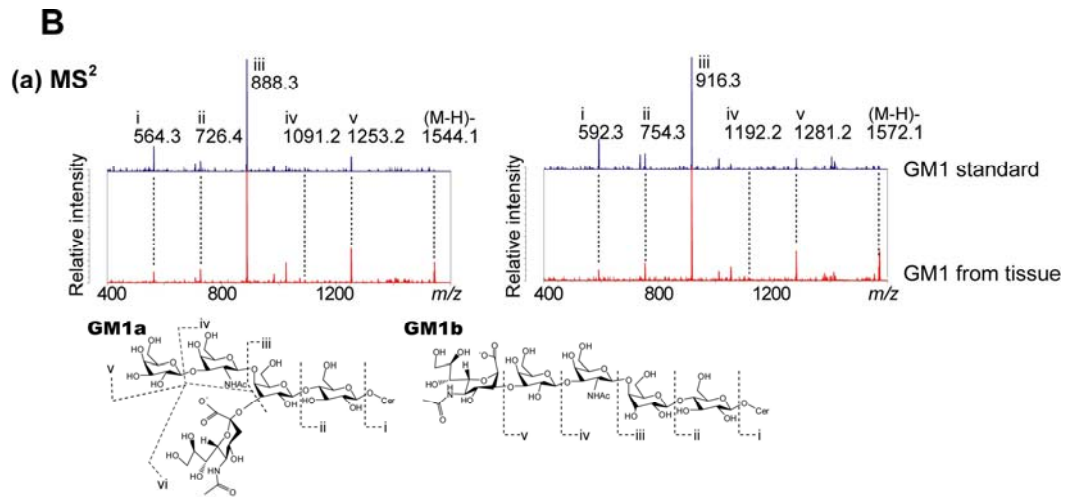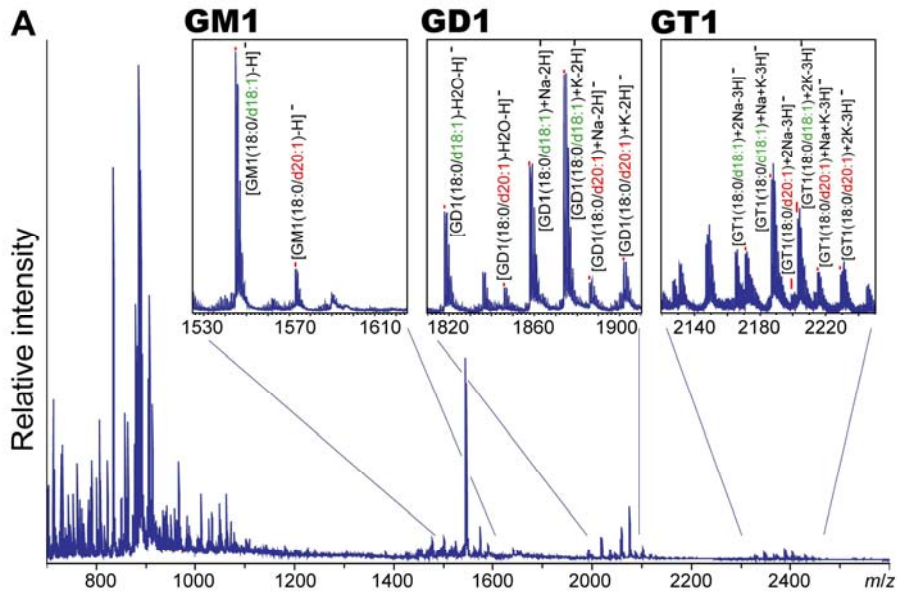
Figure 3-2: Direct MALDI-MS and MS^n allows specific detection of ganglioside molecular species.

A. Averaged mass spectra obtained from the entire hippocampal formation. In the spectra, the mass peaks corresponding to GM1, GD1, and GT1 are detected, and IMS provides distinct signals for molecular species containing C18- and C20-sphingosines.

B. MS^n structural analysis of ions corresponding to GM1. (a) MS^2 product ion spectra show that the ions at m/z 1544 and 1572 had the same oligosaccharide structure, i.e., they contained a sialic acid moiety, but the ceramide mass peaks were observed at different m/z values. (b) MS^3 product ion mass spectra of m/z 888.3 and 916.3 were obtained to determine the different structural constituents in the ceramide moieties. Because of the detection of m/z 283.0 (fatty acid-related ion) in both the spectra, the 28-u difference between m/z 1544 and m/z 1572 was attributed to the difference in the sphingosine constituent; m/z 1544 had C18-sphingosine and m/z 1572 had C20-sphingosine.
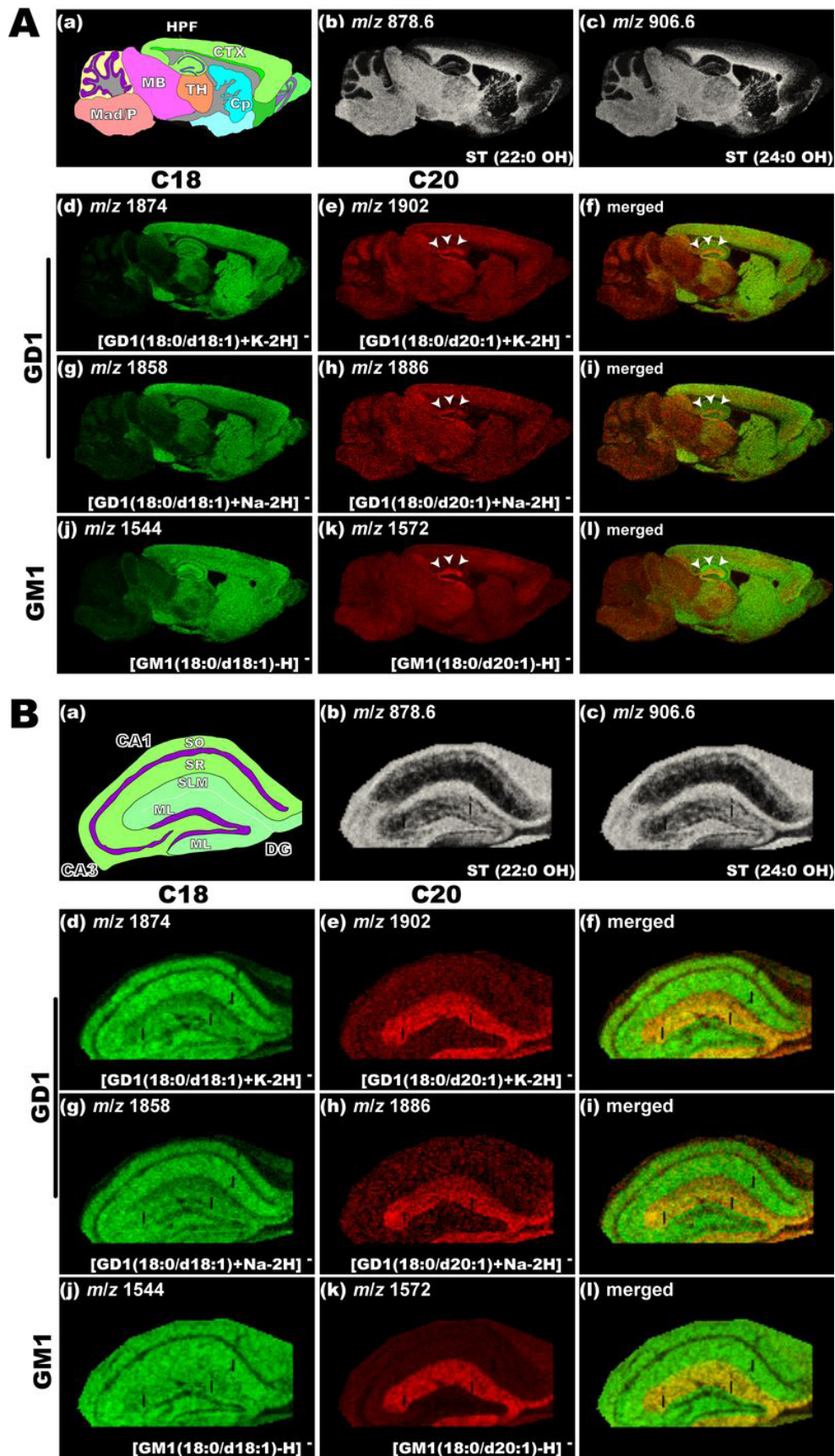
Figure 3-3: Localization of C20-sphingosine-containing gangliosides in the hippocampal formation.
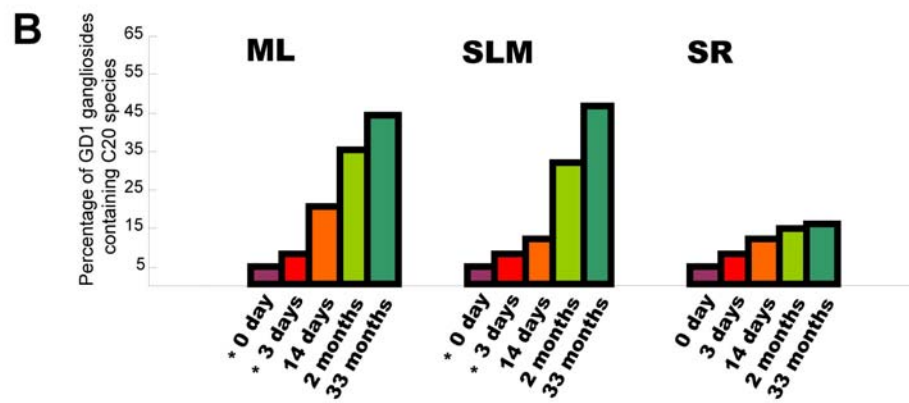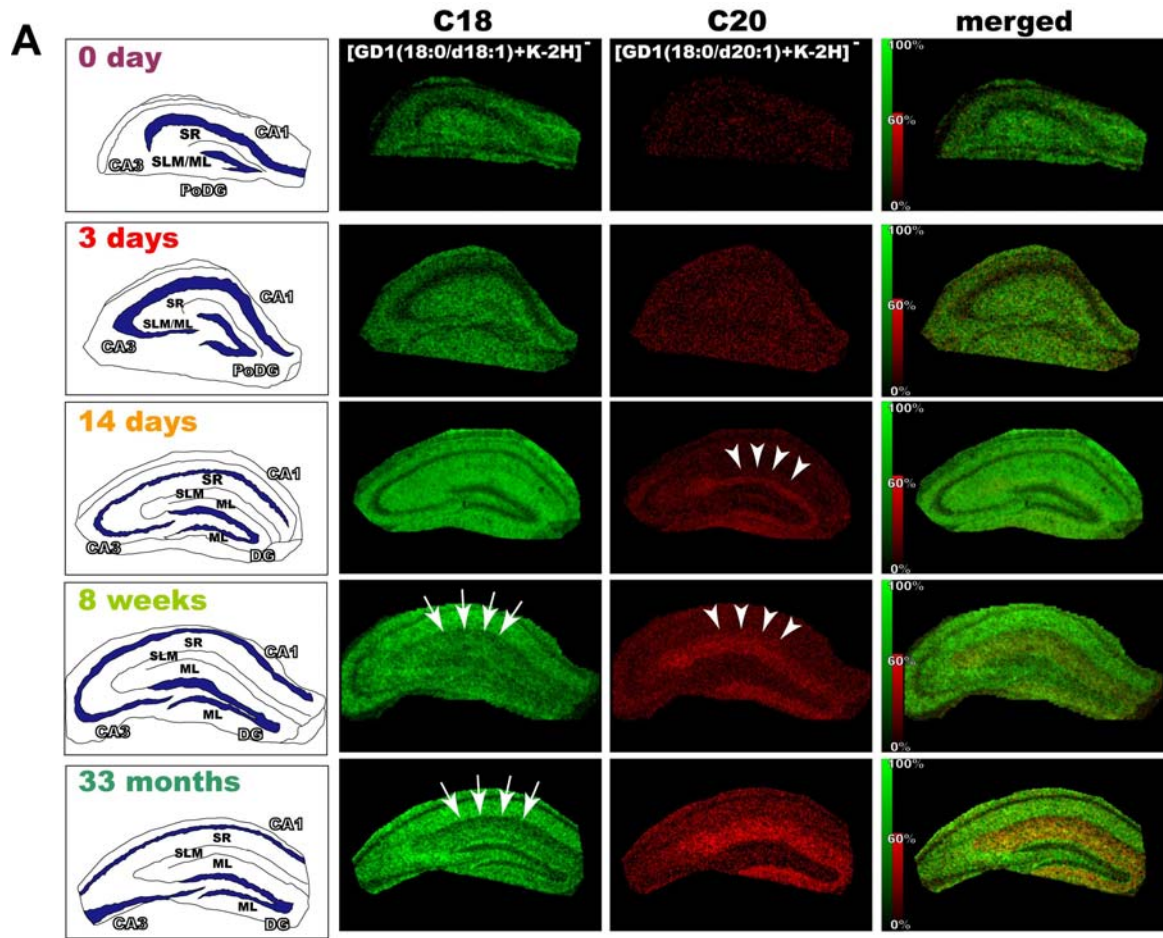
IMS at 50 μm raster step size was used to gain an overview of ganglioside distribution in different brain regions (A), and IMS at 15 μm raster size was used to study in detail the distribution pattern of gangliosides in the hippocampus (B). In both panels, schematic diagram of the brain section (a) and ion images of STs (b-c) are presented. For ions corresponding to the GD1 molecular species, I observed the ion distributions of both sodium and potassium complexes, i.e., the ions at m/z 1858 (f) and m/z 1886 (g), which correspond to the [M+Na-H]$^-$ form of C18- and C20-GD1, and those at m/z 1874 (h) and m/z 1902 (i), which correspond to the [M+K-H]$^-$ form of C18- and C20-GD1, respectively. The ion distribution patterns corresponding to the GD1-Na salts and GD1-K salts are fairly uniform for both C18- and C20- species. For GM1, m/z 1544 (d) and m/z 1572 (e), which correspond to C18- and C20-sphingosines containing GM1 respectively are shown.
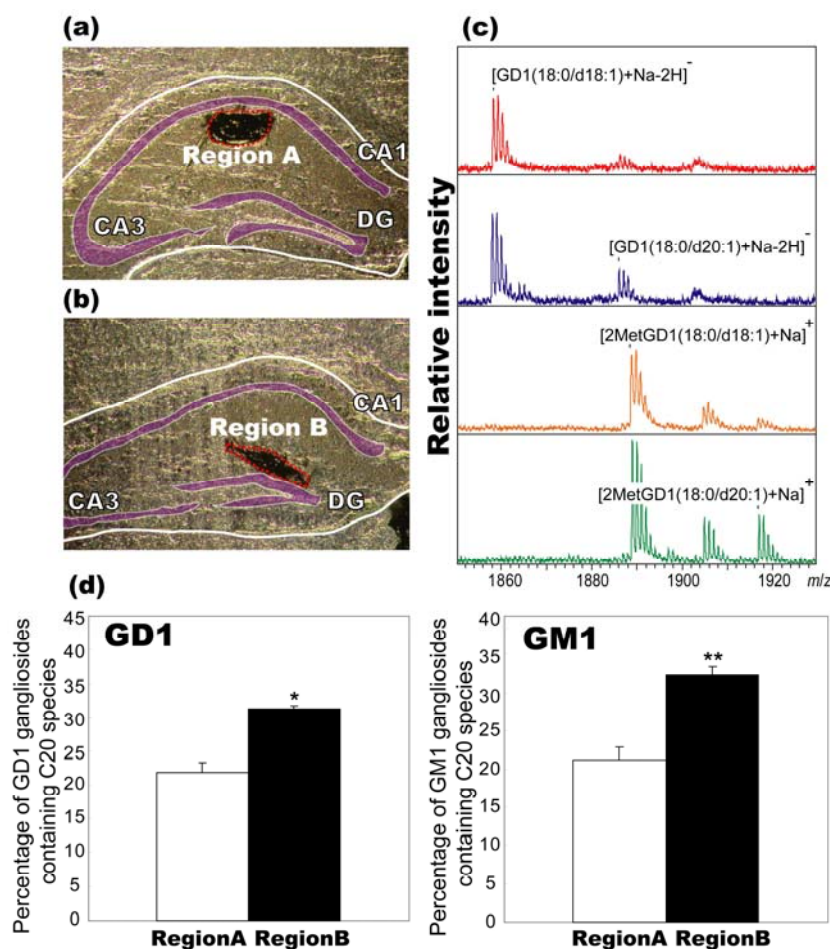
Figure 3-4: Localization of C20-sphingosine-containing gangliosides was confirmed by MS of extracted and methyl-esterified gangliosides.

To determine the percentage of GM1/GD1 gangliosides containing the C20-species in different regions without allowing sialic acid dissociation during MS measurement, I extracted gangliosides from the dendritic region of the SR (region A, (a)) and the ML/SLM (region B, (b)). They were derivatized to methyl-esterified gangliosides. From the result of MS of underivatized gangliosides and methyl-esterified gangliosides (c), the percentage of GM1/GD1 gangliosides containing the C20-species were calculated (d). Three different mouse brain sections were used, and the data were expressed as mean ± S.D. * and ** indicate $P < 0.05$ and $P < 0.005$, respectively, Student's *t*-test.

A

	C18	C20	merged
0 day	[GD1(18:0/d18:1)+K-2H]⁻	[GD1(18:0/d20:1)+K-2H]⁻	

B

Percentage of GD1 gangliosides containing C20 species

ML   SLM   SR

Figure 3-5: Development- and aging-related accumulation of C20-GD1 in the ML and SLM of the hippocampal formation.

I visualized the ion corresponding to GD1 (m/z 1874 and 1902) in the mouse hippocampus at the indicated time points (P0, P3, P14, 1 month, and 33 months). For each time point, intensity scale of C20-GD1 is normalized in order that the brightest pixels of C20-GD1 have 60% of the maximal C18-GD1 intensity value. In the P14 mouse hippocampus, C20-GD1 was concentrated in the narrow area of DG-SMm and began to spread over the medial edge of the region (arrow heads). In contrast, the concentration of the C-18 species decreased in the ML/SLM with aging (arrows). Quantification result of C20-GD1 on the total GD1 signal in the ML, SLM and SR region has also been shown (B). *; At P0 and P3, I could not distinguish between the ML and SLM area; therefore, values obtained from the region corresponding to ML/SLM have been used for both the regions in the graph.

Chapter 4. MALDI-IMS with statistical analyses revealed abnormal distribution of metabolites in colon cancer liver metastasis

1. Introduction

In this chapter, a medical application of MALDI-IMS to colon cancer liver metastasis is described. The goal of this study is to discover potential biomarkers which are specifically found in normal or diseased cells. The IMS capability to simultaneously detect multiple metabolites at a time, even with spatial information, facilitates this emerging technique as an effective tool for biomarker discovery, within surgically resected tissues. In fact, previous study has shown that IMS can discriminate cancer types (such as primary or non-primary cancer) based on their molecular signature, and even predict survival rate among human patients[56]. For this kind of purpose, it is necessary to utilize statistical analyses to extract useful information from enormous IMS data-sets. The MS of tissues gives an extremely complex spectrum with hundreds to a thousand of peaks obtained from a single data point, and furthermore, several thousands of spectra with spatial data are obtained at one IMS measurement. Because of the complexity and enormousness of the IMS dataset, for discovery of biomarkers, manual processing of the dataset in order to obtain significant information is not a realistic procedure. In this regard, today, multivariate analysis becomes a powerful tool in IMS data analysis. Here, I applied the statistical procedure to the IMS results of the pathological specimen, colon cancer liver metastasis.

Colon cancer is a challenging worldwide clinical problem and the incidence rate of colon cancer has been rising rapidly in Japan [123]. Genealogy is known to be a risk factor [124] and as environmental factors, aging [125] and diet, particularly a high intake of animal

67

protein and fat along with a low intake of fiber [126] increase the incidence of colorectal cancer. Until today, a number of approaches including a cDNA microarray have revealed characteristics of cancer cells with some success, such as discover of specific gene expressions for drug resistance [127]. In addition to this, IMS approaches presented here which enable comprehensive analysis of metabolite expression patterns in tissues might improve our ability to understand the molecular complexities of tumor cells.

In this chapter, I will show altered composition of metabolites in the cancerous tissue revealed by IMS, with both manual data processing and statistical data management. In particular, as a statistical strategy, an unsupervised multivariate data analysis technique that enables us to sort the data sets without any reference information is described. A major method that is related to IMS, namely, principal component analysis (PCA) will be described in detail.

2. Materials and Methods

Chemicals. Trifluoroacetic acid (TFA) was purchased from Merck (Darmstadt, Germany). Methanol was purchased from Wako Pure Chemical Industries (Osaka, Japan). 2, 6-dihydroxy acetophenone (2, 6-DHA) was purchased from Bruker Daltonics (Leipzig, Germany). A calibration standard for the low *m/z* region was prepared by mixing angiotensin III ($[M+H]^+$: 899.47) and Leu-Euk ($[M+H]^+$: 556.28). All the chemicals used in this study were of the highest purity available.

Conductive sheet. The conductive sheet was purchased from Tobi Co., Ltd. (Osaka, Japan). This sheet has a thin indium-tin-oxide (ITO) layer on a polyethylene

terephthalate. The sheet was 125 μm thick and its conductivity was 100 Ω. The transparency was 80% (λ = 550 nm), so that I could observe stained tissues with transmitted light. This flexible sheet made sample handling easy, because the sheet could be cut to an arbitrary size with a paper cutter and samples did not crack easily, which was sometimes problematic with glass slides.

Tissue block preparation. A tissue block with colon cancer liver metastasis was removed from a Japanese patient during an operation, and rinsed with PBS buffer. The tissue was then immediately frozen in liquid nitrogen to minimize degradation, and was kept at -80°C. Informed consent was obtained before the operation.

Sample preparation. Before sectioning, the liver block was left for 30 min at -20°C. The tissue sections were sliced to a thickness of 3 μm using a cryostat (CM 3050; Leica, Wetzler, Germany) and mounted onto the ITO sheet. A thin matrix layer was applied to the surface by an airbrush. A two-minute spraying of 2, 6-DHA solution (30 mg/ml in 70%methanol/0.1%TFA) was iterated twice. During spraying, the distance between the nozzle and the tissue surface was kept at 15 cm. After drying, the ITO sheet was attached to a metal-coated glass slide by conductive tape to facilitate electrical conduction.

Conditions of mass spectrometry and MALDI-IMS. The tissue section was analyzed using a MALDI-TOF/TOF-type instrument, Ultraflex II TOF/TOF (Bruker Daltonics, Leipzig, Germany), which was equipped with a Nd:YAG laser with a 200 Hz repetition rate. External calibration solution was deposited on the surface of the ITO sheet to

minimize mass shift. In this experiment, an acceleration voltage set to 25 kV.

Imaging mass spectrometry. A raster scan on the tissue surface was performed automatically. Laser irradiation consisted of 100 shots in each spot. The interval of data points was 100 μm, giving a total of 445 data points in the tissue section. The spectra shown in the Results section were accumulated in square sections (300 μm x 300 μm) of normal and cancerous areas. Here, I did not apply data processing such as smoothing or baseline subtraction. The reconstructions from the spectra were performed by FlexImaging (Bruker Daltonics).

Statistical Analysis. Statistical analyses were carried out using the ClinProTools 2.2 Software. For the statistical analyses, the mass spectra were internally recalibrated on common peaks (also known as spectral alignment) and normalized on the total ion current. An average spectrum created from all single spectra was used for a peak picking and to define integration ranges. These integration ranges were used to obtain the intensities or areas on the single spectra. The signal intensities were used for all calculations.

3. Results and discussion

Comparison of averaged mass spectra in normal and cancerous areas

At first, a tissue section with colon cancer liver metastasis was stained with HE for histological observation (Figure 4-1 (a)). The histochemical staining enables to distinguish the normal, stroma, and cancer cells which were localized on the left, middle, and right location of the tissue section, respectively. A successive tissue section was

70

used for MALDI-IMS and after the measurement, according to the histological

observation, two quadrate areas—one from the normal area and the other from the

cancerous area—were selected to collect and average the obtained mass spectra (Figure

4-1(b)).

Figure 4-2 shows the averaged mass spectra from the cancerous (Figure 4-2a) and

normal area (Figure 4-2b). Numerous differences on the mass signals were observed

between the normal and cancerous cells. In particular, I found that the signal at *m/z* 725

showed a massive increase in the cancerous region while ion at *m/z* 616 was almost

disappeared in the cancer cells.

Visualization of molecules specifically localized in normal and cancerous region.

Having demonstrated the cancerous/normal tissue specific localization of ions at *m/z*

616 and 725, respectively, I proceed to the visualization of their distribution pattern. As

expected, the ion distribution images shown in Figure 4-3 demonstrate that they are

expressed in the normal/diseased region specific manner; ion at *m/z* 725 was clearly

localized in the cancerous region while ion at *m/z* 616 was found only in the normal cell

region. The merged image demonstrates that these two ions were complementary

distributed in the specimen.

Molecular identification with tandem MS.

Next question is the origin of these two ions. As shown in previous chapters, tandem

MS provides the structural information of interest ions and therefore, it enables the

molecular identification. The result of tandem MS with regard to *m/z* 725 is shown in

Figure 4-4A. In the product ion mass spectrum, peak at *m/z* 666.5 and 542.5 which are

71

corresponded to neutral loss (NL) of trimethylamine (59 u, C_3H_9N) and NL of trimethylamine and cyclophosphate (124 u, $C_2H_5O_4P$), respectively, were detected. This result indicates that *m/z* 725 contained an alkali metal adduct phosphocholine, therefore ion at *m/z* 725 is suggested to be PC or sphingomyelin (SM) [128]. According to the nitrogen rule, ion at *m/z* 725 having odd nominal mass should contain additional nitrogen in its structure, thus indicating presence of a sphingosine. I concluded that *m/z* 725 was attributed to be a sodiated molecule of SM(16:0).

Regarding the ion at *m/z* 616, the first generation product ion mass spectrum from *m/z* 616 showed consecutive neutral losses of 73, 59, and 45 Da (Figure 4-4B(a)). From the previous leterature[129, 130], it is suggested that *m/z* 616 corresponded to heme B and that these neutral losses were derived from loss of CH2CH2COOH (73 Da), CH2COOH (59 Da), or COOH (45 Da) group, respectively. The molecular structure of heme B is displayed as an inset. Figure 4-4B(b) shows the second product ion mass spectrum generated from *m/z* 557, and an additional NL of 59 Da was observed. This fragment was considered to be derived from another CH2COOH in heme B.

Here, I demonstrate that SM(16:0) was strongly expressed in the cancerous area. Previous studies reported that in the colon cancer, the cancerous cells contain elevated amounts of total phospholipids [131], and in addition, the phospholipid composition of the cellular membrane is altered [131, 132] even between cancer cell types, i.e., metastases and non-metastatic cancer [132]. Brasitus et al. studied a relationship between the malignancy and altered lipid composition of the colon cancer, and reported significant accumulation of SM, in consistent with presented result [133]. On the other hand, heme B consists of an iron atom and porphyrin, and is known as a prosthetic group in hemoglobin, which is a protein in erythrocytes. Presented results indicate the difference between the blood rich

organ liver and the ischemic metastatic colon cancer[134, 135].

IMS linked to multivariate analysis.

Until here, I showed that two small metabolites were specifically expressed between the cancerous and normal tissue areas. In the described data analysis procedures without statistical methods, I usually averaged the spectra of each region and visually compared the mass peaks between the spectra one by one. As seen in Figure 4-2, with such visual comparisons of spectra, I was certainly able to find differences among the peak expressions. However, such methodology is inefficient especially when one is analyzing a large number of mass peaks and/or many tissue samples.

Below, I will describe the IMS-linked PCA, to compare the metabolite composition of the normal/cancerous regions. Here, I will not describe the detailed mathematical theory due to the space limitation, but in brief, PCA is a statistical method that merges the data containing multiple elements into low-dimensional data. It reduces a large set of variables to a small set of variables called "principal components" which are linear combinations of the original variables. In the PCA coupled IMS data analysis, spectra obtained by IMS are processed to peak-detection and based on the generated peak list, PCA decomposition was performed. PCA images (i.e., 2D intensity map of principle component score on the tissue section) were often utilized to find differences of molecular composition among regions/tissues.

PCA calculation results in several parameters and below, the "*component score*" and "*factor loading*" are particularly important for interpretation of results. A component score is calculated for each mass spectrum; all are defined for each principal component (e.g. for PC1, PC2....). Those component scores are often plotted two-dimensionally, to facilitate interpretation of the PCA results. In Figure 4-5 and 3-6, component scores for

each principle component are plotted on the x-axis and y-axis, and each dot in the graph represents a spectrum from a distinct data point on the tissue section. What is important to note is whether two (or several) populations of spectra (= dot) obtained from distinct regions, e.g., normal vs. diseased, are spatially separated on the graph, or not. If they are separated (Figure 4-5a), it means that the molecular expression patterns of these two regions were statistically distinct from each other. If not, PCA failed to extract the statistical differences between the populations (Figure 4-5b).

Figure 4-6 shows result of IMS-PCA for the colon cancer tissue. In this case, this unsupervised analysis revealed that the largest spectral difference (i.e. the largest difference in metabolite composition) was observed between the normal and the other tissue areas (i.e., normal vs. stroma/cancer area), and second large difference was observed between the stroma and normal/caner area. The overall interpretation of PCA was shown in table 4-1.

In the graphs shown in Figure 4-6(b), the colored circles indicate mass spectra obtained from the normal, stroma and cancerous regions (colored in red, green and blue, respectively). Notably, the 3 populations are spatially-separated by the component scores for PC2 and PC3, but not PC1. This indicates that PC2 and PC3 particularly contain the statistical differences among these three regions.

In detail, along with the PC2 scores (x-axis), the spectra from normal and the others are clearly separated. The PC2 image also demonstrates a large difference of PC2 score value between normal vs. the other regions (Figure 4-6(c)). On the other hand, along with the PC3 scores (y-axis), spectra from stroma and the other regions are separated and the PC3 image also shows much higher PC3 score value of stroma region than the other regions (Figure 4-6(c)).

74

Analysis of loading factor for each principle component facilitates identification of "responsible" molecules which differentiate control and diseased samples.

As a next step, an analysis of factor loading plot would identify peaks that were differentially expressed between regions. Since a component score defined for each spectrum is a sum of the value of the factor loading value, multiplied by peak intensity, therefore, when numbers (= m) of mass peaks were used in the analysis, the component score will be:,

$$ScorePC1(x, y) = \sum_{n=1}^{m} load(n) \times Int.(n)$$

$ScorePC1(x, y)$: component score against PC1, obtained from (x, y)

$load(n)$: factor loading value against a mass peak for n

$Int.(n)$: mass peak intensity for n

m: number of mass peaks used for calculation

According to this equation, in the spectra from the normal tissue region, the mass peak with large negative value regarding PC2-factor loading, is supposed to be intense. On the other hand, it was also indicated that peaks with large positive value for PC2-factor loading would be specific molecules to the stroma/cancerous regions. In other words, such mass peaks with a radical absolute value for PC2-factor loading are suggested to be major contributors to differentiate these regions.

PC2 represents difference of metabolite composition between normal vs. other region.

In Figure 4-7, the factor loading values for PC1 and PC2 are plotted on the x-axis and y-axis, respectively. Each dot indicates a distinct mass peak. Such a graph makes it very easy to find the peaks with the intended factor loading value against each PC. Since

peaks that have negative loading values regarding PC2 are supposed to be specifically expressed by the normal liver cells, thus I picked up a mass peaks with large negative loading value for PC2, and obtained their distribution image. As results, I found that ion at *m/z* 616.2, which is already demonstrated as a normal region specific molecule, was statistically classified into "*normal region specific*" category (Figure 4-7, lower part). Furthermore, by this procedure, other mass peaks corresponding to sodiated and potassiated molecules of PC(diacyl-16:0/22:6) were identified as the normal cell specific metabolites (Figure 4-7, lower part). On the other hand, through the same procedure, I also successfully identified the molecules which localized in the cancerous/stroma region (Figure 4-7, upper part).

PC3 represents difference of metabolite composition between stroma vs. other region.

In Figure 4-8, the factor loading values for PC1 and PC3 are plotted on the x-axis and y-axis, respectively. In this case, since mass peaks that have a large positive loading value regarding PC3 are supposed to be specific molecule to the stroma region, therefore I picked up mass peak at *m/z* 722.0 and obtained a distribution image (Figure 4-8, upper part). As a result, I identified *m/z* 722.0 as stroma specific molecule, and on the other hand, with same procedure, I revealed that ions at *m/z* 760.4 and 766.4 were almost disappeared in the stroma region.


4. Conclusion

Biomarkers are objective indicators of particular pathogenic processes, pharmacological responses, or normal biological states; they can involve any kind of molecule in living organs, e.g., proteins, peptides, DNA and/or metabolites. Biomarkers

are essential for the diagnosis and prediction of diseases; IMS can provide distribution information regarding various biomolecules at the cell and tissue levels, and thus it is expected to become a powerful tool for in situ biomarker discovery.

In this chapter, I showed identification of potential biomarkers, which are a molecule that differentiate among the normal, cancerous and even stroma cells in the colon cancer liver metastasis. For this purpose, I showed the statistical strategy is quite effective to deal with the large volume data-set of IMS.

The volumes of IMS datasets continue to increase, because of current improvements to IMS with regards to high resolution [136], three-dimensional (3D) imaging [137], and reconstruction from 3D mass spectra containing ion drift times in ion mobility MS [12]. Data analysis of such large datasets will increasingly depend on the statistical analysis, and therefore the development and application of such analyses will be more important issue.

**Figures and Tables for Chapter 4.**
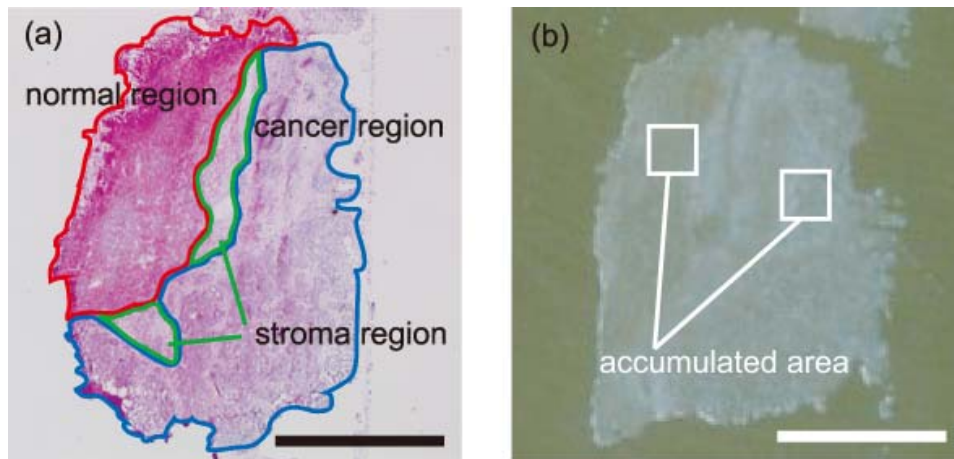
Figure 4-1: Histological observation of HE-stained liver tissue section with colon cancer metastasis. The HE-stained section allows to distinguish the normal, stroma, and cancer cells which were localized on the left, middle, and right location of the section, respectively (a). Photograph of the tissue section prepared for MALDI-IMS (b). From the data points in white squares represented in (b), mass spectra were collected and averaged. Bars, 1 mm.
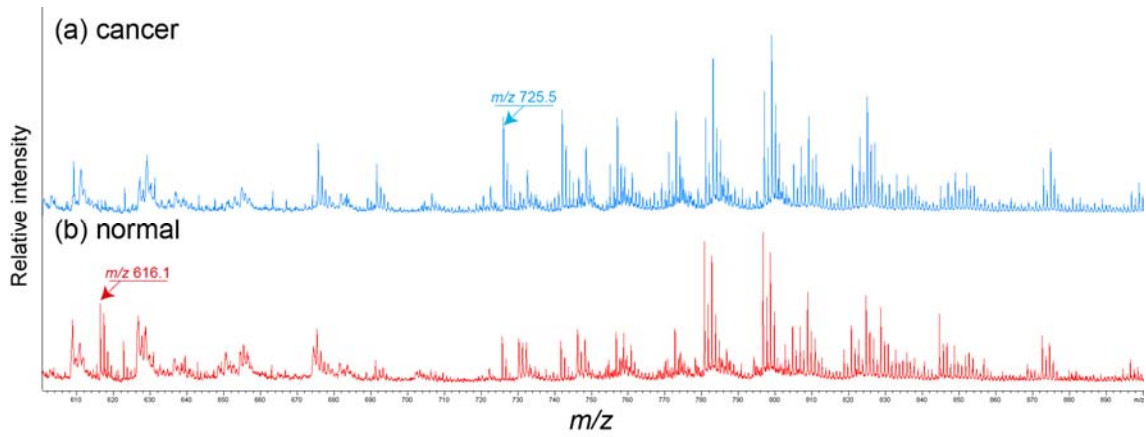
Figure 4-2: Comparison of averaged mass spectra from the cancerous (a) and normal (b) areas.
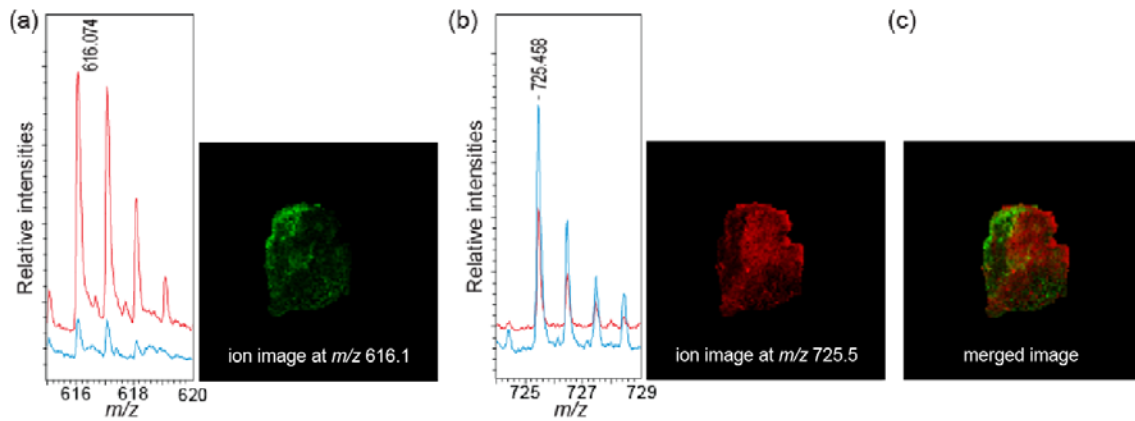
**Figure 4-3: Visualization of molecules specifically localized in normal and cancerous region**.

Ion distribution images and corresponding mass spectra demonstrates the strong distribution of ion at *m/z* 616 in the normal area (a), while the ion at *m/z* 725 showed higher expression in the cancerous area than in the normal area (b). The merged image (c) shows that these two ions were complementary distributed in the specimen.

A

B

(a) MS/MS of *m/z* 616

(b) MS/MS of *m/z* 557 (MS³ of 616)

81
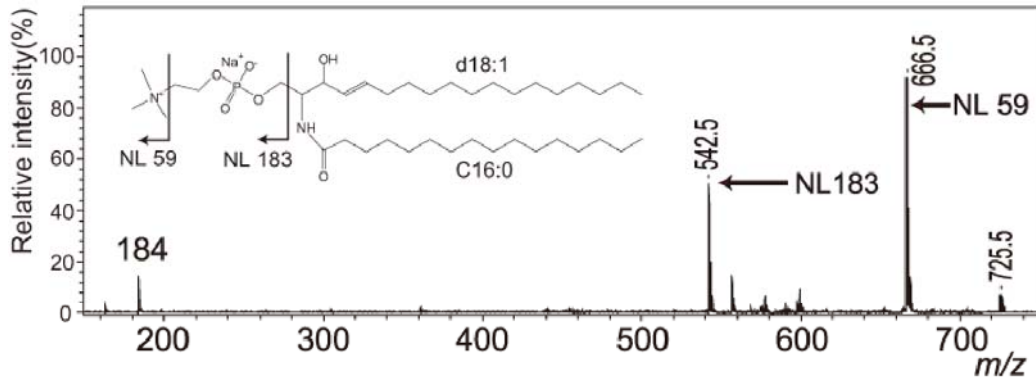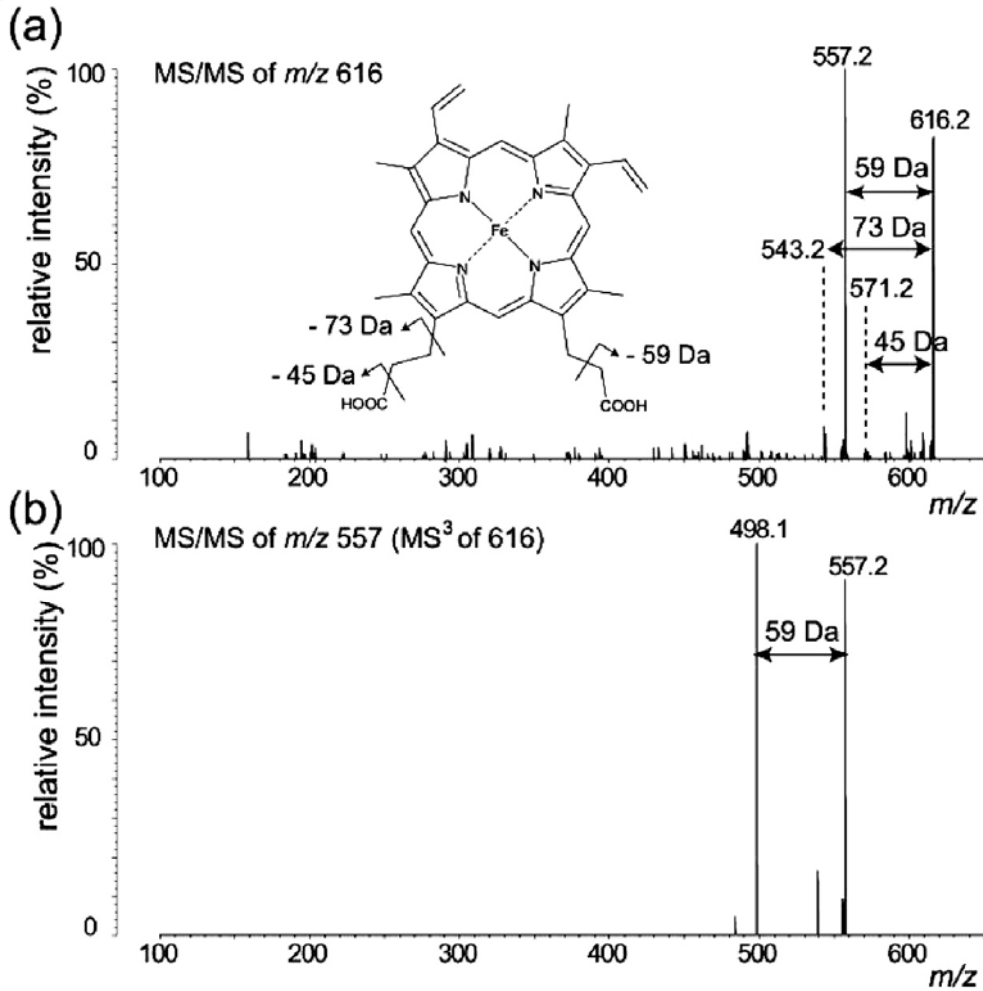
Figure 4-4: Tandem MS enables to molecular identification of interested ions directly on the tissue surface.

A. Product ion mass spectrum on the liver section of *m/z* 725. The neutral loss of 59 u and 124 u observed in the spectra is trimethylamine and cyclophosphate, indicating phosphocholine structure. This fragmentation occurred when alkali metal was adducted the precursor ion. The biomolecule of *m/z* 725 was suggested to be sodiated molecule of SM(16:0).

B. Product ion mass spectra on the liver section of m/z 616.2 (a) and 557.2 (b). The m/z value and fragment patterns indicate that the product ion of m/z 616 is heme-B. Consecutive neutral losses of 73, 59, and 45 Da correspond to CH2CH2COOH, CH2COOH, and COOH, respectively. The molecular structure of heme B is shown as an inset in (a).
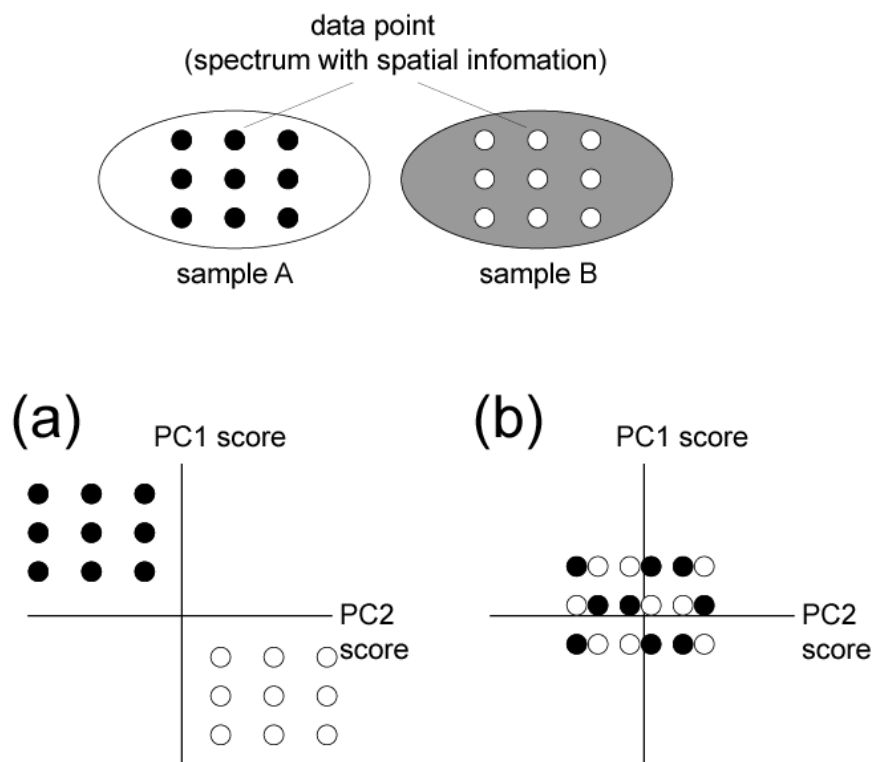
Figure 4-5: Example of data interpretation of IMS linked PCA.

In this study, dots seen in the 2D plot represent the *case*, i.e., spectrum from distinct data points. If dots from distinct sample are separated (a), it means that the molecular expression patterns of these two regions were statistically distinct from each other. If not, PCA failed to extract the statistical differences between the two populations (b).
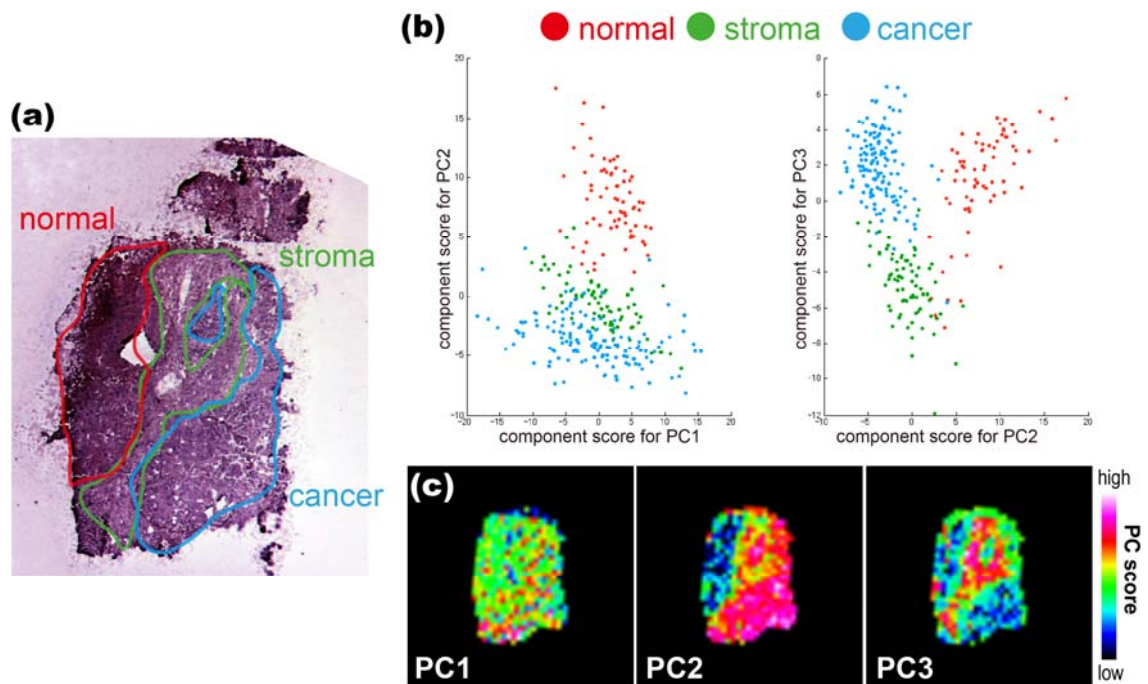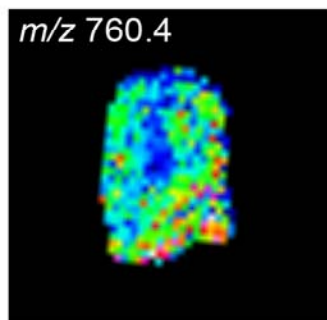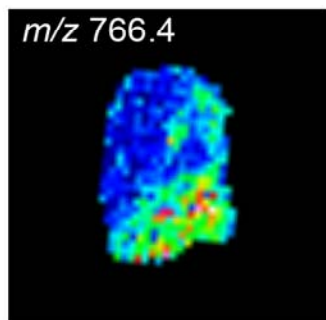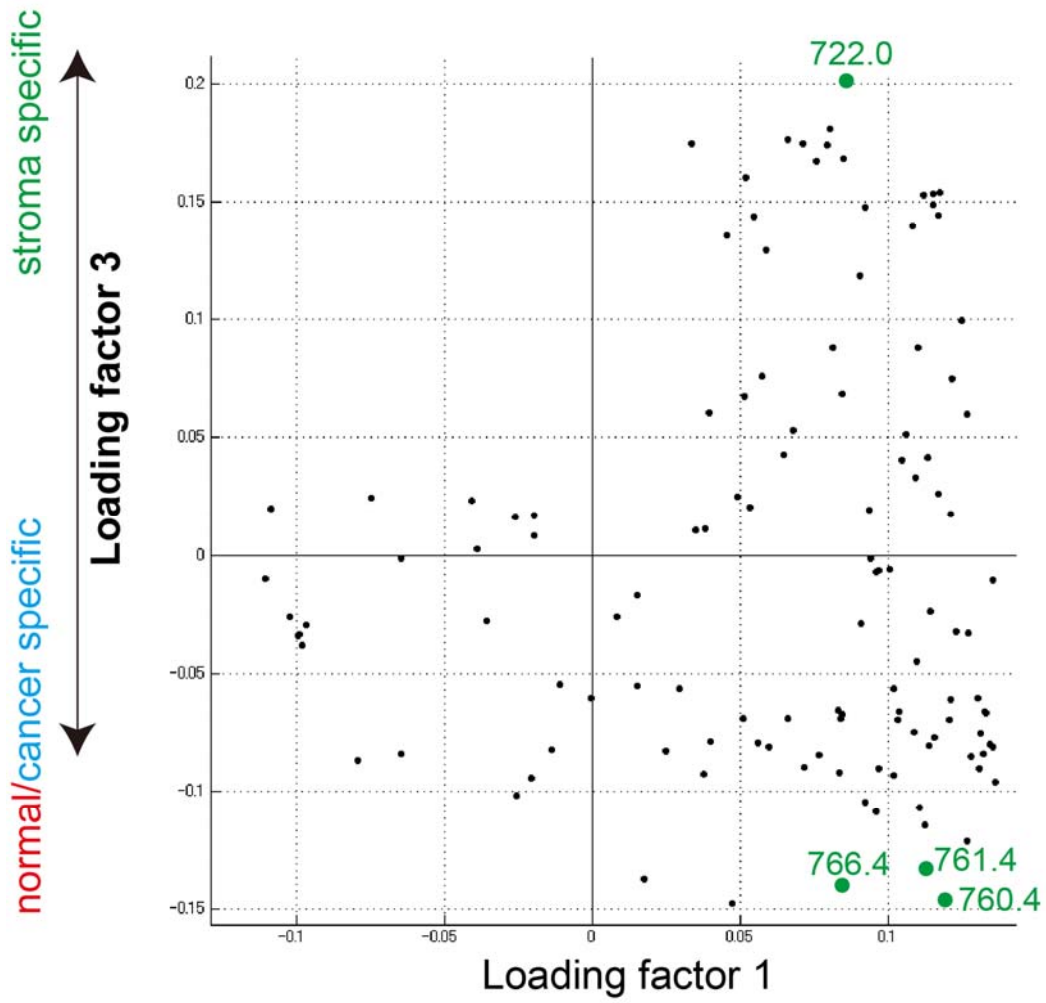
Figure 4-6: IMS linked PCA of colon cancer liver metastasis section revealed altered metabolite comosition among normal stroma and cancer regions.

Optical images of HE-stained section after IMS measurement representing the normal, stroma, and cancer regions (a). Graphs in which principle component scores for PC1, PC2 PC3 are plotted are shown in (b). Principal component images are shown in (c); According to the value of principle component score calculated for the each spectrum at each tissue location, pixels were stained with pseudo-color.
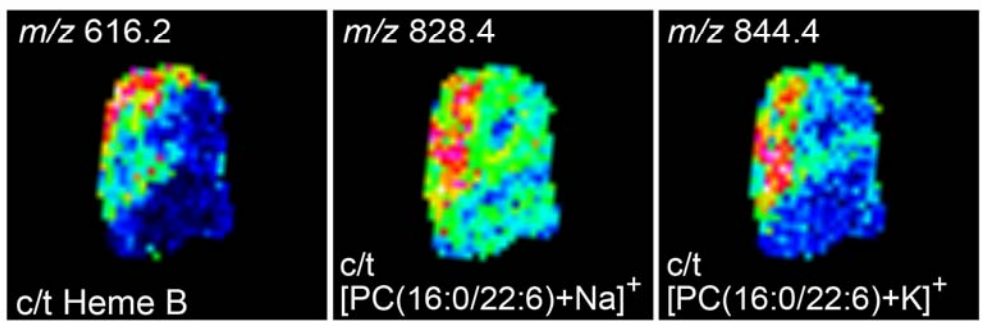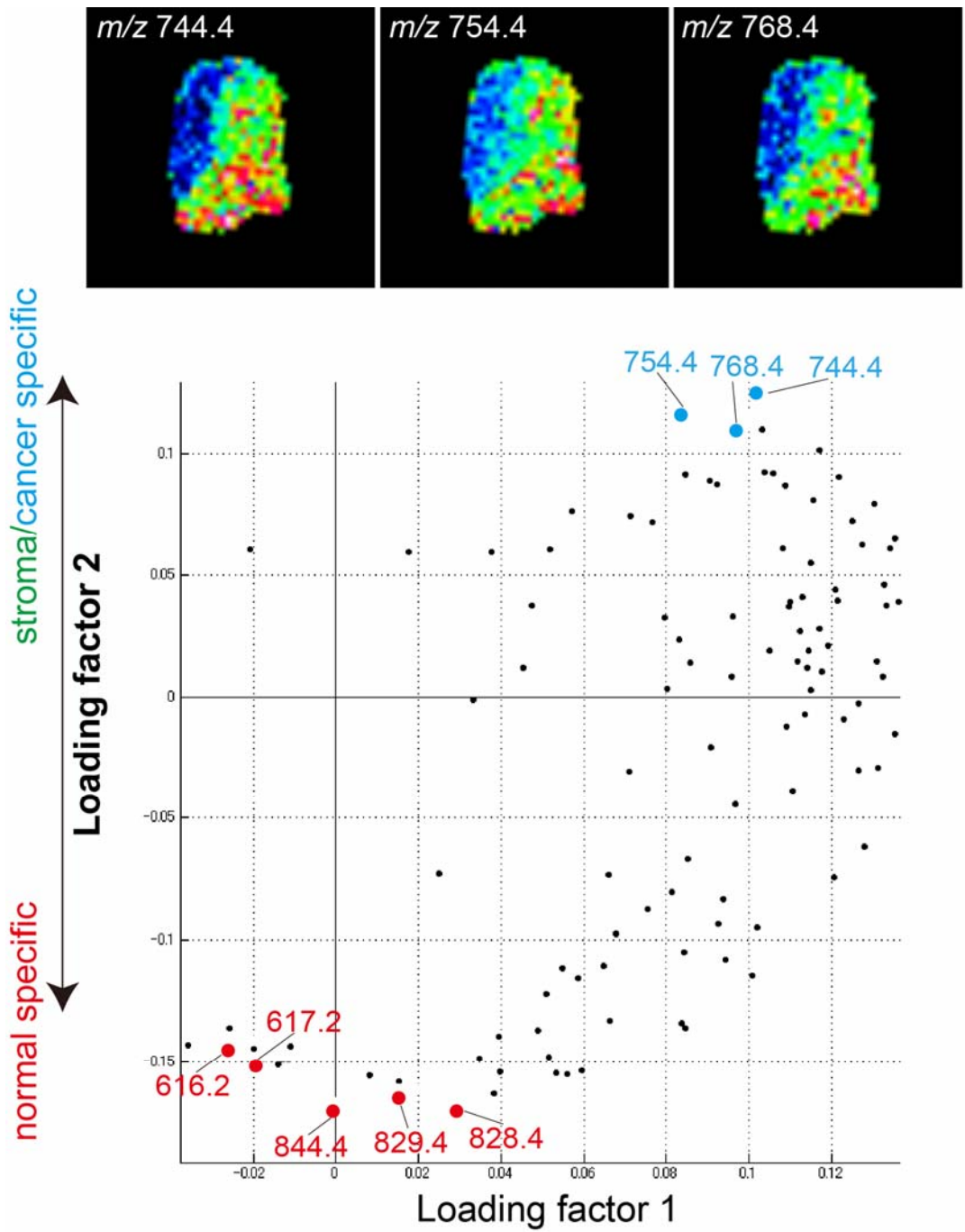
Figure 4-7: PC2 represents difference of metabolic composition between normal vs. other region.

In the center graph, factor loading values for PC1 and PC2 are plotted on x-axis and y-axis, respectively. Each dot indicates the distinct mass peak. The peaks with a large positive/negative value for loading factor 2 (i.e., major contributors to differentiation among the groups) were chosen and their distribution images are visualized. "*c/t*" means "corresponding to".

m/z 722.0

stroma specific

Loading factor 3

normal/cancer specific

722.0

766.4 761.4
760.4

Loading factor 1

m/z 766.4 *m/z* 760.4
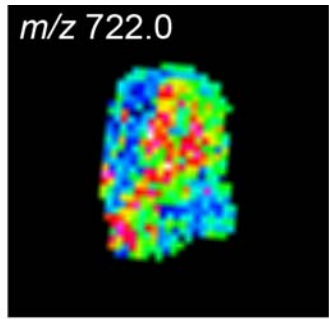
Figure 4-8: PC2 represents difference of metabolic composition between normal vs. other region.

In the center graph, factor loading values for PC1 and PC3 are plotted on x-axis and y-axis, respectively. The mass peaks with large positive/negative value for loading factor 3 were chosen and their distribution images are visualized.

Table 4-1: Results and interpretation of PCA of the liver section with colon cancer metastasis

		Primary contributing PCs			Interpretation of the component
Component 2	negative	m/z 616.2（heme B）	m/z 828.4 （c/t [PC(diacyl-16:0/22:6)+Na]+）	m/z 844.4 （c/t [PC(diacyl-16:0/22:6)+Na]+ ）	representing altered metabolite composition between normal and other regions.
	positive	m/z 744.4	m/z 754.4	m/z 768.4	

		Primary contributing PCs			Interpretation of the component
Component 3	negative	m/z 722.0	-	-	representing altered metabolite composition between stroma and other regions.
	positive	m/z 760.4	m/z 766.4		

Chapter 5: Visualization of metabolic dynamics by mass spectrometry

1. Introduction

In previous chapters, I showed that IMS is an effective technique to visualize a large number of metabolite molecular species simultaneously on a single tissue section. As demonstrated, studies using IMS have revealed that lipid metabolites distributed rather heterogeneously, even in cell selective manner, in the mouse brain[19]. These observations raise a fundamental question; do the localized small metabolites play specific functional roles to each neural cell-type *in vivo*? If so, how can we analyze them? To know this, in this chapter, I analyzed dynamic changes of metabolites on neural stimuli, in their amount and distribution pattern. Differential analysis using IMS between control and stimulated samples provided key information about which kind of cells are stimulated and what kind of metabolic pathways are involved in the neural activity on the stimuli.

Here, using IMS and other technique, I established experimental system to profile the metabolite dynamics i.e., the fluctuation in their expression with time and space, *in vivo*. I focused on analysis of lipids and uncovered the region specific dynamics of several specific lipids on stimulation by IMS conjunction with laser capture micro dissection (LCM) technology. As a first step, I visualized the dynamics of abundant phospholipid molecular species induced by kainate administration, which is widely used as a model of limbic seizures, in mouse hippocampus by IMS. Next, LCM conjunction with enzyme immune assay (EIA) completes the micro region profiling of lipid metabolites, especially of extremely small amount lipids; bioactive lipids such as prostaglansins (PGs) regulate various physiological events at very low concentration, and their dynamics were also analyzed with spatial information. The results indicate

poly-unsaturated fatty acids (PUFAs), especially arachidonic-acid (AA) were specifically released in the granule cell layer of dentate-gyrus (DG) in the mouse hippocampus and metabolized to PGs. My approach completes a comprehensive profiling of lipid metabolites on the specific tissue location, towards *in situ* metabolomics.

2. Materials and Methods

Kainate administration, Eight-week-old male C57BL/6J mice were intraperitoneally injected with kainate (25 mg/kg body weight, in saline) and then sacrificed at indicated time points. Animals treated for 3 and 24 h were rated for seizure severity based on a previously defined rating scale [56, 138]; those with a score above stage 5 were used. All experiments with mice were conducted using protocols approved by the Animal Care and Use Committee of the Mitsubishi Kagaku Institute of Life Sciences.

Sample preparation and IMS: Tissue preparation and IMS were performed as described previously [67], using a 2,5-dihydroxybenzoic acid (DHB) matrix solution (50 mg/mL DHB dissolved in 20 mM sodium acetate, 0.1% TFA, and 70% methanol). Matrices were applied simultaneously to the tissue sections that were to be compared in order to equalize the analyte extraction and co-crystallization conditions. Mass spectrometry was performed as described previously, using an Ultra Flex 2 MALDI-TOF mass spectrometer (Bruker Daltonics, Leipzig, Germany) equipped with a Nd:YAG laser. Briefly, data were acquired in the positive-reflectron mode under an accelerating potential of 25 kV. Each spectrum was the result of 100 laser shots on each data point. In this analysis, signals between *m/z* 400 and 1000 were collected. The interval between data points was 20 μm; thus, we obtained a total of approximately 6000 data points for

each hippocampal region. Image reconstruction was performed using FlexImaging 2.1 software (Bruker Daltonics).

Spectrum Normalization, In this study, the variance of ionization efficiency, which is caused by the heterogeneous distribution of matrix crystals and their sublimation during measurement, was eliminated for each data point by equalizing the total ion current of each mass spectra. Also, I used the internal standard (IS) method to normalize spectra obtained from control and kainate-administered mice. Spectra for comparison (i.e. spectra obtained from same hippocampal areas, in different condition) were normalized to have same intensity of IS peak.   To choose an IS peak whose expression level does not change significantly during stimulation (control vs. kainate-administrated (0.5 h)), I defined a PIS (pseudo-IS) index which are defined for each mass peak as follows:

$$PIS_{index}(m/z) = \sum_{n} \left| \left(\frac{A_n / A_{m/z}}{B_n / B_{m/z}} \right) - 1 \right|$$

A = intensity of mass peaks in spectrum A

B = intensity of mass peaks in spectrum B

n = number of mass peaks

In the drug-administrated condition, I assumed that expressions of specific metabolites are significantly altered, while large number of other metabolites did not change their expression levels significantly. In such condition, a low PIS-index value represents that variations in peak level are small among the different conditions, and thus such peaks were adequate as IS. I computed the formula with used 15 intense mass peaks (n=15) and six peaks show low PIS-index values (Table 5-1).

I chose the peak at m/z 756.4, which was derived from the PC(diacyl-16:0/16:0) and its invariability was confirmed by RPLC/ESI-MS/MS using external standard method (Supplemental Table) . In consequence, the normalized spectra, which used *m/z* 756.4 as IS, resulted in a high correlation (r^2) and linearity (slope) (Figure 5-1).

Other Data processing, Spectra from regions of interest in tissue sections under each condition (i.e., control and kainate-treated) were averaged and then normalized using the internal standard peak (refer to SI). Peaks were selected using FlexAnalysis (Bruker Daltonics), and relative differences in peak intensity between the kainate-treated and control samples were computed by simple arithmetic division. The agglomerative hierarchical clustering algorithm in Eisen's software was applied to investigate the metabolite expression pattern in response to the kainate treatment.

Laser Capture Microdissection (LCM) and enzyme immne assay (EIA), Thirteen micrometer sections of frozen mouse brains were sliced and freeze-dried in the cryo-chamber (CM 3050;Leica, Germany). Approximately 10 coronal sections from a single mouse brain were microdissected with a Leica LMD Laser Capture Microdissection System (LMD 6000), from indicated hippocampal regions. Laser capture microdissected tissues were immediately dissolved in 20 µl of methanol, and used for EIA within a day. The concentration of PGF2a was assessed by EIA (Cayman, Ann Arbor, MI U.S.A.). All samples were run in triplicate, standard curves were run on the same plate, and the standard-curve method was used to calculate the concentration of PGF2α.

Sample preparation for LC/ESI-MS/MS, The ESI-MS/MS analysis was performed using a 4000Q-TRAP quadrupole linear ion trap hybrid mass spectrometer (Applied Biosystems/MDS Sciex, Concord, ON, Canada) with an ACQUITY Ultra Performance LC® (Waters, Milford, MA). The samples were resolved on the ACQUITY UPLCTM BEH C18 column (1.0 × 150 mm i.d., 0.17-μm particle) and then subjected directly to ESI-MS/MS analysis. Ten microliters of the samples injected by the autosampler were directly introduced, and the samples were separated by a step gradient with mobile phase A (acetonitrile:methanol:water = 19:19:2 v/v/v containing 0.1% formic acid and 0.028% ammonium):mobile phase B (isopropanol, 0.1% formic acid, and 0.028% ammonium) ratios of 95:5 (0–5 min), 70:30 (5–40 min), 50:50 (40–41 min), 50:50 (41–90 min), and 95:5 (90–120 min) at a flow rate of 70 μL/min and a column temperature of 30 °C.

LC/ESI-MS/MS: To identify the PC species, precursor ion scanning was performed using the 4000Q-TRAP instrument; these methods are effective for detecting PCs because characteristic fragment ions are generated by collision-induced dissociation (CID) .

3. Results and discussion

Spectrum normalization and validation analysis of MSI for metabolite dynamics

Until here, I have demonstrated that IMS enables the visualization of the multiple metabolites on a single tissue section. Furthermore, I have revealed large changes of metabolite composition during neural development (within months or years). Next challenge is to visualize the metabolic dynamics between the control and stimulated samples, within much shorter time (within hours). For this purpose, improvement of

IMS on quantitative ability is necessary; basically, direct MALDI-MS obviate tissue extirpation and analyte extraction procedures, thereby reducing variations in sample preparation. However, the ionization efficiency of analyte on tissue sections could vary depending on the matrix-analyte co-crystallization conditions[122], so the absolute intensity of mass spectra should be processed using an adequate normalization method among different samples or measurements. The normalization process enables the direct comparison of spectra by projecting data sets onto a common intensity scale, and so far, several normalization methodologies for mass spectrometric measurement have been developed [139-141]. I performed normalization of the spectra obtained from different tissue sections with both total ion current (TIC) and an internal standard (IS) whose expression level did not change (in following study, peak at m/z 756.4 was used. Also refer to methods). Firstly, the variance of ionization efficiency in each data point, which is caused by the heterogeneous distribution of matrix crystals and their sublimation during measurement, was eliminated by equalizing the TIC of all obtained mass spectra. Next, the variance among the different conditioned tissue sections caused by variations of sample preparation processes were normalized using IS peak and it facilitated further precise correction of metabolite expression intensity. In this study, the latter normalization was performed for quantitative analysis subjecting the averaged spectra collected from each corresponding hippocampal areas of different sections, and for visualization analysis subjecting the spectra from the entire hippocampal areas.

To evaluate the accuracy and reproducibility of mass signals for metabolites obtained by this procedure, I compared 2 averaged spectra collected from the entire hippocampal region regarding the peak intensities of 857 mass peaks, obtained from different mice. After the normalization, intensities of these mass peaks in the 2 spectra were strongly

correlated ($r^2 = 0.996$) (Figure 5-1A). After normalization by internal standard peak, the correlation was even better than that between the 2 spectra obtained by conventional MALDI-mass spectrometry in which independent lipid extracts from the mouse hippocampus were analyzed ($r^2 = 0.984$, data not shown).

On the other hand, the 2 mass spectra obtained from the hippocampi of the control and kainate-administered mice (0.5 h post-administration) revealed a lower correlation ($r^2 = 0.961$ for the tissue and $r^2 = 0.936$ for the extract, data not shown; Figure 5-1A) by reflecting kainate-induced alteration on metabolism. Representative examples of mass spectra obtained at each time point after kainate administration are shown in Figure 5-1B. While the overall peak pattern of mass spectra between both the sample groups are quite consistent, kainate altered the intensity of several mass peaks. For example, the peaks indicated by blue arrowheads were rapidly decreased in intensity at 0.5–3 h and gradually recovered at 24 h (Figure 5-1B). In contrast, the intensity of the peaks labeled with red arrowheads transiently increased and then slightly decreased after kainate administration.

Kainate is a glutamate analog that has been widely used in pharmacological studies of neuronal injury related to ischemic conditions and epilepsy [142] as well as for neuronal plasticity[143]. Though evidences of abnormal neural metabolism were reported in early studies of kainate-induced epilepsy [144] and the visualization of kainate-induced genes and protein expressions have been intensively studied [145], little, if any, information was available regarding the alteration of metabolites previously. IMS and our data analysis firstly provided the reproducible detection of kainate-induced metabolic alteration directly on tissues.

Region-specific analysis by IMS revealed the specific reduction of PUFA-PCs in response to kainate.

PCs are not only the major components of plasma membrane but also possible source of lipid messengers, and they are known to alter their metabolism during epileptic seizures [146]. Elucidation of the alterations in their distribution and expression levels during kainate-induced seizure is key to understanding their functional roles as structural components of biological membranes as well as in the storage of bioactive lipid precursors during neural stimulation.

First, I determined the composition of PC subtypes in the mouse hippocampus by using a 2-dimensional map of PCs in conjunction with a reverse-phase liquid chromatography/electro spray ionization (RPLC/ESI)-MS/MS system [22, 147] (Figure 5-2A and Table1), and then assigned the 10 abundant PCs to the mass peaks detected by IMS. Next, I validated the assignment by applying direct MS/MS on the hippocampal tissue surface (Supplemental Figure S8). It is notable that hippocampal phospholipids have greater AA content than other areas of the brain [22, 147], and this is also true with regard to PC (Table 5-2).

In this analysis, IMS facilitates the analysis of changes of mass signals in micro tissue regions with cellular resolution. Here I collected and averaged the mass spectra from 3 hippocampal regions, namely, the dentate gyrus (DG), granule cell layer of the DG, and the pyramidal cell layer of CA1, and the entire hippocampal area (as shown in Figure 5-3). To understand overview of kainate-induced alteration with spatial information, the relative expression levels of PCs in the hippocampal regions at each time point were computed, and the local dynamics of PCs were obtained and classified by hierarchical cluster analysis. Figure 5-2 shows the results of hierarchical cluster analysis of the

97

expression patterns of the 10 abundant PCs in the 4 hippocampal regions. It clearly revealed the rapid reduction and recovery trends of PUFA-PCs in response to the stimuli, while it was not observed for PCs containing saturated fatty acid (SFA) or monounsaturated fatty acid (MUFA). In particular, DHA-PCs exhibit a massive decrease among the regions of the hippocampus, while cell layer-specific (*CA-1 soma* and *DG-soma* region) decreases were observed for AA-PCs.

Visualization of the dynamic changes in PUFA-PCs during KA induced seizure

  Visualization of the reductions in PUFA-PCs showed that they occurred in specific hippocampal regions. Figure 5-3 shows the results of imaging and the time course plot of the relative expression level for 2 major SFA/MUFA-PCs, namely, PC(diacyl-16:0/16:0) and PC(diacyl-16:0/18:1). Interestingly, these 2 abundant PCs showed rather different distributions in the basal state. While PC(diacyl-16:0/16:0) was strongly distributed in the dendritic region of the hippocampus, PC(diacyl-16:0/18:1) tended to localize in the pyramidal cell layer of CA1 and granule cell layer of the DG region. PC(diacyl-16:0/18:1) showed a slight and temporal decrease in these regions, but analysis of the entire region did not show significant reduction.

In contrast, visualization of PUFA-PC expressions revealed a dynamic decrease by kainate treatment. In the basal state, AA-PCs were prominently detected in the cell layer of CA1 and DG and showed a higher expression level in the latter (Figure 5-4A, arrowheads). I found that expression of the 2 major AA-PCs (*m/z* 804.5 and 832.5) was rapidly decreased at these cell layers in a rather region-specific manner and that AA-PCs in the cell layer of DG showed more prominent reduction. With regard to DHA-PCs, strong signals of the 2 major subtypes (diacyl-16:0/22:6 and

diacyl-18:1:0/22:6) were commonly detected in the CA3 region, stratum

lacunosum-moleculare, and the molecular layer of DG (Figure 5-4B, arrows).

Reductions in DHA-PCs following stimulation occurred not only in the cell-layer region

but also in the dendritic region of the hippocampus. I verified that the reductions in

PUFA-PCs were also observed in hippocampal lipid extracts with the LC/ESI-MS/MS

system by using the external standard method (Figure 5-5). I confirmed that PUFA-PCs

showed specific reduction and that, as observed in IMS experiments, DHA-PCs showed

more prominent decreases than AA-PCs. Slight decreases were observed for

SFA/MUFA-PCs, but they were insignificant (less than 5% of the control samples).

Visualization of the dynamic changes in lyso-PCs

 The abovementioned observation indicates the preferential cleavage of PUFA-PCs by

activated PLA_2 during kainate stimulation, because some PLA_2 subtypes are activated

by the Ca^{2+} influx and preferential hydrolysis of PUFA-phospholipids [148]. In addition to

these results, our method also facilitates the visualization of the expression of lyso-PCs,

which are the enzymatic products of PLA_2 activity. As anticipated, the corresponding

signals of lyso-PC(16:0) at *m/z* 518.3 and lyso-PC(18:0) at *m/z* 546.3 were classified

into the up-regulated cluster in the initial analysis. Interestingly, results of the imaging

analysis clearly outline the mossy fiber pathway (Figure 5-6A. arrowheads), and I

visualized their elevated expression following kainate treatment. While these images

reveal the strong expression of lyso-PCs in the mossy fiber-containing region, the most

prominent increase rate was detected in the DG granule-cell layer region in which major

reductions of AA-PCs and DHA-PCs were observed. High-magnification images

clearly show massive production of lyso-PC(16:0) in the granule cell layer, where

lyso-PC is rarely expressed in the basal state (Figure 5-6B, arrowheads).

These observations indicate that following the kainate treatment, AA-PCs are cleaved within the cell layer and produce lyso-PCs in the same regions. Indeed, kainate-induced reduction of membrane phospholipids and marked accumulation of AA and DHA were reported to be observed in brain lipid extracts [23]. Our technique visualized this phenomenon with cellular resolution and revealed that it occurred in a rather region-specific manner in the mouse hippocampus. In particular, the reductions in AA and DHA in the cell layers suggested the involvement of cytosolic- PLA_2 ($cPLA_2$) which is found in juxtanuclear location within cells [51, 149]. Sensitive responses in the DG granule cells are attributable to the high-density expression of presynaptic kainate-receptor subunits by neurons [150].

DG-granule cell specific production of prostaglandin F2α in response to KA-stimulation

As shown, by utilizing IMS, I demonstrated that following kainate administration, the expression of PCs particularly PUFA-containing PCs were dynamically altered in a region-specific manner. These observations suggest that PUFA-PCs are rapidly cleaved in distinct regions by stimulated PLA_2 activity, and this raises further questions; were the released-PUFAs converted into bioactive lipids such as PGs? If so, can I profile the productions of such bioactive-lipids within small tissue regions? However, the concentration of PGs is maintained at much lower than those of precursor phospholipids (such as AA-PCs) in the body, thus detection/imaging of such less-abundant metabolites are rather challenging issue in MALDI-IMS. Because tissues and cells are directly subjected to IMS measurement, numerous molecular species compete for ionization;

eventually, abundant molecules could be preferentially be detected while suppressing the ionization of trace molecules. This phenomenon is called the "ion suppression effect" [151-153]

Figure 5-7 shows a strategy to overcome this problem. To profile such less abundant lipids from tissues with distribution information, at first, tissues of three interested micro regions. In this case, according to the previous IMS results (Figure 5-4), CA-pyramidal cell layer and CA1-SR, and DG-granule cell layer were dissected and collected by LCM technology. Then, after careful extraction of lipids from the dissected tissues, trace PGs were quantified by EIA. Figure 5-8 shows the result of quantification of PGF2α from the three small hippocampal regions, on both with/without the KA administration. The increased production of PGF2α was observed in all analyzed regions, and the DG neurons showed particularly notable burst of the PGF2α (approx. two times higher than other regions).

Together with the DG-cell specific decrease of AA-PCs at 0.5h post dose (Figure 5-4) and increase of LPC (Figure 5-6), these results propose a "cell-selective" AA-metabolism on KA stimulation in the hippocampus. Presented results are consistent with the previously reported study which shows the hippocampus selective production of PGs, especially of $PGF_2\alpha$, compared to cerebral cortex region, on KA stimulation [51]. My study adds the further detailed localization information and even revealed the cell specificity of AA-metabolism. In particular, DG-granule cells were supposed to have strong metabolic activity which converts AA into PGs (Figure 5-9; Under KA stimulation, arachidonoyl-PCs were hydrolyzed presumably by stimulated PLA_2 activity on elevated Ca^{2+}, and LPC and AA were produced. Released PUFAs are converted into various lipid mediators [154]. The immediate release of AA initiates the production of

considerable and sustained concentrations of AA peroxides, which are characterized by a toxic, destructive, and inactivating action, particularly on membrane receptors [155]. From the presented results, the DG-cells are suggested to have an specific mechanism involving a PLA_2 localization/activation, which preferably hydrolyze AA-PCs. Due to the large molecular family of PLA_2 and their complex regulation mechanism, further study is required to elucidate it, and application of presented strategies to genetically modified mice of PLA_2s will be quite effective to asses their functional role in the brain. Finally, recent study revealed that the released DHA is oxygenated to produce neuroprotective agents against the oxidative damage caused by free radicals [156] in contrast to the PGs. In the mouse retina, DHA was found to modulate neuronal excitability by reducing KA-induced responses [156]. Coupled with the characteristic localization of DHA-PCs (i.e., localized storage of these DHA), DHA are strongly suggested to play cell type-specific roles in the hippocampus. Though their precise role in brain is still unknown, presented strategy could also be applied for the analysis of them. Because they are closely associated with synaptogenesis, neuronal plasticity, neuronal survival, and learning and memory, detailed understanding of the mechanism of lipid-mediators production will provide a biochemical basis for understanding the roles of them in the brain.

Figures and Tables for Chapter 5.
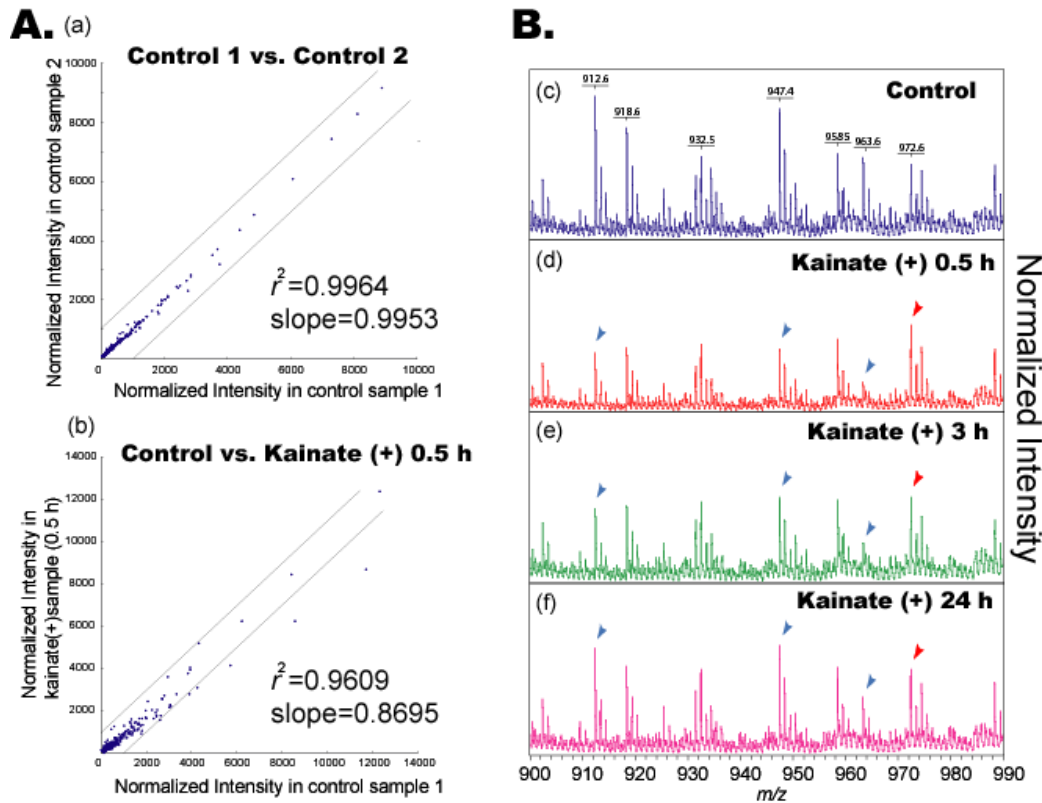
Figure 5-1: IMS was used to detect the kainate-induced changes in metabolite expression. Mass spectra were collected from the entire region of the mouse hippocampus treated with kainate or in the absence of kainate (control) and normalized with the internal standard peak (*m/z* = 756.4). A. Validation analyses of metabolite expression profiles with MALDI-IMS. Correlation analyses of quantitative data between 2 different control samples (a) or control *vs.* kainate-treated samples (0.5 h post-administration) (b). Kainate-induced alteration in metabolite expression was reflected to have a lower degree of correlation. B. Representative mass spectra from control samples (c) and kainate-administered mice (d–f). The mice were sacrificed at the indicated time points following administration. Arrowheads indicate the mass peaks that are transiently decreased (blue arrowheads) or increased (red arrowheads) in response to the kainate treatment (B, d-f).

A.

B.

Cluster 1   Cluster 2   Cluster 3

Cluster 1

Cluster 2

Cluster 3
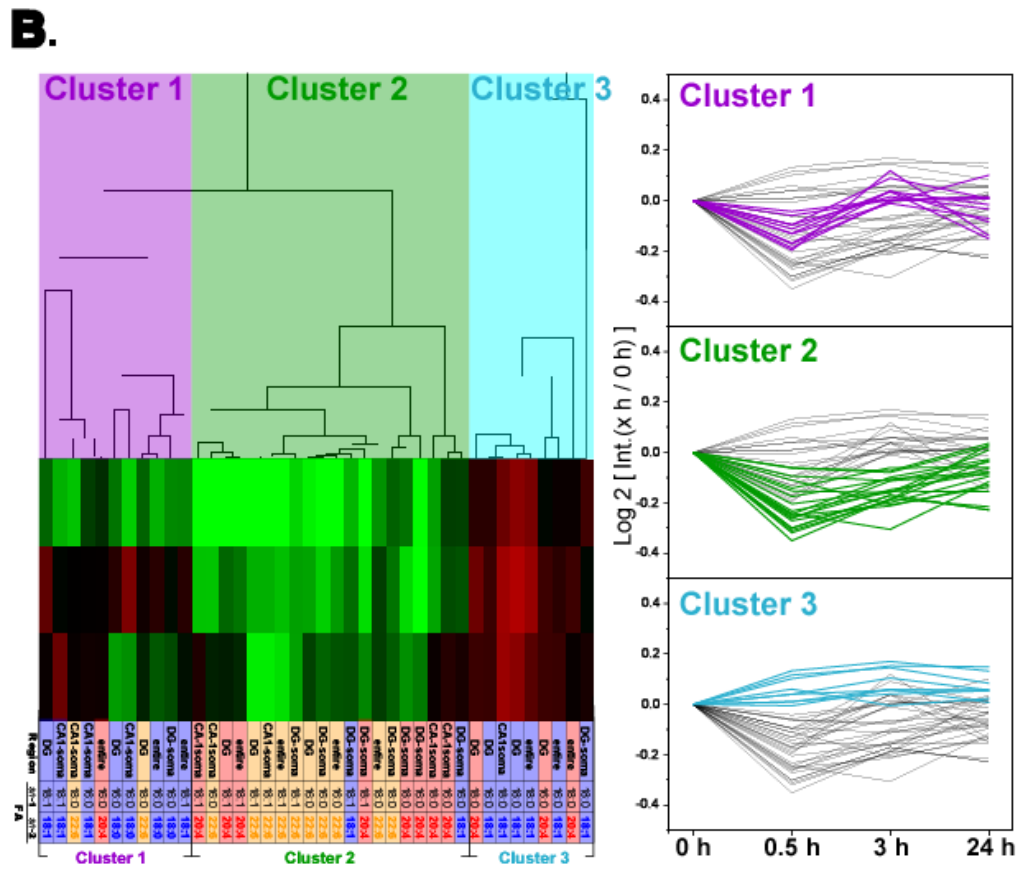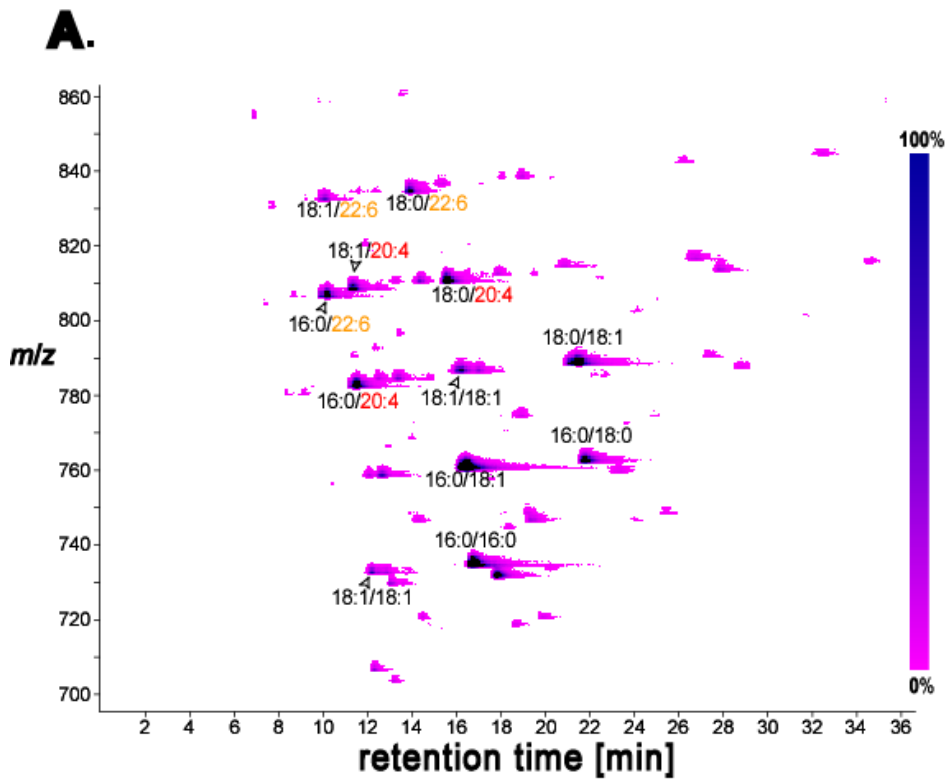
Figure 5-2: *In situ* **metabolomics revealed region-specific reductions in PUFA-PCs following kainate administration.**

A. Two-dimensional map of the PC mixture from the mouse hippocampus was obtained by RPLC/ESI-MS/MS. The 2-dimensional map shows m/z values along the vertical axis and the retention times along the horizontal axis. Spots corresponding to abundant PCs that were commonly detected with LC/ESI-MS/MS and IMS were assigned.

B. Hierarchical cluster analysis of the expression dynamics of 10 abundant PCs in 4 hippocampal regions in response to kainate administration (left). They were classified into 3 categories. Cluster 1 showed a slight transient decrease at 0.5 h, and cluster 2 showed massive reduction. Profiles with unaltered expression were classified as cluster 3 (right). DHA-PCs (orange) and AA-PCs (red) were specifically decreased, whereas SFA/MUFA-PCs (blue) did not show considerable reductions. In particular, AA-PCs showed cell layer-specific reduction after the kainate treatment. In the IMS experiment, I added sodium acetate in the matrix solution; thus, PCs were detected in the $[M+Na]^+$ ion form.
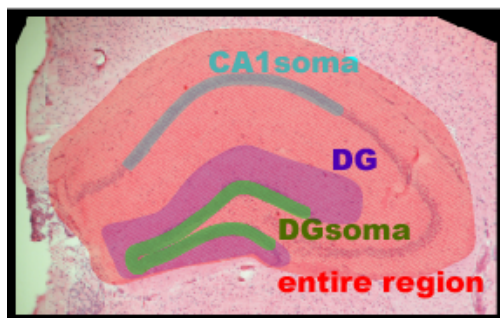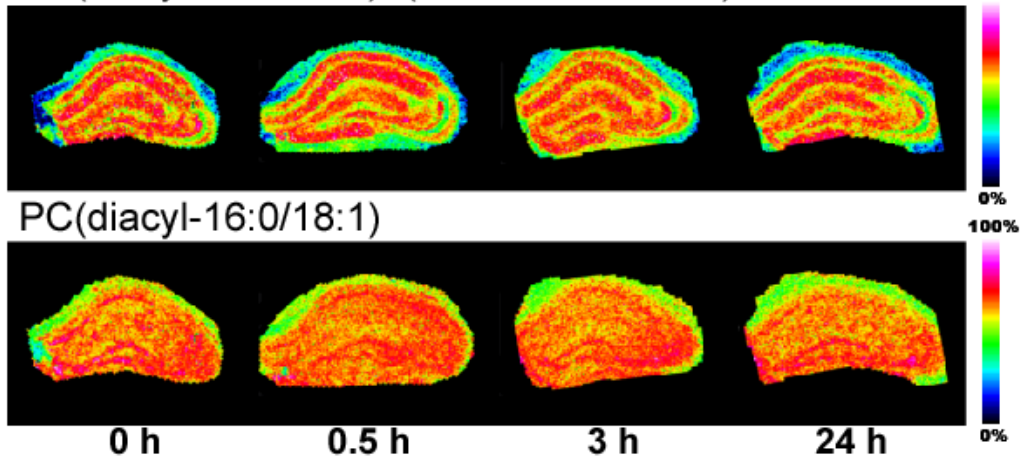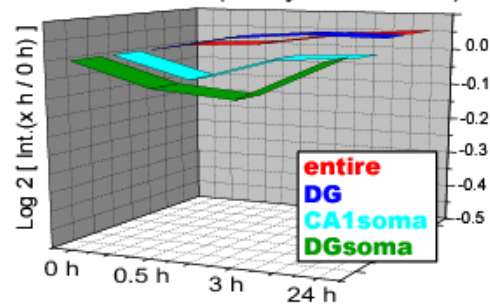
Figure 5-3: SFA/MUFA-containing PCs did not show an alteration in both their expression levels and distribution patterns after kainate administration.
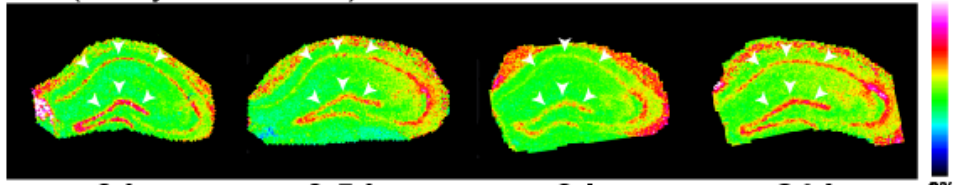
Spatiotemporal distribution of SFA/MUFA-PCs (PC(diacyl-16:0/16:0) and PC(diacyl-16:0/18:1)) in the hippocampus after kainate administration (upper panel). The kainite treatment did not alter their distribution pattern. Coronal section of the mouse hippocampus stained with HE showed staining of the hippocampal regions of the CA1-pyramidal cell layer, DG-granule cell layer, DG, and the entire hippocampal area from which mass spectra were obtained (lower panel, left). Time course plot of the expression level in these regions revealed their unaltered expression following stimulation (lower panel, right).

A. AA-PCs

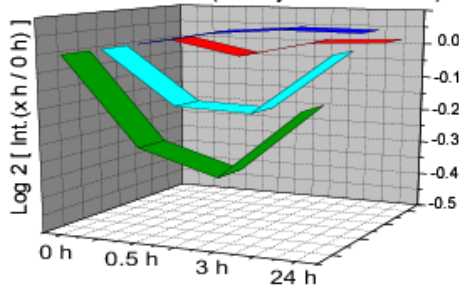PC(diacyl-16:0/20:4)
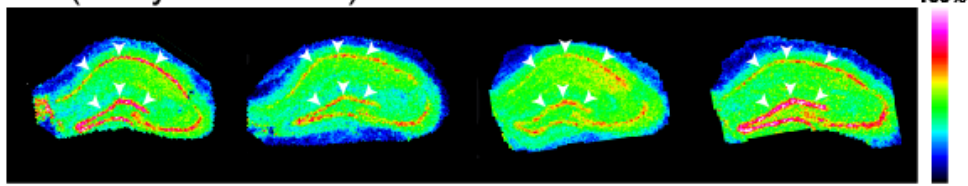
PC(diacyl-18:0/20:4)
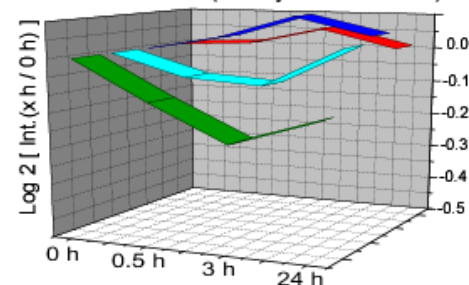

0 h   **0.5 h**   **3 h**   **24 h**
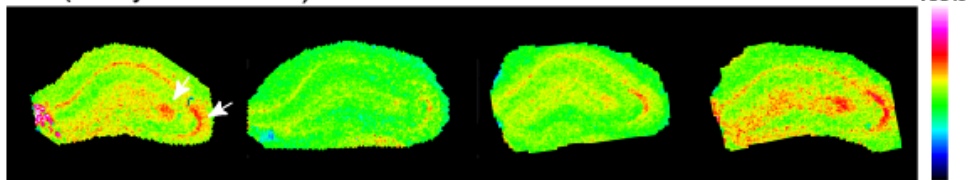
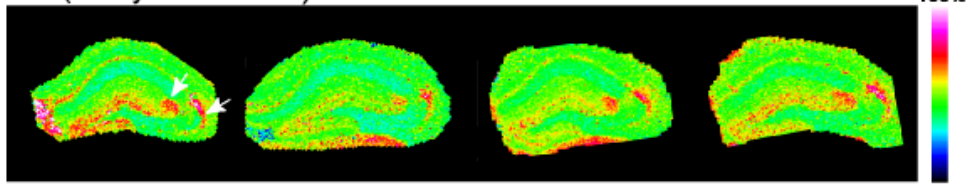*m/z* 804.5 PC(diacyl-16:0/20:4)

m/z 832.5 PC(diacyl-18:0/20:4)

B. DHA-PCs

PC(diacyl-16:0/22:6)

PC(diacyl-18:0/22:6)

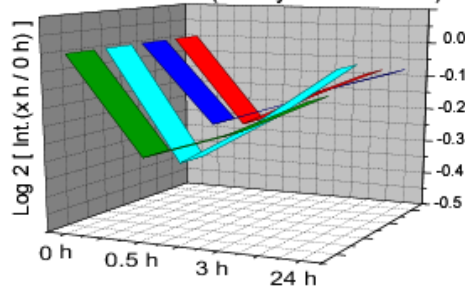

0 h   **0.5 h**   **3 h**   **24 h**

m/z 828.5 PC(diacyl-16:0/22:6)

m/z 856.6 PC(diacyl-18:0/22:6)

107
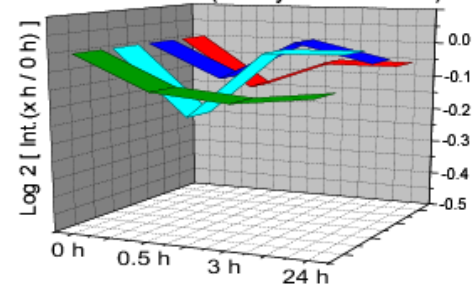
Figure 5-4: PUFA-containing PCs showed decreased expression levels in a region-specific manner following kainate administration.

A. Spatio-temporal distribution of AA-PCs (PC(diacyl-16:0/20:4) and PC(diacyl-18:0/20:4)) in the hippocampus after kainate administration (upper panel). Imaging of AA-PC expressions visualized their cell layer-specific reduction after kainate stimulation (upper). The time course plot of their expression level also indicates the region specificity of the reduction (lower panel).

B. Spatiotemporal distribution of DHA-PCs (PC(diacyl-16:0/22:6) and PC(diacyl-18:0/22:6)) on the hippocampus (upper panel). Imaging of DHA-PC expression dynamics (upper) and time course plot of expression level (lower panel) indicate their massive reduction in the hippocampal area.
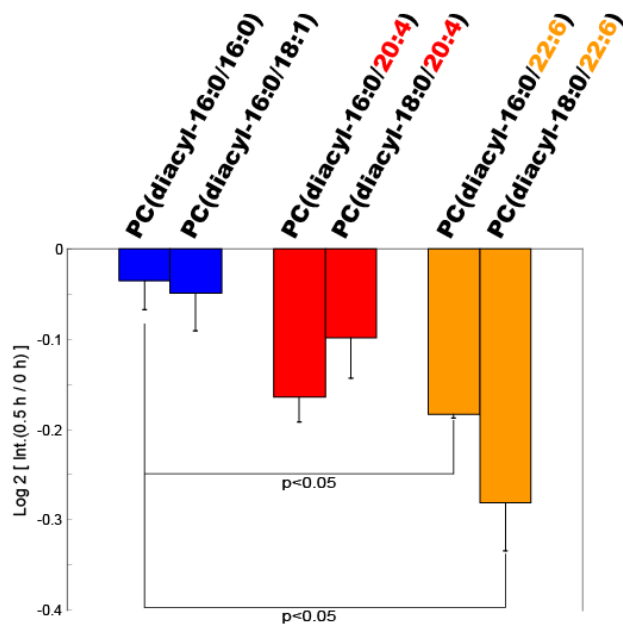
Figure 5-5: The LC/ESI-MS/MS system verified the specific reduction of PUFA-PCs after kainate administration in the hippocampal lipid extracts.

Hippocampal tissues were dissected from the mice of the control and kainate-administrated group (0.5 h post-administration), total lipids were extracted, and 3 pairs of control and kainate-treated mice were examined. Expression levels of PC were quantified using the LC/ESI-MS/MS system with LPC(17:0) as the external standard. Data were expressed as mean + S.E.
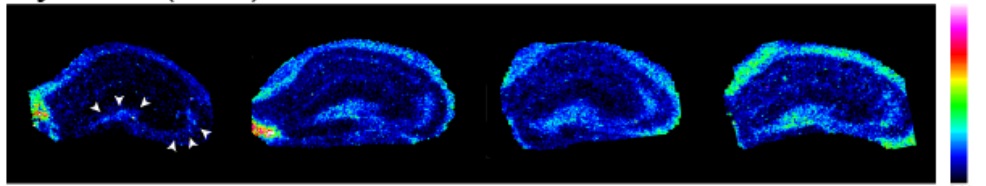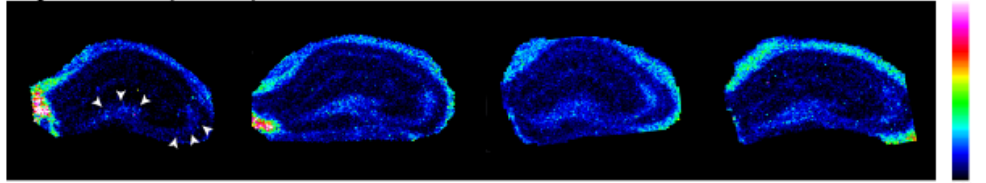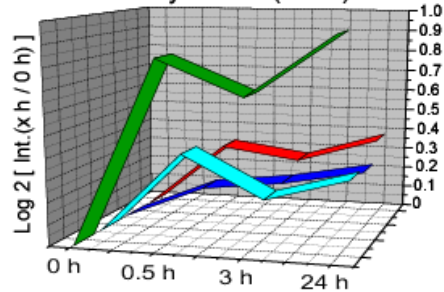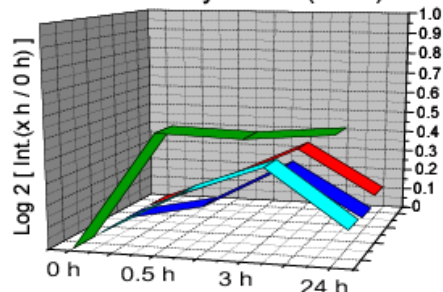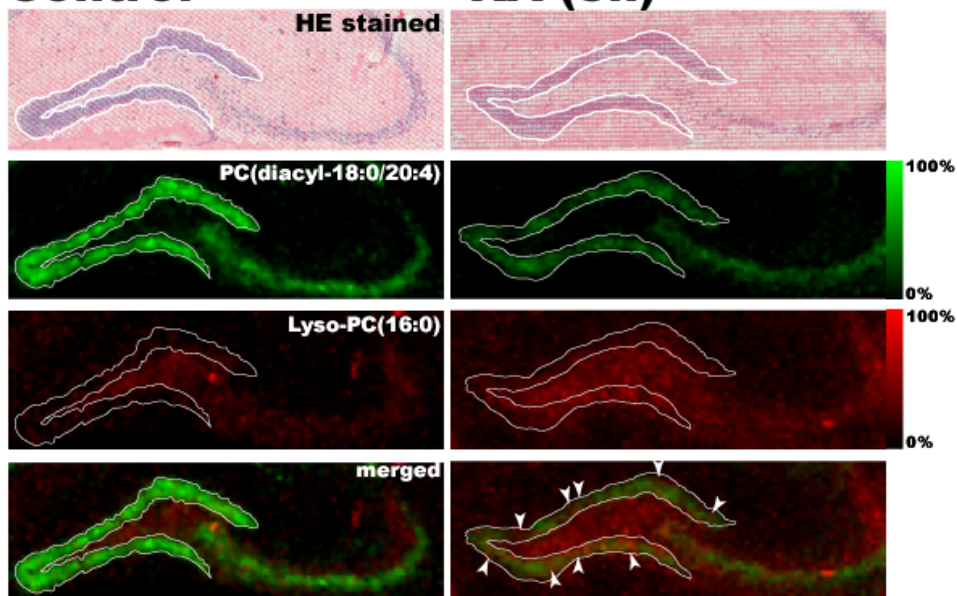
Figure 5-6: Lyso-PC expression increased in the DG-granule cell layer, which is complementary to the reduction of AA-PCs. A. Spatiotemporal

distribution of lyso-PC(16:0) and lyso-PC(18:0) in the hippocampus after kainate administration (upper panel). Imaging of lyso-PC expressions visualized their localization in the region corresponding to the mossy fiber pathway (arrowheads). The time course plot of their expression levels indicates the drastic elevation of lyso-PC levels in the granule cell layer of DG (lower). B. High-magnification images demonstrated the complemental elevation of lyso-PC(16:0) levels with the reduction of AA-PC(diacyl-16:0/20:4) in the cell layer region at 0.5 h after kainate administration.
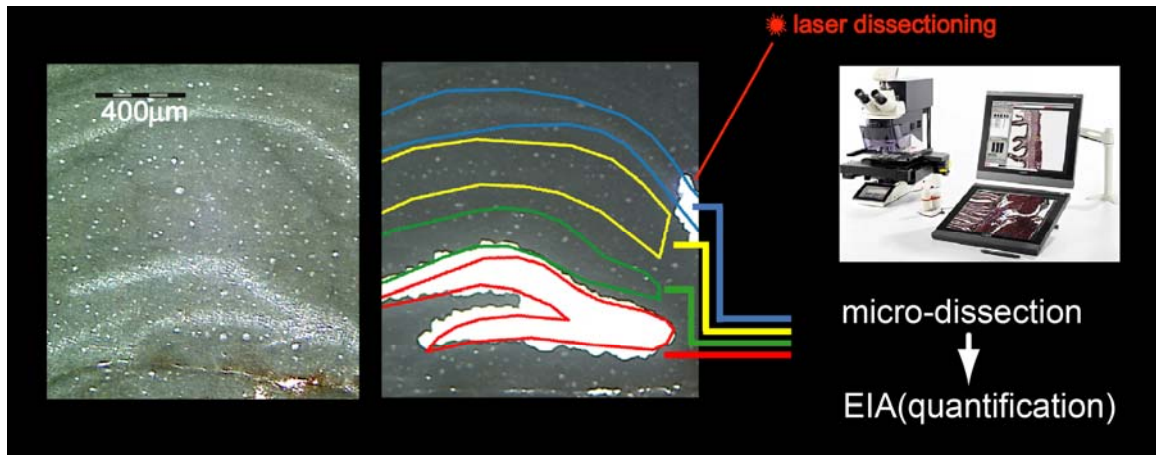
Figure 5-7: Schematic representation of LCM-EIA assay for quantification of trace prostaglnadins (PGs).
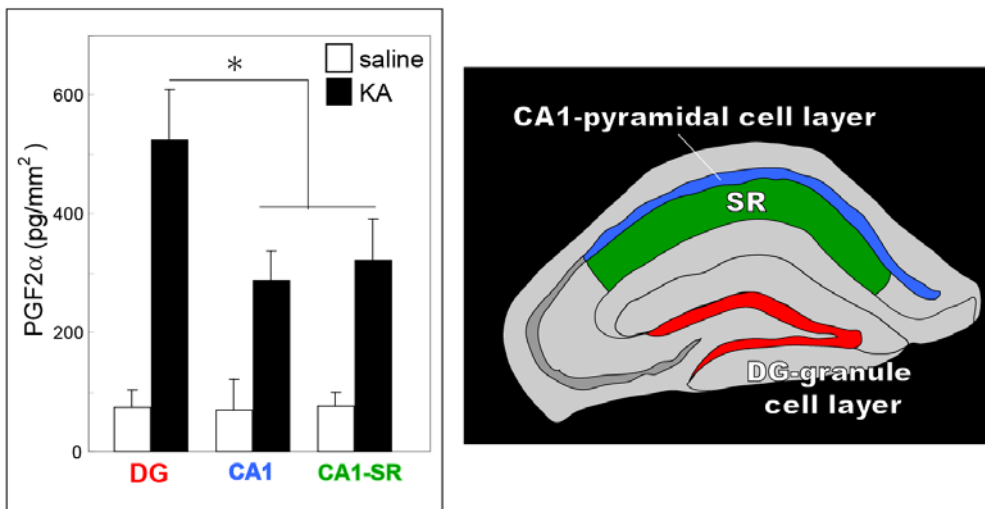
Figure 5-8: PGF2α was strongly produced in the DG-granule cell layer region in response to the KA-administration (0.5 h post dose).

Three different mouse brain sections were used, and the data were expressed as mean ± S.D. * indicate P < 0.05 and P < 0.005, respectively, Student's t-test.
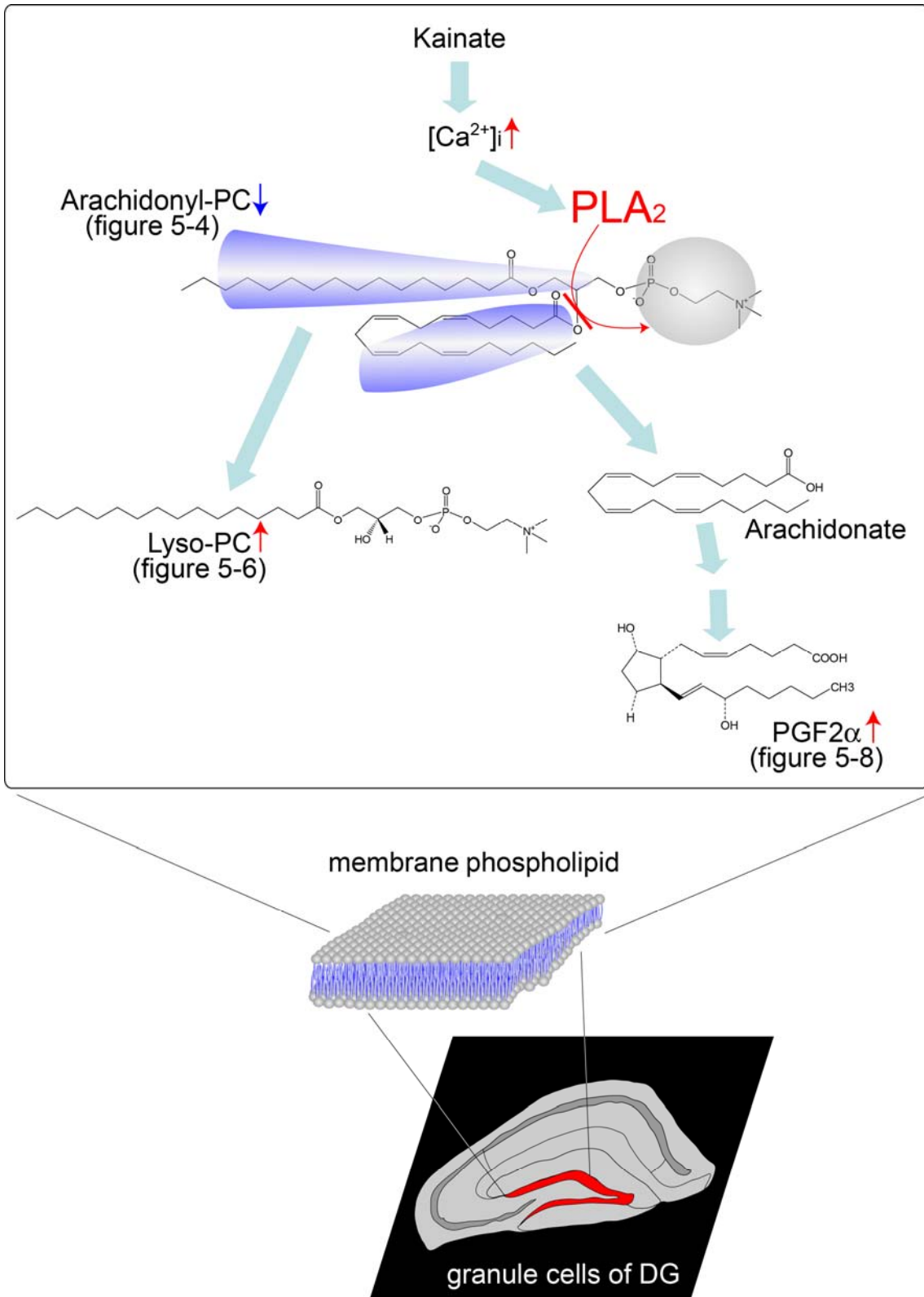
Figure 5-9: Suggested scheme of DG-granule neuron selective reaction to produce PGF2α.

Arachidonoyl-PCs were hydrolyzed presumably by PLA_2 activity, and LPC and free arachidonate were produced. The latter could be immediately converted to PGs by COX activity.

Table 5-1:

m/z	PIS-Index	molecular species	abundance ratio (control / kainate treated (0.5 h post dose))
753.6	2.88	SM(18:0)	
757.4	2.89	Isotopic peak of PC(16:0/16:0)	
784.4	2.95	Isotopic peak of PC(16:0/18:1)	
783.4	2.99	Isotopic peak of PC(16:0/18:1)	
756.4	2.99	PC(16:0/16:0)	1.02±0.03
782.4	3.04	PC(16:0/18:1)	1.03±0.07

(average PIS-index of top 15 peaks) = 4.09

Table 5-2: Molecular species of phosphatidylcholines from mouse hippocampus identified by UPLC/ESI-MS/MS.

Molecular species	Relative intensity	S.D.
PC(diacyl-16:0/18:1)	100	
PC(diacyl-16:0/16:0)	77.98	1.00
PC(diacyl-18:0/18:1)	53.19	2.16
PC(diacyl-16:0/20:4)	41.09	0.69
PC(diacyl-16:0/18:0)	34.59	0.42
PC(diacyl-16:0/22:6)	33.66	0.49
PC(diacyl-18:0/20:4)	29.69	0.24
PC(diacyl-18:1/20:4)	16.07	0.66
PC(diacyl-18:0/22:6)	15.58	0.25
PC(diacyl-18:1/18:1)	12.10	0.75
PC(diacyl-16:0/16:1)	7.07	0.65
PC(diacyl-18:1/22:6)	6.35	0.22
PC(diacyl-16:0/20:3)	4.96	0.33
PC(diacyl-18:0/18:2)	4.28	0.46
PC(diacyl-18:1/18:2)	2.37	0.26

General conclusion

The question I want to address here is whether we can understand the metabolism of body through the visualization of metabolite molecules, or not.

As mentioned, metabolites are the end products of cellular regulatory processes and can regulate various biological phenomena depending on their concentrations. Establishment of a methodology to profile the metabolite dynamics (i.e., how their expression fluctuate between time and space) comprehensively will contribute to understand how they regulate the biological phenomena, and I consider that analysis of metabolite molecular flux between time and space is a way to directly assess metabolism itself, thus will be a key technique to address my question (i.e., *in situ* metabolomics).

As a first step, I and colleagues established visualization methods for several metabolites, especially of lipids, by using IMS technology. This emerging MS-based molecular imaging technique provides distribution information regarding various biomolecules at the cell and tissue levels. In the first part of this thesis (chapter 1-3), I report my exploration of metabolite distribution in tissues with IMS, and discovered that metabolite species even with quite similar chemical structures shows distinct distribution patterns within tissues. Further, I applied IMS to a human diseased sample to identify potential biomarkers. By utilization of statistical analyses in combination with the IMS measurement, I demonstrate that it is quite effective tool for such clinical purpose (chapter 4).

The revealed heterogeneous distributions of metabolites raise a fundamental question;

do the localized small metabolites play specific functional roles to each cell-type *in vivo*? As described in chapter 5, the differential analysis between control and stimulated samples tells us about "*what*" kind of metabolic pathways are involved in the neural activity on the stimuli, and more importantly, such analysis tells us "*where*" the stimulated metabolism was occurred in the tissues. In chapter 5, I uncovered the region specific dynamics of several specific lipids on the stimulation by IMS conjunction with LCM technology. I revealed the cell-selective dynamics of bioactive-lipids induced by kainate administration, which is widely used as a model of limbic seizures, in mouse hippocampus. The results indicate the responsibility of the DG cells to the severe neuro-inflammation observed after the seizure.

 I conclude that we certainly can understand the metabolism of body through the visualization of metabolite molecules, particularly of their molecular flux. Although further study is required, I'd like to consider that the presented approaches will contribute to complete the *in situ* metabolomics.

References

1.　　Garrett, T.J*., et al.* Imaging of small molecules in tissue sections with a new intermediate-pressure MALDI linear ion trap mass spectrometer. *International Journal of Mass Spectrometry* **260**, 11 (2006).

2.　　Khatib-Shahidi, S., Andersson, M., Herman, J.L., Gillespie, T.A. & Caprioli, R.M. Direct molecular analysis of whole-body animal tissue sections by imaging MALDI mass spectrometry. *Analytical chemistry* **78**, 6448-6456 (2006).

3.　　Stoeckli, M., Staab, D., Staufenbiel, M., Wiederhold, K.H. & Signor, L. Molecular imaging of amyloid beta peptides in mouse brain sections using mass spectrometry. *Analytical biochemistry* **311**, 33-39 (2002).

4.　　Chaurand, P., Norris, J.L., Cornett, D.S., Mobley, J.A. & Caprioli, R.M. New developments in profiling and imaging of proteins from tissue sections by MALDI mass spectrometry. *Journal of proteome research* **5**, 2889-2900 (2006).

5.　　Caprioli, R.M., Farmer, T.B. & Gile, J. Molecular imaging of biological samples: localization of peptides and proteins using MALDI-TOF MS. *Analytical chemistry* **69**, 4751-4760 (1997).

6.　　Chaurand, P., Stoeckli, M. & Caprioli, R.M. Direct profiling of proteins in biological tissue sections by MALDI mass spectrometry. *Analytical chemistry* **71**, 5263-5270 (1999).

7.　　Stoeckli, M., Chaurand, P., Hallahan, D.E. & Caprioli, R.M. Imaging mass spectrometry: a new technology for the analysis of protein expression in mammalian tissues. *Nature medicine* **7**, 493-496 (2001).

8.　　Shimma, S*., et al.* Mass Imaging and Identification of Biomolecules with MALDI-QIT-TOF-Based System. *Analytical chemistry*　(2008).

9.　　Jackson, S.N., Wang, H.Y. & Woods, A.S. In situ structural characterization of phosphatidylcholines in brain tissue using MALDI-MS/MS. *Journal of the American Society for Mass Spectrometry* **16**, 2052-2056 (2005).

10.　　Jones, J.J., Borgmann, S., Wilkins, C.L. & O'Brien, R.M. Characterizing the phospholipid profiles in mammalian tissues by MALDI FTMS. *Analytical chemistry* **78**, 3062-3071 (2006).

11.　　Rujoi, M., Estrada, R. & Yappert, M.C. In situ MALDI-TOF MS regional analysis of neutral phospholipids in lens tissue. *Analytical chemistry* **76**, 1657-1663 (2004).

12.　　McLean, J.A., Ridenour, W.B. & Caprioli, R.M. Profiling and imaging of tissues by imaging ion mobility-mass spectrometry. *J Mass Spectrom* **42**, 1099-1105 (2007).

13.　　Jackson, S.N*., et al.* MALDI-ion mobility-TOFMS imaging of lipids in rat brain tissue. *J Mass Spectrom* **42**, 1093-1098 (2007).

14.　　Hayasaka, T*., et al.* Matrix-assisted laser desorption/ionization quadrupole ion trap time-of-flight (MALDI-QIT-TOF)-based imaging mass spectrometry reveals a layered distribution of phospholipid molecular species in the mouse retina. *Rapid Commun Mass Spectrom* **22**, 3415-3426 (2008).

15.　　Colliver, T.L*., et al.* Atomic and molecular imaging at the single-cell level with TOF-SIMS. *Analytical chemistry* **69**, 2225-2231 (1997).

16.　　Ostrowski, S.G., Van Bell, C.T., Winograd, N. & Ewing, A.G. Mass spectrometric imaging of highly curved membranes during Tetrahymena mating. *Science (New York, N.Y* **305**, 71-73 (2004).

17.　　Monroe, E.B., Jurchen, J.C., Lee, J., Rubakhin, S.S. & Sweedler, J.V. Vitamin E imaging and localization in the neuronal membrane. *Journal of the American Chemical Society* **127**, 12152-12153 (2005).

18.　　Touboul, D., Brunelle, A., Halgand, F., De La Porte, S. & Laprevote, O. Lipid imaging by gold cluster time-of-flight secondary ion mass spectrometry: application to Duchenne muscular dystrophy. *Journal of lipid research* **46**, 1388-1395 (2005).

19.　　Hayasaka, T*., et al.* Matrix-assisted laser desorption/ionization quadrupole ion trap time-of-flight (MALDI-QIT-TOF)-based imaging mass spectrometry reveals a layered distribution of phospholipid molecular species in the mouse retina. *Rapid Commun Mass Spectrom* **22**, 3415-3426 (2008).

20.   Jackson, S.N., Wang, H.Y. & Woods, A.S. In situ structural characterization of glycerophospholipids and sulfatides in brain tissue using MALDI-MS/MS. *Journal of the American Society for Mass Spectrometry* **18**, 17-26 (2007).

21.   Pulfer, M. & Murphy, R.C. Electrospray mass spectrometry of phospholipids. *Mass spectrometry reviews* **22**, 332-364 (2003).

22.   Murakami, M., Nakatani, Y., Atsumi, G., Inoue, K. & Kudo, I. Regulatory functions of phospholipase A2. *Critical reviews in immunology* **17**, 225-283 (1997).

23.   Piomelli, D., Astarita, G. & Rapaka, R. A neuroscientist's guide to lipidomics. *Nat Rev Neurosci* **8**, 743-754 (2007).

24.   Jackson, S.N., Wang, H.Y. & Woods, A.S. Direct profiling of lipid distribution in brain tissue using MALDI-TOFMS. *Analytical chemistry* **77**, 4523-4527 (2005).

25.   Astigarraga, E*., et al.* Profiling and Imaging of Lipids on Brain and Liver Tissue by Matrix-Assisted Laser Desorption/Ionization Mass Spectrometry Using 2-Mercaptobenzothiazole as a Matrix. *Analytical chemistry* (2008).

26.   Wang, H.Y., Jackson, S.N. & Woods, A.S. Direct MALDI-MS analysis of cardiolipin from rat organs sections. *Journal of the American Society for Mass Spectrometry* **18**, 567-577 (2007).

27.   Cornett, D.S., Frappier, S.L. & Caprioli, R.M. MALDI-FTICR imaging mass spectrometry of drugs and metabolites in tissue. *Analytical chemistry* **80**, 5648-5653 (2008).

28.   Trim, P.J*., et al.* Matrix-Assisted Laser Desorption/Ionization-Ion Mobility Separation-Mass Spectrometry Imaging of Vinblastine in Whole Body Tissue Sections. *Analytical chemistry* (2008).

29.   Atkinson, S.J., Loadman, P.M., Sutton, C., Patterson, L.H. & Clench, M.R. Examination of the distribution of the bioreductive drug AQ4N and its active metabolite AQ4 in solid tumours by imaging matrix-assisted laser desorption/ionisation mass spectrometry. *Rapid Commun Mass Spectrom* **21**, 1271-1276 (2007).

30.   Kokaji, T. Applied Biosystems'IMS. in *Mass microscopy; Imaging mass spectrometry protocol book* (ed. M. Setou) (Shpringer Japan, 2008).

31.   Sugiura, Y., Shimma, S., Konishi, Y., Yamada, M.K. & Setou, M. Imaging mass spectrometry technology and application on ganglioside study; visualization of age-dependent accumulation of C20-ganglioside molecular species in the mouse hippocampus. *PLoS ONE* **3**, e3232 (2008).

32.   Chen, Y*., et al.* Imaging MALDI mass spectrometry using an oscillating capillary nebulizer matrix coating system and its application to analysis of lipids in brain from a mouse model of Tay-Sachs/Sandhoff disease. *Analytical chemistry* **80**, 2780-2788 (2008).

33.   Ageta, H*., et al.* Layer-specific sulfatide localization in rat hippocampus middle molecular layer is revealed by nanoparticle-assisted laser desorption/ionization imaging mass spectrometry. *Medical Molecular Morphology* **in press** (2008).

34.   Cha, S. & Yeung, E.S. Colloidal graphite-assisted laser desorption/ionization mass spectrometry and MSn of small molecules. 1. Imaging of cerebrosides directly from rat brain tissue. *Analytical chemistry* **79**, 2373-2385 (2007).

35.   Taira, S*., et al.* Nanoparticle-assisted laser desorption/ionization based mass imaging with cellular resolution. *Analytical chemistry* **80**, 4761-4766 (2008).

36.   Altelaar, A.F*., et al.* Gold-enhanced biomolecular surface imaging of cells and tissue by SIMS and MALDI mass spectrometry. *Analytical chemistry* **78**, 734-742 (2006).

37.   Zhang, H., Cha, S. & Yeung, E.S. Colloidal graphite-assisted laser desorption/ionization MS and MS(n) of small molecules. 2. Direct profiling and MS imaging of small metabolites from fruits. *Analytical chemistry* **79**, 6575-6584 (2007).

38.   Li, Y., Shrestha, B. & Vertes, A. Atmospheric pressure infrared MALDI imaging mass spectrometry for plant metabolomics. *Analytical chemistry* **80**, 407-420 (2008).

39.   Shimma, S. & Setou, M. Mass Microscopy to Reveal Distinct Localization of Heme B (m/z 616) in Colon Cancer Liver Metastasis. *J. Mass Spectrom. Soc. Jpn.* **55** (2007).

40.   Mazel, V*., et al.* Identification of ritual blood in African artifacts using TOF-SIMS and synchrotron radiation microspectroscopies. *Analytical chemistry* **79**, 9253-9260 (2007).

41.   Takamori, S*., et al.* Molecular anatomy of a trafficking organelle. *Cell* **127**, 831-846

(2006).

42.   Rohrbough, J. & Broadie, K. Lipid regulation of the synaptic vesicle cycle. *Nature reviews* **6**, 139-150 (2005).

43.   Kim, D. Fatty acid-sensitive two-pore domain K+ channels. *Trends in pharmacological sciences* **24**, 648-654 (2003).

44.   Miller, B., Sarantis, M., Traynelis, S.F. & Attwell, D. Potentiation of NMDA receptor currents by arachidonic acid. *Nature* **355**, 722-725 (1992).

45.   Jacobson, K., Mouritsen, O.G. & Anderson, R.G. Lipid rafts: at a crossroad between cell biology and physics. *Nature cell biology* **9**, 7-14 (2007).

46.   Allen, J.A., Halverson-Tamboli, R.A. & Rasenick, M.M. Lipid raft microdomains and neurotransmitter signalling. *Nature reviews* **8**, 128-140 (2007).

47.   Yamashita, A., Sugiura, T. & Waku, K. Acyltransferases and transacylases involved in fatty acid remodeling of phospholipids and metabolism of bioactive lipids in mammalian cells. *Journal of biochemistry* **122**, 1-16 (1997).

48.   Williams, J.H., Errington, M.L., Lynch, M.A. & Bliss, T.V. Arachidonic acid induces a long-term activity-dependent enhancement of synaptic transmission in the hippocampus. *Nature* **341**, 739-742 (1989).

49.   Dinh, T.P.*, et al.* Brain monoglyceride lipase participating in endocannabinoid inactivation. *Proceedings of the National Academy of Sciences of the United States of America* **99**, 10819-10824 (2002).

50.   Han, X. & Gross, R.W. Global analyses of cellular lipidomes directly from crude extracts of biological samples by ESI mass spectrometry: a bridge to lipidomics. *Journal of lipid research* **44**, 1071-1079 (2003).

51.   Yoshikawa, K., Kita, Y., Kishimoto, K. & Shimizu, T. Profiling of eicosanoid production in the rat hippocampus during kainic acid-induced seizure: dual phase regulation and differential involvement of COX-1 and COX-2. *The Journal of biological chemistry* **281**, 14663-14669 (2006).

52.   Guan, X.L.*, et al.* Non-targeted profiling of lipids during kainate-induced neuronal injury. *Faseb J* **20**, 1152-1161 (2006).

53.   Ikegami, K.*, et al.* Loss of alpha-tubulin polyglutamylation in ROSA22 mice is associated with abnormal targeting of KIF1A and modulated synaptic function. *Proceedings of the National Academy of Sciences of the United States of America* **104**, 3213-3218 (2007).

54.   Sweedler, J.V.*, et al.* Identification and characterization of the feeding circuit-activating peptides, a novel neuropeptide family of aplysia. *J Neurosci* **22**, 7797-7808 (2002).

55.   Hosokawa, N., Sugiura, Y. & Setou, M. Spectrum Normalization Method Using an External Standard in Mass Spectrometric Imaging. *J. Mass Spectrom. Soc. Jpn.* **Vol. 56**, 5 (2008).

56.   Yanagisawa, K.*, et al.* Proteomic patterns of tumour subsets in non-small-cell lung cancer. *Lancet* **362**, 433-439 (2003).

57.   Yao, I., Sugiura, Y., Matsumoto, M. & Setou, M. In situ proteomics with imaging mass spectrometry and principal
component analyses in the Scrapper-knockout mouse brain. *PROTEOMICS* **in press** (2008).

58.   Altelaar, A.F., Luxembourg, S.L., McDonnell, L.A., Piersma, S.R. & Heeren, R.M. Imaging mass spectrometry at cellular length scales. *Nature protocols* **2**, 1185-1196 (2007).

59.   Umemura, A., Mabe, H., Nagai, H. & Sugino, F. Action of phospholipases A2 and C on free fatty acid release during complete ischemia in rat neocortex. Effect of phospholipase C inhibitor and N-methyl-D-aspartate antagonist. *Journal of neurosurgery* **76**, 648-651 (1992).

60.   Rehncrona, S., Westerberg, E., Akesson, B. & Siesjo, B.K. Brain cortical fatty acids and phospholipids during and following complete and severe incomplete ischemia. *Journal of neurochemistry* **38**, 84-93 (1982).

61.   Sugiura, Y., Shimma, S. & Setou, M. Thin Sectioning Improves the Peak Intensity and Signal-to-Noise Ratio in Direct Tissue Mass Spectrometry *J. Mass Spectrom. Soc. Jpn.* **Vol. 54**, 4 (2006).

62.   Schwartz, S.A., Reyzer, M.L. & Caprioli, R.M. Direct tissue analysis using matrix-assisted laser desorption/ionization mass spectrometry: practical aspects of sample preparation. *J Mass Spectrom* **38**, 699-708 (2003).

63.   Han, X. & Gross, R.W. Quantitative analysis and molecular species fingerprinting of triacylglyceride molecular species directly from lipid extracts of biological samples by electrospray ionization tandem mass spectrometry. *Analytical biochemistry* **295**, 88-100 (2001).

64.   Hsu, F.F. & Turk, J. Structural determination of glycosphingolipids as lithiated adducts by electrospray ionization mass spectrometry using low-energy collisional-activated dissociation on a triple stage quadrupole instrument. *Journal of the American Society for Mass Spectrometry* **12**, 61-79 (2001).

65.   Sugiura, Y., Shimma, S. & Setou, M. Two-step matrix application technique to improve ionization efficiency for matrix-assisted laser desorption/ionization in imaging mass spectrometry. *Analytical chemistry* **78**, 8227-8235 (2006).

66.   Mock, K.K., Sutton, C.W. & Cottrell, J.S. Sample immobilization protocols for matrix-assisted laser-desorption mass spectrometry. *Rapid Commun Mass Spectrom* **6**, 233-238 (1992).

67.   Taguchi, R*., et al.* Focused lipidomics by tandem mass spectrometry. *Journal of chromatography* **823**, 26-36 (2005).

68.   Stubiger, G., Pittenauer, E. & Allmaier, G. MALDI seamless postsource decay fragment ion analysis of sodiated and lithiated phospholipids. *Analytical chemistry* **80**, 1664-1678 (2008).

69.   Touboul, D*., et al.* Changes of phospholipid composition within the dystrophic muscle by matrix-assisted laser desorption/ionization mass spectrometry and mass spectrometry imaging. *European journal of mass spectrometry (Chichester, England)* **10**, 657-664 (2004).

70.   Houjou, T., Yamatani, K., Imagawa, M., Shimizu, T. & Taguchi, R. A shotgun tandem mass spectrometric analysis of phospholipids with normal-phase and/or reverse-phase liquid chromatography/electrospray ionization mass spectrometry. *Rapid Commun Mass Spectrom* **19**, 654-666 (2005).

71.   Sinclair, A.J. & Crawford, M.A. The accumulation of arachidonate and docosahexaenoate in the developing rat brain. *Journal of neurochemistry* **19**, 1753-1758 (1972).

72.   Svennerholm, L. Distribution and fatty acid composition of phosphoglycerides in normal human brain. *Journal of lipid research* **9**, 570-579 (1968).

73.   Svennerholm, L. & Vanier, M.T. The distribution of lipids in the human nervous system. 3. Fatty acid composition of phosphoglycerides of human foetal and infant brain. *Brain research* **50**, 341-351 (1973).

74.   Martinez, M. & Mougan, I. Fatty acid composition of human brain phospholipids during normal development. *Journal of neurochemistry* **71**, 2528-2533 (1998).

75.   McCombie, G., Staab, D., Stoeckli, M. & Knochenmuss, R. Spatial and spectral correlations in MALDI mass spectrometry images by clustering and multivariate analysis. *Analytical chemistry* **77**, 6118-6124 (2005).

76.   Norris, J.L*., et al.* Processing MALDI mass spectra to improve mass spectral direct tissue analysis *International Journal of Mass Spectrometry* **260**, 212-221 (2006).

77.   Hitzemann, R.J. & Johnson, D.A. Developmental changes in synaptic membrane lipid composition and fluidity. *Neurochemical research* **8**, 121-131 (1983).

78.   Zerouga, M., Jenski, L.J. & Stillwell, W. Comparison of phosphatidylcholines containing one or two docosahexaenoic acyl chains on properties of phospholipid monolayers and bilayers. *Biochimica et biophysica acta* **1236**, 266-272 (1995).

79.   Salem, N., Jr., Litman, B., Kim, H.Y. & Gawrisch, K. Mechanisms of action of docosahexaenoic acid in the nervous system. *Lipids* **36**, 945-959 (2001).

80.   Kim, H.Y. Novel metabolism of docosahexaenoic acid in neural cells. *The Journal of biological chemistry* **282**, 18661-18665 (2007).

81.   Stubbs, C.D. & Smith, A.D. The modification of mammalian membrane

polyunsaturated fatty acid composition in relation to membrane fluidity and function. *Biochimica et biophysica acta* **779**, 89-137 (1984).

82.   Surette, M.E. & Chilton, F.H. The distribution and metabolism of arachidonate-containing phospholipids in cellular nuclei. *The Biochemical journal* **330 (Pt 2)**, 915-921 (1998).

83.   Hishikawa, D*., et al.* Discovery of a lysophospholipid acyltransferase family essential for membrane asymmetry and diversity. *Proceedings of the National Academy of Sciences of the United States of America* **105**, 2830-2835 (2008).

84.   van Echten, G. & Sandhoff, K. Ganglioside metabolism. Enzymology, Topology, and regulation. *The Journal of biological chemistry* **268**, 5341-5344 (1993).

85.   Rahmann, H. Brain gangliosides and memory formation. *Behavioural brain research* **66**, 105-116 (1995).

86.   Prinetti, A., Iwabuchi, K. & Hakomori, S. Glycosphingolipid-enriched signaling domain in mouse neuroblastoma Neuro2a cells. Mechanism of ganglioside-dependent neuritogenesis. *The Journal of biological chemistry* **274**, 20916-20924 (1999).

87.   Ramirez, O.A., Gomez, R.A. & Carrer, H.F. Gangliosides improve synaptic transmission in dentate gyrus of hippocampal rat slices. *Brain research* **506**, 291-293 (1990).

88.   Kotani, M., Terashima, T. & Tai, T. Developmental changes of ganglioside expressions in postnatal rat cerebellar cortex. *Brain research* **700**, 40-58 (1995).

89.   Yu, R.K., Macala, L.J., Taki, T., Weinfield, H.M. & Yu, F.S. Developmental changes in ganglioside composition and synthesis in embryonic rat brain. *Journal of neurochemistry* **50**, 1825-1829 (1988).

90.   Iwabuchi, K., Yamamura, S., Prinetti, A., Handa, K. & Hakomori, S. GM3-enriched microdomain involved in cell adhesion and signal transduction through carbohydrate-carbohydrate interaction in mouse melanoma B16 cells. *The Journal of biological chemistry* **273**, 9130-9138 (1998).

91.   Iwabuchi, K., Handa, K. & Hakomori, S. Separation of "glycosphingolipid signaling domain" from caveolin-containing membrane fraction in mouse melanoma B16 cells and its role in cell adhesion coupled with signaling. *The Journal of biological chemistry* **273**, 33766-33773 (1998).

92.   Kasahara, K., Watanabe, Y., Yamamoto, T. & Sanai, Y. Association of Src family tyrosine kinase Lyn with ganglioside GD3 in rat brain. Possible regulation of Lyn by glycosphingolipid in caveolae-like domains. *The Journal of biological chemistry* **272**, 29947-29953 (1997).

93.   Kasahara, K*., et al.* Involvement of gangliosides in glycosylphosphatidylinositol-anchored neuronal cell adhesion molecule TAG-1 signaling in lipid rafts. *The Journal of biological chemistry* **275**, 34701-34709 (2000).

94.   Sonnino, S. & Chigorno, V. Ganglioside molecular species containing C18- and C20-sphingosine in mammalian nervous tissues and neuronal cell cultures. *Biochimica et biophysica acta* **1469**, 63-77 (2000).

95.   Sambasivarao, K. & McCluer, R.H. Lipid Components of Gangliosides. *Journal of lipid research* **15**, 103-108 (1964).

96.   Schwarz, H.P., Kostyk, I., Marmolejo, A. & Sarappa, C. Long-chain bases of brain and spinal cord of rabbits. *Journal of neurochemistry* **14**, 91-97 (1967).

97.   Jungalwala, F.B., Hayssen, V., Pasquini, J.M. & McCluer, R.H. Separation of molecular species of sphingomyelin by reversed-phase high-performance liquid chromatography. *Journal of lipid research* **20**, 579-587 (1979).

98.   Palestini, P., Sonnino, S. & Tettamanti, G. Lack of the ganglioside molecular species containing the C20-long-chain bases in human, rat, mouse, rabbit, cat, dog, and chicken brains during prenatal life. *Journal of neurochemistry* **56**, 2048-2050 (1991).

99.   Palestini, P., Masserini, M., Sonnino, S., Giuliani, A. & Tettamanti, G. Changes in the ceramide composition of rat forebrain gangliosides with age. *Journal of neurochemistry* **54**, 230-235 (1990).

100.   Mansson, J.E., Vanier, M.T. & Svennerholm, L. Changes in the fatty acid and sphingosine composition of the major gangliosides of human brain with age. *Journal of*

neurochemistry **30**, 273-275 (1978).

101.   Masserini, M*., et al.* Cyclic AMP accumulation in HeLa cells induced by cholera toxin. Involvement of the ceramide moiety of GM1 ganglioside. *The Biochemical journal* **271**, 107-111 (1990).

102.   Kotani, M., Kawashima, I., Ozawa, H., Terashima, T. & Tai, T. Differential distribution of major gangliosides in rat central nervous system detected by specific monoclonal antibodies. *Glycobiology* **3**, 137-146 (1993).

103.   Chaurand, P*., et al.* Monitoring mouse prostate development by profiling and imaging mass spectrometry. *Mol Cell Proteomics* **7**, 411-423 (2008).

104.   Rubakhin, S.S., Hatcher, N.G., Monroe, E.B., Heien, M.L. & Sweedler, J.V. Mass spectrometric imaging of the nervous system. *Current pharmaceutical design* **13**, 3325-3334 (2007).

105.   Shimma, S*., et al.* Mass Imaging and Identification of Biomolecules with MALDI-QIT-TOF-Based System. *Analytical chemistry* **80**, 878-885 (2008).

106.   Shimma, S*., et al.* MALDI-based imaging mass spectrometry revealed abnormal distribution of phospholipids in colon cancer liver metastasis. *Journal of chromatography* **855**, 98-103 (2007).

107.   Sugiura, Y., Shimma, S. & Setou, M. Thin Sectioning Improves the Peak Intensity and Signal-to-Noise Ratio in Direct Tissue Mass Spectrometry. *J. Mass Spectrom. Soc. Jpn.* **54**, 4 (2006).

108.   Sugiyama, E., Hara, A., Uemura, K. & Taketomi, T. Application of matrix-assisted laser desorption ionization time-of-flight mass spectrometry with delayed ion extraction to ganglioside analyses. *Glycobiology* **7**, 719-724 (1997).

109.   Handa, S. & Nakamura, K. Modification of sialic acid carboxyl group of ganglioside. *Journal of biochemistry* **95**, 1323-1329 (1984).

110.   Sekiya, S., Wada, Y. & Tanaka, K. Derivatization for stabilizing sialic acids in MALDI-MS. *Analytical chemistry* **77**, 4962-4968 (2005).

111.   Harvey, D.J. Matrix-assisted laser desorption/ionisation mass spectrometry of oligosaccharides and glycoconjugates. *Journal of chromatography* **720**, 429-446 (1996).

112.   Powell, A.K. & Harvey, D.J. Stabilization of sialic acids in N-linked oligosaccharides and gangliosides for analysis by positive ion matrix-assisted laser desorption/ionization mass spectrometry. *Rapid Commun Mass Spectrom* **10**, 1027-1032 (1996).

113.   van Groen, T., Miettinen, P. & Kadish, I. The entorhinal cortex of the mouse: organization of the projection to the hippocampal formation. *Hippocampus* **13**, 133-149 (2003).

114.   Calderon, R.O., Attema, B. & DeVries, G.H. Lipid composition of neuronal cell bodies and neurites from cultured dorsal root ganglia. *Journal of neurochemistry* **64**, 424-429 (1995).

115.   Hjorth-Simonsen, A. Projection of the lateral part of the entorhinal area to the hippocampus and fascia dentata. *The Journal of comparative neurology* **146**, 219-232 (1972).

116.   Masco, D. & Seifert, W. Gangliosides in lesion-induced synaptogenesis: studies in the hippocampus of the rat brain. *Brain research* **514**, 84-92 (1990).

117.   Ramirez, J.J., MacDonald, K., Manibo, J., Payne, J. & Tuite, C. GM1-Ganglioside Suppresses Septodentate Sprouting and Enhances Recovery from Entorhinal Cortex Lesions on DRL Perfomance and Locomotor Behavior in Rats. *Restorative neurology and neuroscience* **12**, 203-211 (1998).

118.   Glasier, M.M., Sutton, R.L. & Stein, D.G. Effects of unilateral entorhinal cortex lesion and ganglioside GM1 treatment on performance in a novel water maze task. *Neurobiology of learning and memory* **64**, 203-214 (1995).

119.   Valsecchi, M., Palestini, P., Chigorno, V., Sonnino, S. & Tettamanti, G. Changes in the ganglioside long-chain base composition of rat cerebellar granule cells during differentiation and aging in culture. *Journal of neurochemistry* **60**, 193-196 (1993).

120.   Gomez-Isla, T*., et al.* Profound loss of layer II entorhinal cortex neurons occurs in very mild Alzheimer's disease. *J Neurosci* **16**, 4491-4500 (1996).

121.   Sonnino, S. & Chigorno, V. Ganglioside molecular species containing C18-and C20-sphingosine in mammalian nervous tissues and neuronal cell cultures. 63-77 (Elsevier, 2000).

122.   Sugiura, Y., Shimma, S. & Setou, M. Two-step matrix application technique to improve ionization efficiency for matrix-assisted laser desorption/ionization in imaging mass spectrometry. 16.

123.   Ajiki, W., Tsukuma, H. & Oshima, A. Survival rates of childhood cancer patients in Osaka, Japan. 50 (FPCR, 2004).

124.   Harkins, L., *et al.* Specific localisation of human cytomegalovirus nucleic acids and proteins in human colorectal cancer. 1557-1563 (Elsevier, 2002).

125.   Newell, G.R., Spitz, M.R. & Sider, J.G. Cancer and age. 3 (1989).

126.   Kuriki, K., *et al.* Risk of colorectal cancer is linked to erythrocyte compositions of fatty acids as biomarkers for dietary intakes of fish, fat, and fatty acids. 1791 (AACR, 2006).

127.   Huerta, S., *et al.* Gene expression profile of metastatic colon cancer cells resistant to cisplatin-induced apoptosis. (2003).

128.   Sugiura, Y., *et al.* Visualization of the cell-selective distribution of PUFA-containing phosphatidylcholines in mouse brain by imaging mass spectrometry. *Journal of lipid research* **50**, 1776-1788 (2009).

129.   Demirev, P.A., *et al.* Detection of malaria parasites in blood by laser desorption mass spectrometry. 3262-3266 (2002).

130.   Rael, L.T., Ayala-Fierro, F., Bar-Or, R., Carter, D.E. & Barber, D.S. Interaction of Arsine with Hemoglobin in Arsine-Induced Hemolysis. 142 (Soc Toxicology, 2006).

131.   Dueck, D.A., *et al.* The modulation of choline phosphoglyceride metabolism in human colon cancer. 97-103 (Springer, 1996).

132.   Dobrzy ska, I., Szachowicz-Petelska, B., Sulkowski, S. & Figaszewski, Z. Changes in electric charge and phospholipids composition in human colorectal cancer cells. 113-119 (Springer, 2005).

133.   Brasitus, T.A., Dudeja, P.K. & Dahiya, R. Premalignant alterations in the lipid composition and fluidity of colonic brush border membranes of rats administered 1, 2 dimethylhydrazine. 831 (American Society for Clinical Investigation, 1986).

134.   Stark, D.D., Wittenberg, J., Butch, R.J. & Ferrucci, J.T. Hepatic metastases: randomized, controlled comparison of detection with MR imaging and CT. 399 (Radiological Society of North America, 1987).

135.   Stark, D.D., *et al.* Superparamagnetic iron oxide: clinical application as a contrast agent for MR imaging of the liver. 297 (Radiological Society of North America, 1988).

136.   McDonnell, L.A., *et al.* Subcellular imaging mass spectrometry of brain tissue. *J Mass Spectrom* **40**, 160-168 (2005).

137.   Andersson, M., Groseclose, M.R., Deutch, A.Y. & Caprioli, R.M. Imaging mass spectrometry of proteins and peptides: 3D volume reconstruction. *Nature methods* **5**, 101-108 (2008).

138.   Eisen, M.B., Spellman, P.T., Brown, P.O. & Botstein, D. Cluster analysis and display of genome-wide expression patterns. *Proceedings of the National Academy of Sciences of the United States of America* **95**, 14863-14868 (1998).

139.   Norris, J.L., *et al.* Processing MALDI Mass Spectra to Improve Mass Spectral Direct Tissue Analysis. *Int J Mass Spectrom* **260**, 212-221 (2007).

140.   Wagner, M., Naik, D. & Pothen, A. Protocols for disease classification from mass spectrometry data. *Proteomics* **3**, 1692-1698 (2003).

141.   Baggerly, K.A., *et al.* A comprehensive approach to the analysis of matrix-assisted laser desorption/ionization-time of flight proteomics spectra from serum samples. *Proteomics* **3**, 1667-1672 (2003).

142.   Ben-Ari, Y. Limbic seizure and brain damage produced by kainic acid: mechanisms and relevance to human temporal lobe epilepsy. *Neuroscience* **14**, 375-403 (1985).

143.   Ben-Ari, Y. & Cossart, R. Kainate, a double agent that generates seizures: two decades of progress. 580-587 (Elsevier, 2000).

144.   Lothman, E.W. & Collins, R.C. Kainic acid induced limbic seizures: metabolic,

behavioral, electroencephalographic and neuropathological correlates. *Brain research* **218**, 299-318 (1981).

145.   Nedivi, E., Hevroni, D., Naot, D., Israeli, D. & Citri, Y. Numerous candidate plasticity-related genes revealed by differential cDNA cloning. (Nature Publishing Group, 1993).

146.   Carrie, I., Clement, M., de Javel, D., Frances, H. & Bourre, J.M. Specific phospholipid fatty acid composition of brain regions in mice. Effects of n-3 polyunsaturated fatty acid deficiency and phospholipid supplementation. *Journal of lipid research* **41**, 465-472 (2000).

147.   Farooqui, A.A., Yi Ong, W., Lu, X.R., Halliwell, B. & Horrocks, L.A. Neurochemical consequences of kainate-induced toxicity in brain: involvement of arachidonic acid release and prevention of toxicity by phospholipase A(2) inhibitors. *Brain Res Brain Res Rev* **38**, 61-78 (2001).

148.   Kamiya, H. Kainate receptor-dependent presynaptic modulation and plasticity. *Neuroscience research* **42**, 1-6 (2002).

149.   Mizota, A., Sato, E., Taniai, M., Adachi-Usami, E. & Nishikawa, M. Protective effects of dietary docosahexaenoic acid against kainate-induced retinal degeneration in rats. *Investigative ophthalmology & visual science* **42**, 216-221 (2001).

150.   Schwab, J.M., Chiang, N., Arita, M. & Serhan, C.N. Resolvin E1 and protectin D1 activate inflammation-resolution programmes. *Nature* **447**, 869-874 (2007).

151.   Krause, E., Wenschuh, H. & Jungblut, P.R. The dominance of arginine-containing peptides in MALDI-derived tryptic mass fingerprints of proteins. *Analytical chemistry* **71**, 4160-4165 (1999).

152.   Gharahdaghi, F., Kirchner, M., Fernandez, J. & Mische, S.M. Peptide-mass profiles of polyvinylidene difluoride-bound proteins by matrix-assisted laser desorption/ionization time-of-flight mass spectrometry in the presence of nonionic detergents. *Analytical biochemistry* **233**, 94-99 (1996).

153.   Annesley, T.M. Ion suppression in mass spectrometry. *Clinical chemistry* **49**, 1041-1044 (2003).

154.   Farooqui, A.A. & Horrocks, L.A. Excitotoxicity and neurological disorders: involvement of membrane phospholipids. *International review of neurobiology* **36**, 267-323 (1994).

155.   Schauwecker, P.E. & Steward, O. Genetic determinants of susceptibility to excitotoxic cell death: implications for gene targeting approaches. *Proceedings of the National Academy of Sciences of the United States of America* **94**, 4103-4108 (1997).
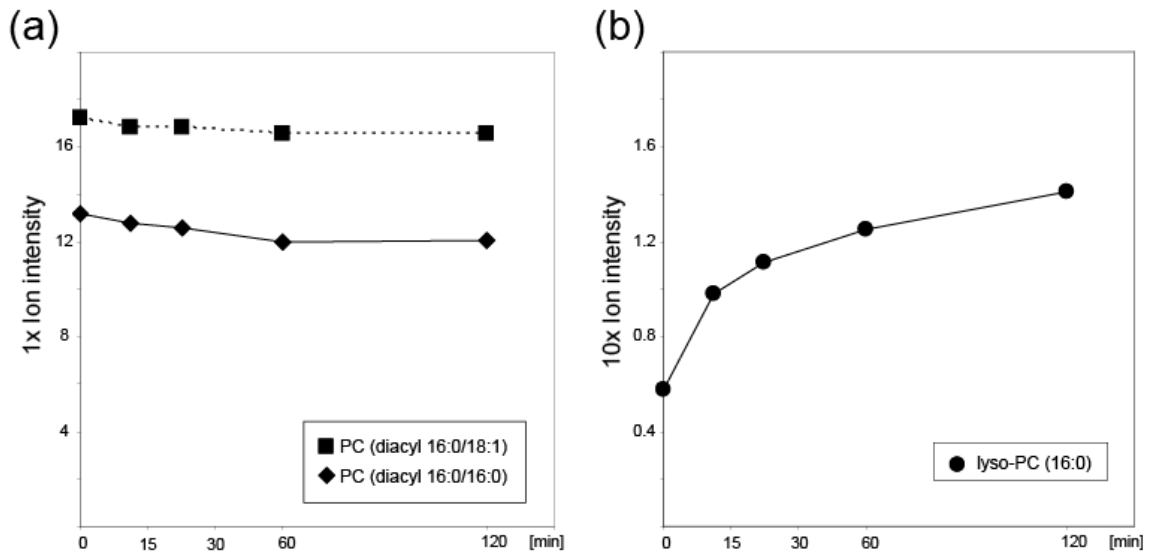
156.   Shimma, S.*, et al.* MALDI-based imaging mass spectrometry revealed abnormal distribution of phospholipids in colon cancer liver metastasis. *J Chromatogr B Analyt Technol Biomed Life Sci*   (2007).

Supplemental Figures

Figure S1.

Figure S1. Post-mortem degradation of PCs and increase in lyso-PCs.
  An IMS of series was performed of mouse brains extracted at different elapsed times from sacrifice (within a minute, and 15, 30, 60, and 120 min after sacrifice). After IMS, the ion intensities of the PCs were averaged over the entire section. As post-mortem events, degradation of PCs and an increase in lyso-PCs were observed within 15 minutes, presumably caused by stimulation activity of PLAs under ischemic conditions (Rehncrona et al., 1982; Umemura et al., 1992). In this study, mouse brains were extracted within a minute (typically in 40 seconds) after sacrifice.
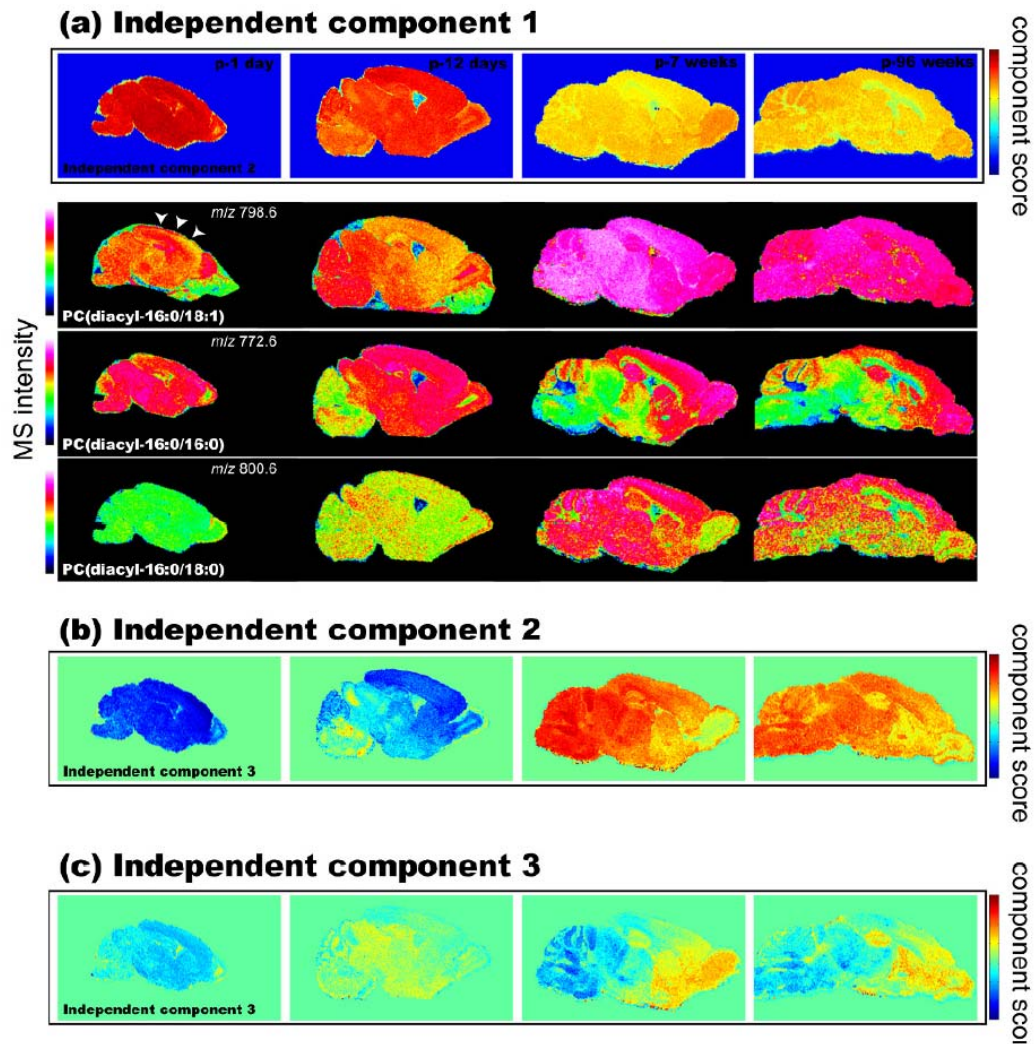
Figure S2.
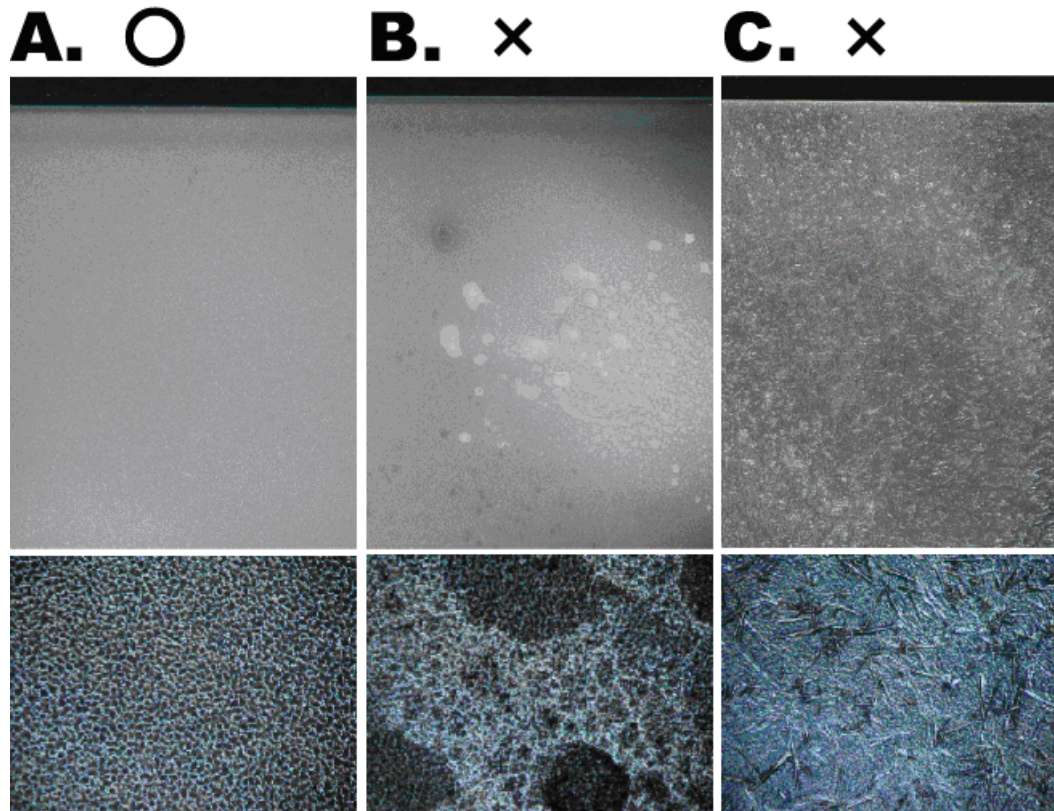
Figure S2. Tips for spray-coating of the matrix solution by air-brush.
a, A properly handled spray-coating step created a uniform matrix crystal layer, and awareness of certain technical points leads to a successful coating step.
b, Too small a distance between the air-brush and the tissues (< 10 cm) often creates large droplets of matrix solution and results in inhomogeneous crystals.
*c*, Humidity is also an important factor. Room humidity was held under 25% at room temperature (25 °C). High humidity tends to cause formation of needle-like crystals (> 80%, at room temperature). The upper panel shows stereoscopic microscope images, and the lower panel shows phase-contrast microscopic images of the matrix layer formed on the glass slides.

Figure S3.

Figure S3. IMS-ICA of the developmental mouse brains revealed dynamic changes in PC distribution. ICA was performed along with PCA on the four developing mouse brain sections to extract general trends in PC distributions during development. Three trends emerged. *a*, Component 1 represents an accumulation of PCs with saturated fatty acids (SFA) and MUFAs. *b*, Component 2 represents a reduction in PCs with short-chain fatty acids and an accumulation of myelin-constituted PCs. *c*, Component 3 represents the accumulation of two abundant AA-PCs in the hippocampus, cerebral cortex, corpus striatum, and granule cell layer of the cerebellum. ICA components 2 and 3 correspond to PCA components 2 and 3, respectively. In panel (*a*), the upper row illustrates the principal component score for each pixel, and the lower rows show the results of individual visualizations of PCs that had large loading factors for each independent component. Also see Table 2-4.
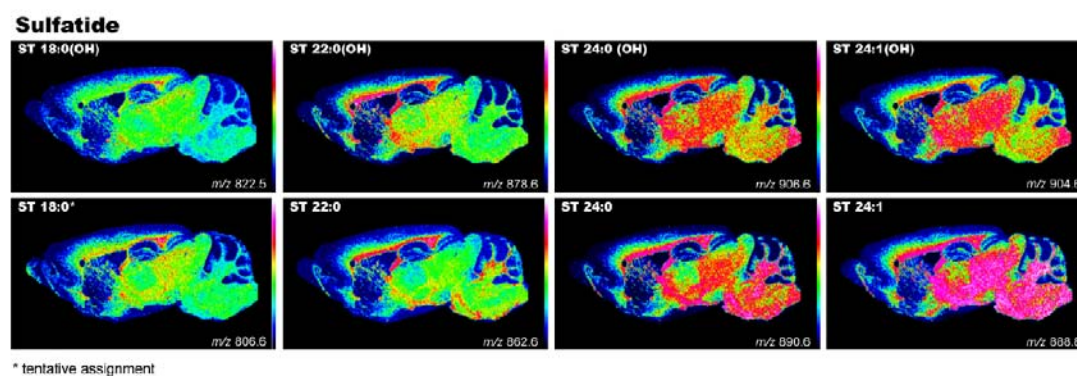
130
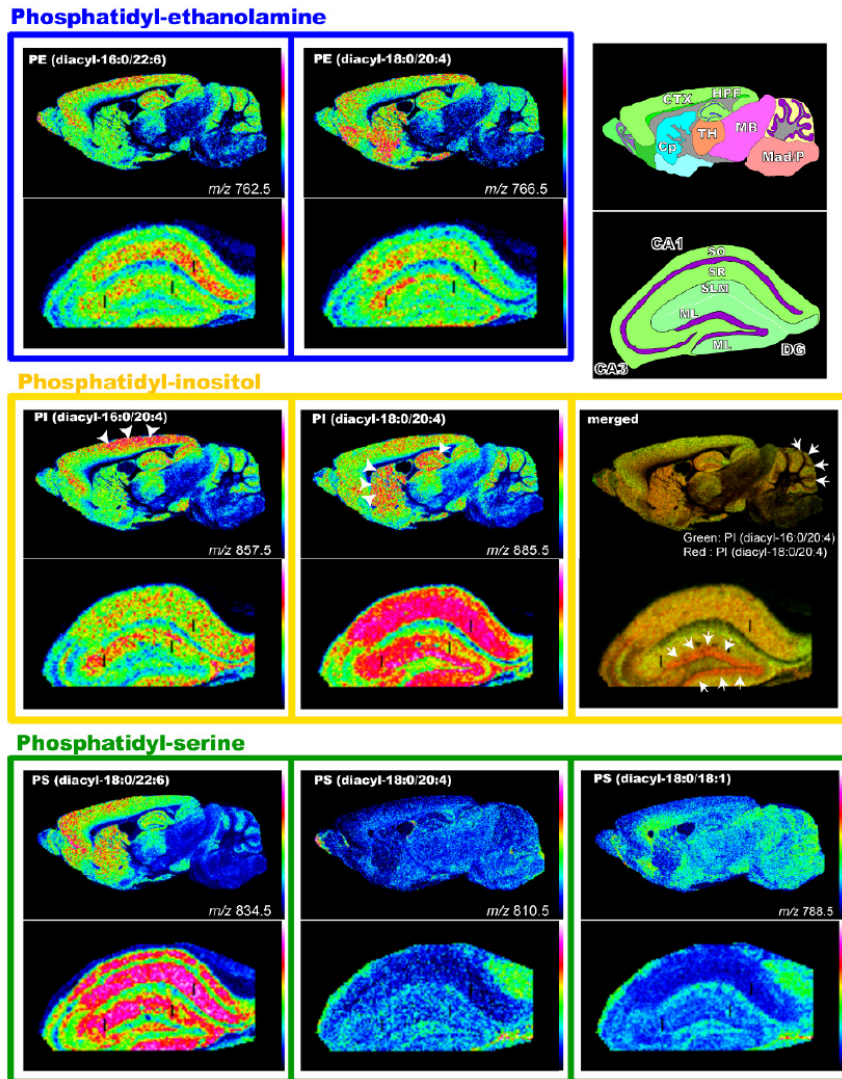
Figure S4.

Figure S4. Differential distributions of PE, PS, and PI molecular species in the mouse brain sections. In negative ion detection mode, IMS of a brain section simultaneously revealed heterogeneous distributions of PE, PS and PI molecular species. A schema of the mouse brain sagittal section and hippocampus, and ion images for PEs, PSs, and PIs are shown. Molecular assignment was performed according to (Jackson et al., 2007). Among them, two abundant molecular species of PI, PI (diacyl-16:0/20:4) and PI (diacyl-18:0/20:4), showed a characteristic distribution. While PI (diacyl-16:0/20:4) localized in the CP and HPF, PI (diacyl-18:0/20:4) was strongly contained in the CTX (arrowheads). In greater detail, PI (diacyl-18:0/20:4) was enriched in the granule cell layer of HPF and the granule layer of the cerebellum (arrows). CBX, cerebellar cortex; CP, corpus striatum; CTX, cerebral cortex; HPF, hippocampal formation; TH, thalamus.
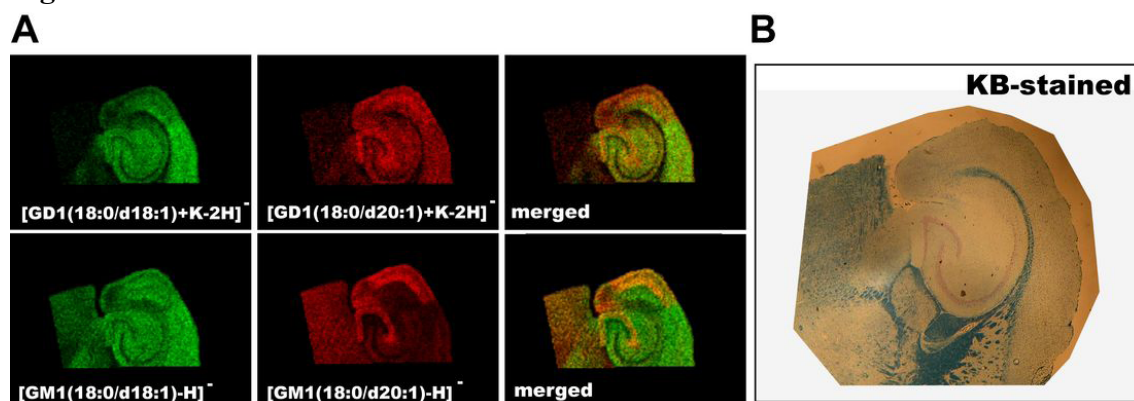
Figure S5.

Figure S5. Distribution patterns of ST molecular species in mouse brain sections. In negative ion detection mode, IMS of a brain section simultaneously revealed the distribution patterns of ST molecular species. In contrast to the GPLs, all of the molecular species visualized were localized in the myelinated region, but the molecular species with long carbon chains were more strongly contained in the mid-brain region than those with short carbon chains. Molecular assignment was performed according to the reference (Jackson et al., 2007).
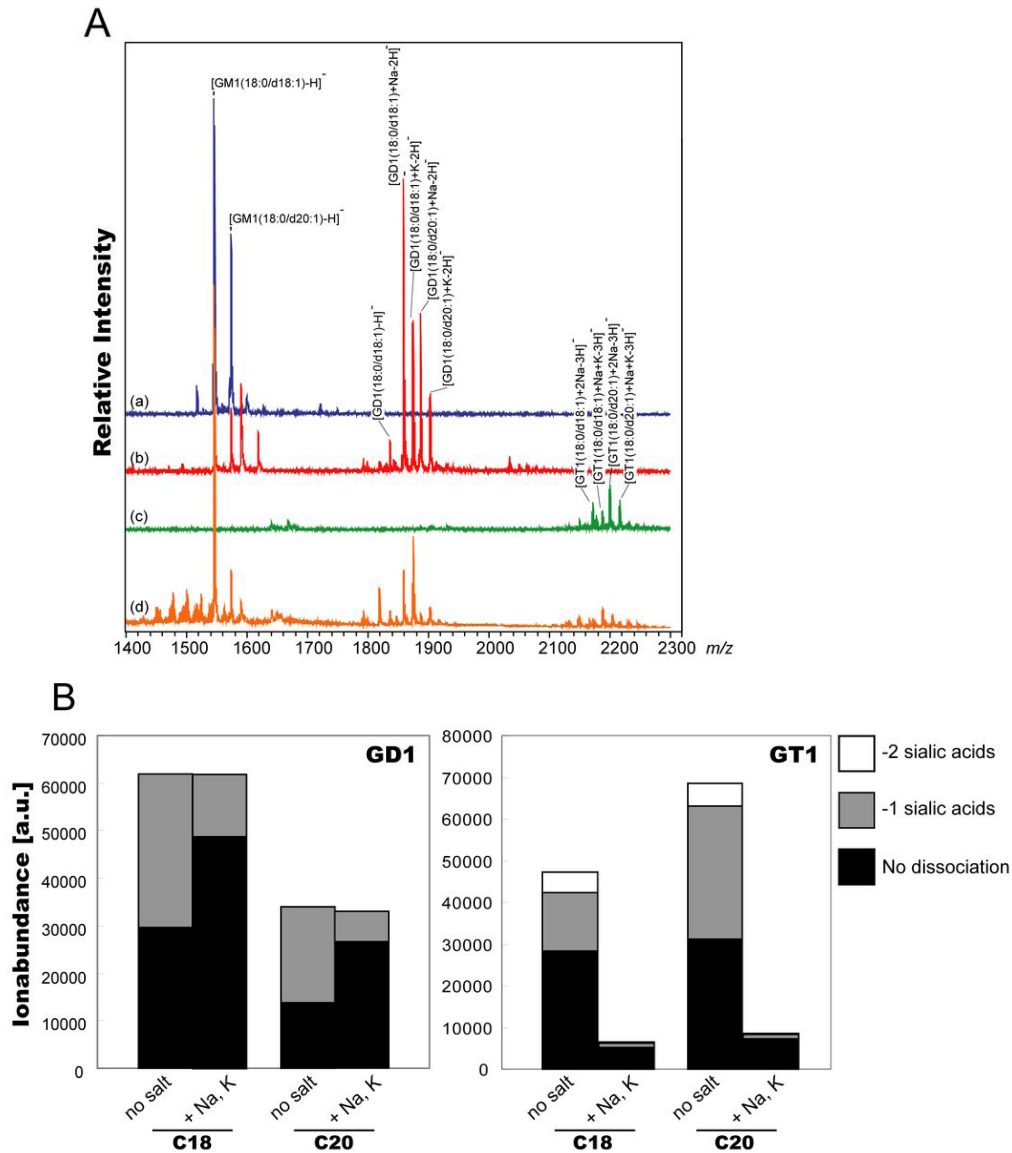
Figure S6.

A

B

Figure S6. Structures of ganglioside molecular species containing C18-LCB and C20-LCB. C20 species has 2 more carbons in their LCB moiety than C18 species (arrow).
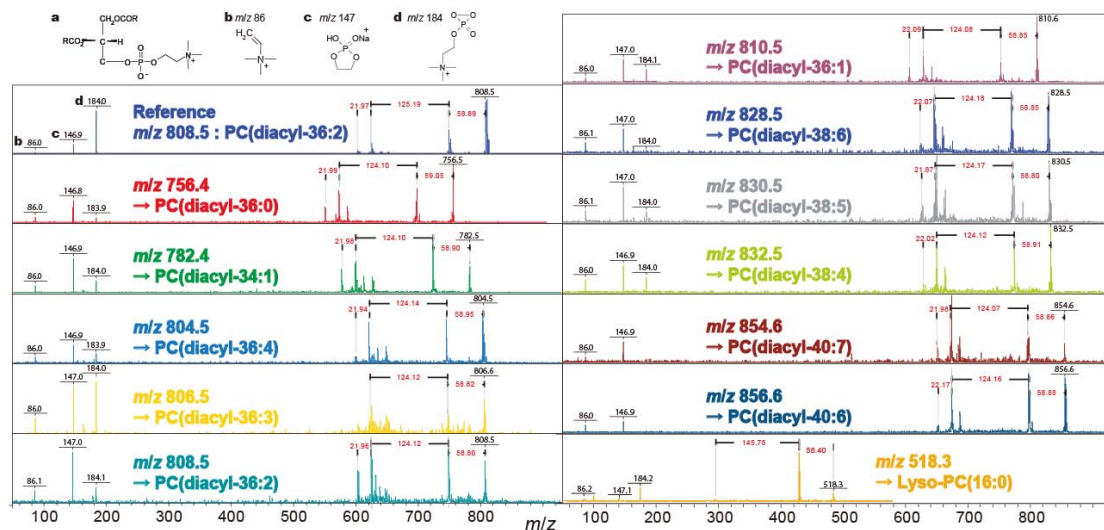
Figure S7.

Figure S7. C20 gangliosides were concentrated in the dendritic region of hippocampal granule neurons. A. Low-resolution MSI (40 µm raster) was performed to gain an overview of ganglioside expression in the horizontal section of mouse brain. For ions corresponding to the GD1 molecular species, I visualized the ion distribution of the potassium complex, i.e., the ions at *m/z* 1874 and *m/z* 1902, which correspond to the [M+K-H]⁻ form of C18- and C20-GD1, respectively. For those corresponding to GM1, the ions at *m/z* 1544 and *m/z* 1572, which correspond to C18-spingosine- and C20-sphingosine-containing GM1 species, respectively, are shown. B. To show the projections from the EC to the DG, an optical image of successive sections stained by the KB method has been presented.

134

Figure S8.

Figure S8. Direct MS/MS on the tissue surface identified the mass peaks of 10 abundant PCs of the hippocampus.
Product ion spectra of the mass peaks corresponding to the 10 abundant PCs of the hippocampus were obtained using MS/MS. Neutral loss of $m/z = 59$, 124, and 146, which correspond to trimethylamine, cyclophosphonate, and sodiated cyclophosphonate, were observed in the product ion spectrum of the reference PC and used to identify PC-derived mass peaks. In addition, diagnostic fragment ions, $m/z = 86$, 147 (cationized cyclophosphonate by sodium ion) and 184 (phosphatidylcholine ion), were also used; their structures are also presented.